ELECTRONIC AND STERIC EFFECT IN TRANSITION METAL CATALYZED GROUP TRANSFER REACTIONS: PAVING THE ROAD TO HIGH THROUGHPUT VIRTUAL SCREENING OF CATALYSTS

by

Tzuhsiung (Nick) Yang

A dissertation submitted in partial fulfillment of the

requirements for the degree of

Doctor of Philosophy

(Chemistry)

at the

UNIVERSITY OF WISCONSIN – MADISON

2018

Date of final oral examination: 05/10/2018

This dissertation is approved by the following members of the Final Oral Committee:

John F. Berry, Professor, Inorganic Chemistry, University of Wisconsin—Madison
Thomas Brunold, Professor, Inorganic Chemistry, University of Wisconsin—Madison
Clark R. Landis, Professor, Inorganic Chemistry, University of Wisconsin—Madison
Jennifer M. Schomaker, Associate Professor, Organic Chemistry, University of Wisconsin—Madison
Miron Livny, Professor, Computer Science, University of Wisconsin—Madison
David P. Goldberg, Professor, Inorganic Chemistry, Johns Hopkins University

Electronic and Steric Effect in Transition Metal Catalyzed Group Transfer Reactions: Paving the Road to High Throughput Virtual Screening of Catalysts

Tzuhsiung (Nick) Yang

Under the supervision of Professor John F. Berry University of Wisconsin – Madison

Abstract

Computational chemistry has become a widely employed complementary tool to the understanding of spectroscopy and reactions. With the continuous developments of computer software and hardware, the role of computers in chemistry has become highly interweaved to experiments and will one day lead discoveries. Chapters 2 and 3 illustrate the application of computational chemistry in the understanding of experiments. In Chapter 2, computational studies are applied to understand experimental spectroscopic signals, geometric and electronic structure of the reactive intermediates, and the reaction mechanism in the proposed Rh_2(II,III) catalytic mechanism in Rh_2-catalyzed nitrene transfer. In Chapter 3, computational chemistry is applied to understand the experimentally observed ligand-tunable silver-catalyzed chemoselective intermolecular nitrene transfer. In contrast, Chapters 4 and 5 demonstrate the role of computers in chemistry. In Chapter 4, grid computing is exploited to accelerate/enable the evaluation of nuclear second derivatives, from which vibrational frequencies, partition function, enthalpy, and entropy can be calculated. In Chapter 5, building on the established crystal database, the Cambridge Structural Database, drug docking program Autodock, the HTCondor framework, and the Open

Science Grid, high throughput virtual screening of novel and potentially efficient catalysts is presented.

The first half of this thesis describes the established involvement of computational chemistry in experimental studies and the second half provides primers for the expansion of computers in chemistry. Future developments such as other grid-computing-based reimplementation of theoretical methods, with one such example described in Chapter 5 and database establishment based on the data generated in Chapter 6 are foreseeable.

DEDICATION

This work is dedicated to my parents, Ming-hui Kuo and Chin-chi Yang, who have provided me a fostering environment and supported my decisions in life. This work is also dedicated to my best friend and husband Li-Ming Hsu for his support throughout five years of graduate school. Last but not the least, this work is also dedicated to all adventurous spirits who dream various possibilities of the future of science.

ACKNOWLEDGMENTS

I would like to thank my advisor, Professor John F. Berry, first for accepting my request to transfer from the Johns Hopkins University to the University of Wisconsin—Madison to join his group in Spring 2015. Throughout my time under his supervision, John provided me with a great amount of freedom in terms of research direction, working style, and travel. And it is indeed this kind of freedom he gave me energized my imagination and independence to come up with different research directions and ideas. In addition, John created a fostering research environment for me given how different my research is from the rest of the group: he introduced me to the Center for selective C-H functionalization (CCHF), through which I was exposed to different fields of chemistry; Prof. Jennifer M. Schomaker (for whom I have a separate paragraph to acknowledge below), who developed me in terms of research and independence through collaboration; Prof. Frank Weinholds, who I am truly grateful for his generous donation of a gratis copy of NBO 6.0.

I would like to thank Professor Jennifer M. Schomaker for both being my collaborator and a reader of my thesis. Believe or not, I never thought in my graduate career that I would ever work so closely with organic chemistry. I was really bad at organic lab back in college and organic chemistry never interested me much after organic lecture I and II. I guess one can never tell in life. That being said, one of my biggest fortune in graduate school is to collaborate with the Schomaker group. I really learned scientifically so much through this collaboration: various types of selectivities, different styles of writing a manuscript, and more. If I did not have this experience, I would not have approached the Center for High Throughput Computing, started thinking about automating elementary step calculation, reimplementing numerical differentiation into grid

computing, and devising methods to allow high throughput virtual screening of catalysts. In addition, I made so many friends/connections through this collaboration, Minxue Huang, Minsoo Ju, Ryan Scamp, and Jessica Roberts. If it was not for this great opportunity, I could not imagine other possibilities that our paths would have intercepted. And lastly, I would like to thank her for putting up with how slow I am on putting results together.

I would like to thank Professor David P. Goldberg for being my advisor at the Johns Hopkins University and a reader of my thesis. I am really grateful to him for all the mentoring and opportunities to learn. I came in to his lab with some experience in computational chemistry and he gave me a great opportunity to start my career with a project to calculate Mossbauer parameters of an $Fe^{IV}(O)$ complex. Following this project, David provided me opportunities to work on various spectroscopy-related projects: calculating vibrational spectra, Mn K-edge XAS pre-edge absorption, EPR parameters, and oxo transfer reactivity. Throughout these projects, he gave me the opportunities to work with experts from diverse fields: Prof. Serena DeBeer and Prof. Sam P. de Visser. These opportunities really improved my knowledge in XAS, EPR, and reaction modeling. And last but not the least, I thank David for supporting my decision to transfer.

I would like to thank my committee members Professor Thomas Brunold and Prof. Clark R. Landis. Thank you for walking me through various stages in my graduate education and, to me most importantly, professional development. To me, Thomas was always cheerful when I ran into him. I cannot thank him enough for sharing with me his experience as a foreigner in this country and his advice in terms of post-graduate career choices. One thing I admire Thomas very much is his expertise in spectroscopy. Personally, I have this infatuation for spectroscopies. If I had a chance to start over in graduate school, I would like to be a cool spectroscopist just like Thomas. I would like to thank Clark for his guidance in my personal development. I came into graduate

school with the naïve thought that all I had to manage was research and research (and research). Undoubtedly, I was ignorant. It will always be a lesson I have to undergo that human are not numbers and logics. And I thank you Clark for walking me through this.

I would like to thank Professor Miron Livny for being a reader of my thesis and the invention of HTCondor. Even though I have not personally worked with Professor Livny, I have benefited enormously from the HTCondor project of his and his coworkers'. I learned so much during the office hours of the CHTC and the OSG summer school (2016). And I am truly grateful to Professor Livny for all these resources, which really broaden my imagination. Chapters 4 and 5 are particularly attributed to Professor Livny and his team: If I did not have the opportunity to know about the HTCondor, these two chapters would have not been possible at all.

I would like to thank the staff at chemistry department, in particular Kristi Heming, Karen Stephens, Arrietta Clauss, Heike Hofstertter, and Charles Fry for your administrative and technical support. I would also like to thank the staff at the CHTC Lauren Michael and Christina Koch for your support on the cluster. I learned how much about the CHTC, HTCondor, and OSG through you and this enabled substantial portion of my projects.

I would like to thank Dr. Jeeyong Jeong (currently an assistant professor at Amherst college) for her mentorship during college. She taught me how to perform biological experiments with human cell, cancer cell, yeast, and *E*. coli. Even to now, I still remember one phrase she said to me as I paraphrase, "you have to do the experiment regardless when if the cells are ready."

I would like to thank Dr. Amanda R. Corcos for being my research mentor in chemistry during college and coworker during graduate school. I thank her for teaching me how to perform wet chemistry: Schlenk line technique, inorganic synthesis, frozen photolysis, and more. She really started me in chemistry and taught me how to think critically.

I would like to thank my friends at the Johns Hopkins University and the University of Wisconsin—Madison: Henry Chung, Gaoxiang Liu, Zhewen Song, Yunxiang (Sean) Dai, Kelvin Xie, Mandy Tsai, and Chandra Yang for their support throughout graduate school.

TABLE OF CONTENTS

LIST OF TABLES

LIST OF FIGURES

LIST OF CHARTS

LIST OF SCHEMES

1 Wisconsin Initiative for Science Literacy: Introduction for a General Audience

1.1 Theoretical Chemistry

When people think of chemistry, what usually comes into mind is mixing solutions together, generation of gas (explosion as an extreme), etc. In rare occasions, people think about the involvement of mathematics in chemistry; another way to phrase it is one usually does not need to solve equations in chemistry. To understand the role of theoretical chemistry, consider the preparatory steps before a bridge is being built: sketching the bridge, estimating the capacity, and, most importantly, modeling the strength of the bridge to ensure it is not going to break by the laws of classical mechanics (or Newtonian mechanics). If we can mathematically have some sense regarding the success of constructions as big as a bridge, why can we not attempt the same for those as small as molecules? After all, chemistry is a field of science that concerns the interactions among electrons and protons (with the exception that nuclear chemistry and the associated nuclear medicinal chemistry are also concerned with the neutrons). For example, chlorine ions exchange electrons with hydroxide ions if you mix bleach with acidic tile cleaner (Caution, this is a toxic reaction). Therefore, in theory, we should be able to describe chemical reactions like how we calculate the interactions among point charges in middle/high school physics class. It turns out that things become bizarre when the size of them approaches atomic level. Just to name two famous bizarre phenomena: Schrödinger's cat (uncertainty principle) and Einstein's spooky action of electrons (quantum entanglement). Hence, complicated mathematical functions are needed to describe the actions of electrons in molecules. One question that follows is why we care about theoretical chemistry if the equations are hard to solve and if all we get is numbers on a piece of paper. The answer to that question is that there are situations in chemistry that physical instinct

based on Newtonian mechanics cannot rationalize experimental observations, such as the color and the magnetic properties of chemicals. And indeed, theoretical chemistry is commonly employed to understand signals observed in experiments such as spectroscopy. Furthermore, imagine the possibility to predict the success of reactions before even setting them up. Indeed, this is one of the ultimate goals of theoretical chemistry.

1.2 Density Functional Theory

In the previous section, it was noted that complicated functions are needed to describe the electrons in a molecule because electrons have non-particle-like properties (wave particle duality). Even the functions have units of the square root of density (i.e., $\sqrt{1/ft^3}$), which has barely any real world meaning. A famous physicist Max Born proposed what was later called the Born interpretation that the square of these complicated functions (the wave functions) provides the probability density to locate electrons at a given position. Hence, we know how to "find" where the electrons are in a molecule with some certainty. If we know where the electrons are, how fast they are traveling, and how hard they repel each other (recall the point charge analogy in the previous section), we know the energy of the electrons in a molecule, hence the energy of the molecule and the energy of molecules turning into other molecules (hence the energy of chemical reactions!). This is called the Density Functional Theory because the energy of a molecule is a function of the electron density, which itself is a function of the position of electrons (and nuclei). Indeed, this idea that the electron density determines the properties (such as energy in the form of heat) and the better we know the electron density in a molecule the more accurate the estimate of the energy of the molecule was proposed by Walter Kohn and Pierre Hohenberg. However, this is still a very complicated question because there are many electrons in a molecule, i.e. H_2O has 12 electrons, which repel each other simultaneously. Hence, we need to make some approximations, which if perfect will lead to the extra density. This idea was suggested by Walter Kohn and Lu Jeu Sham in 1965 and known as the Kohn-Sham equation by considering each electron in a molecule behaving as though that they do not see each other yet maintain the density for electrons that see each other. This idea is under active investigation and has a great promise for economical yet accurate computation of chemistry.

1.3 Computers in Chemistry

Computers have been indispensable in daily life since their invention during World War II. One of the changes that computers have brought to our lives is the ability to handle enormous amount of enumeration quickly. For example, search engines such as Google can search through thousands of threads in seconds. However, the involvement of computers in chemistry is much less mundane. The reason for this, at least to some extent, is because chemistry has been around for centuries, which can go all the way back to the Bronze Age. However, the involvement of computers in chemistry had not surfaced until the invention of modern computers and theoretical development of economical yet accurate methods such as the Density Functional Theory. Nowadays, computers are used in chemistry within a continuum having two extremes: methods based on theoretical constructs and those based on experimental data mining. For example, computers can be utilized to enumerate the equations that describe the interaction of molecules with light (spectroscopy), providing a theoretical support for the experimental observations; computers can simulate reaction processes that are too fast to be captured and studies experimentally. In addition, computers can perform fast and systematic sorting, analyzing, and parameterizing of an experimental database. This data-driven approach allows examining chemistry from a more holistic angle and building upon existing observations to extrapolate to future discoveries through methods as simple as linear (or multiple) regression to sophisticated methods such as machine learning. As computer software and hardware continue advancing, computers in chemistry will only become more involved and indispensable.

2 Rh2(II,III) Catalysts with Chelating Carboxylate and Carboxamidate Supports: Electronic Structure and Nitrene Transfer Reactivity

This chapter has been published:

Varela-Álvarez, A.;[†,⊥] Yang, T.;[‡,⊥] Jennings, H.;[‡] Kornecki, K. P.[‡] Macmillan, S. N.;[§] Lancaster, K. M.;[§] Mack, J. B. C.;[∥] Du Bois, J.;[∥] Berry, J. F.[*,‡] and Musaev, D. G.[*,†] *J. Am. Chem. Soc.* **2016**, 138, 2327−2341

[†]The Cherry L. Emerson Center for Scientific Computation, Emory University, Atlanta, Georgia 30322, USA

[‡]Department of Chemistry, University of Wisconsin—Madison, Madison, Wisconsin 53706, USA

[§]Department of Chemistry and Chemical Biology, Cornell University, Ithaca, New York 14853, USA

[∥]Department of Chemistry, Stanford University, Stanford, California 94305, USA

[⊥]A.V.-A. and T.Y. contributed equally to this work.

2.1 My Contribution to this Work

This paper describes a combination of experimental and computational studies to understand the role of the one-electron oxidized catalyst Rh_2(II,III) in Rh_2(II,II)-catalyzed intramolecular nitrene transfer. The scope of the paper is vast; ranging from experimental electrochemical, EPR, XAS, and H/D KIE studies to computational EPR, CASSCF, redox potential, reaction coordinate, and H/D KIE calculations. One particular challenging aspect of the Rh_2(II,III) complexes is their highly modulable electronic state, evidenced by experimental EPR signals. This translates to multiple low lying electronic states in computational studies. My contribution to this highly collaborative work indeed focuses on this aspect of the Rh_2(II,III) complexes.

When multiple low lying electronic states are present and allowed to mix according to the spin (spin multiplicity) selection rule, these states all contribute to the ground electronic wavefunction of a molecule. Theoretical methods that are based on a single electronic configuration (a single determinant) are by construct not adequate. Therefore, multiconfigurational, such as CASSCF, methods are required to accurately represent the system. Some physical aspects of CASSCF methods are the inclusion of orbital momentum when two electronic configurations are related by an orbital angular momentum operator, which is crucial to describe electron-magnetic field interactions such as in an EPR experiment; and resonance structures that generate different orbital occupations, such as metal(n)-nitrene and metal(n+1)-nitrene anion radical resonance structures (n denotes the oxidation state).

Equipped with these physically sounding properties, CASSCF method is less widely used in the field of computational chemistry due to its non-black-box computational procedure. Orbitals in the active space are collected by users, where the selection procedure and assignments rely on the chemical intuition and experience of the user. Yet, orbital optimization step upon the assigned active space is variational, resulting in the possibility of unexpected final active space. When chemical unsounding results are found, users have to recollect orbitals for further orbital optimization. Upon the convergence of chemically intuitive active space, EPR g factors or resonance configurations can be examined.

2.2 Abstract

Dirhodium-catalyzed C−H amination is hypothesized to proceed via Rh_2-nitrene intermediates in either the Rh_2(II,II) or Rh_2(II,III) redox state. Herein, we report joint theoretical and experimental studies of the ground electronic state (GES), redox potentials, and C−H

amination of $[Rh_2^{II,III}(O_2CCH_3)_4(L)_n]^+$ (**1_L**) (L = none, Cl^-, and H_2O), $[Rh_2(esp)_2]^+$ (**2**), and $Rh_2(espn)_2Cl$ (**3**) (esp = α,α,α′,α′-tetramethyl-1,3-benzenedipropanoate and espn = α,α,α′,α′-tetramethyl-1,3-benzenedipropanamidate). CASSCF calculations on **1_L** yield a wave function with two closely weighted configurations, $(\delta^*)^2(\pi_1^*)^2(\pi_2^*)^1$ and $(\delta^*)^2(\pi_1^*)^1(\pi_2^*)^2$, consistent with reported EPR g values [Chem. Phys. Lett. 1986, 130, 20−23]. In contrast, EPR spectra of **2** show g values consistent with the DFT-computed $(\pi^*)^4(\delta^*)^1$ GES. EPR spectra and Cl K-edge XAS for **3** are consistent with a $(\pi^*)^4(\delta^*)^1$ GES, as supported by DFT. Nitrene intermediates **2N_L** and **3N_L** are also examined by DFT (the nitrene is an NSO_3R species). DFT calculations suggest a doublet GES for **2N_L** and a quartet GES for **3N_L**. CASSCF calculations describe the GES of **2N** as Rh_2(II,II) with a coordinated nitrene radical cation, $(\pi^*)^4(\delta^*)^2(\pi_{nitrene,1})^1(\pi_{nitrene,2})^0$. Conversely, the GES of **3N** is Rh_2(II,III) with a coordinated triplet nitrene, $(\pi^*)^4(\delta^*)^1(\pi_{nitrene,1})^1(\pi_{nitrene,2})^1$. Quartet transition states (^{4}TSs) are found to react via a stepwise radical mechanism, whereas ^{2}TSs are found to react via a concerted mechanism that is lower in energy compared to ^{4}TSs for both **2N_L** and **3N_L**. The experimental (determined by intramolecular competition) and ^{2}TS-calculated kinetic isotopic effect (KIE) shows a KIE ∼ 3 for both **2N** and **3N**, which is consistent with a concerted mechanism.

2.3 Introduction

C−H amination via nitrene transfer catalysis (NTC) has the potential to be a transformative method in synthetic organic chemistry.[1-5] Some of the leading catalysts for intra- and intermolecular C−H amination via NTC are coordination complexes with a Rh(II)−Rh(II) bond (Scheme 2.1such as the Rh_2-tetracarboxylates and the $Rh_2(esp)_2$ (esp = α,α,α′,α′-tetramethyl-1,3-benzenedipropanoate) catalyst bearing chelating dicarboxylate ligands, which operate best with

sulfamatederived nitrene species (NSO_3R).[6] Other catalysts such as silver, [7-11] iron,[12-18] manganese, [16, 19-20] ruthenium, [20-23] copper,[24-30] and cobalt[31-34] complexes have been shown to perform C−H amination, as well. The Rh_2(II,II) complexes were initially presumed to perform C−H amination via a nitrene interception/insertion mechanism, as shown in Scheme 2.1,[6, 35] in analogy to related carbene transfer reactions.[36] However, subsequently, Du Bois and Berry have independently shown the formation of mixed-valent Rh_2(II,III) species (including a Rh_2(II,III)-nitrene species proposed by Du Bois and Zare) under the highly oxidative NTC conditions, which are also believed to be active in NTC reactivity.[37-39]

Scheme 2.1. NTC Cycle for $Rh_2(esp)_2$ and $Rh_2(espn)_2Cl$

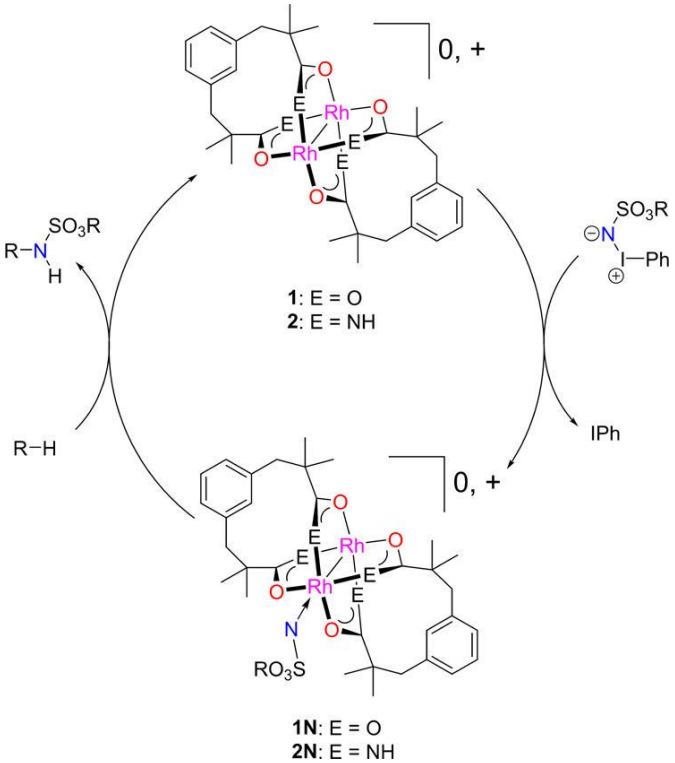

Recently, the Berry group reported a new amidate-ligated Rh_2(II,III) catalyst, $Rh_2(espn)_2Cl$ (espn = α,α,α′,α′-tetramethyl-1,3-benzenedipropanamidate), which is capable of performing intramolecular C−H amination and has a long lifetime under NTC conditions, achieving turnover numbers higher than those of $Rh_2(esp)_2$ by a factor of 3 in head-to-head intramolecular competition

experiments.[40] The longer lifetime of $Rh_2(espn)_2Cl$ during NTC compared to that of $Rh_2(esp)_2$ may be attributed to the greater thermodynamic stability of the former complex. As has been well-documented, amidate ligands not only bind more strongly to the Rh_2 core than do carboxylate ligands but also lower the potential required for oxidation of Rh_2(II,II) to the Rh_2(II,III) level.[41]

Compared to Rh_2(II,II) compounds, there are far fewer investigations of Rh_2(II,III) species. The most extensive electronic structure study of Rh_2(II,III) species, done by Norman and co-workers in 1979,[42] was very thorough but utilized methods that are now out of date and known to lead to inaccurate conclusions. The electronic structure of Rh_2(II,III) species is complex because of the existence of multiple low-lying electronic configurations, which could contribute to their total ground state wave function. Rh_2(II,II) complexes have a single Rh−Rh bond by virtue of the $(\sigma)^2(\pi)^4(\delta)^2(\delta^*)^2(\pi^*)^4$ electron configuration, where all Rh−Rh bonding and antibonding orbitals are filled with the exception of the σ* antibonding orbital.[43] The π* and δ* orbitals located below the σ* orbital are very close in energy,[44] and thus, upon oxidation of Rh_2(II,II) to Rh_2(II,III), it is a priori unclear whether a π* or δ* electron would be removed, leading, in rigorous D_4h symmetry, to a ^2E_g or $^2B_{1u}$ ground electronic state (GES), respectively (Chart 2.1).

Chart 2.1. Possible Ground States of Rh_2(II,III) Compounds

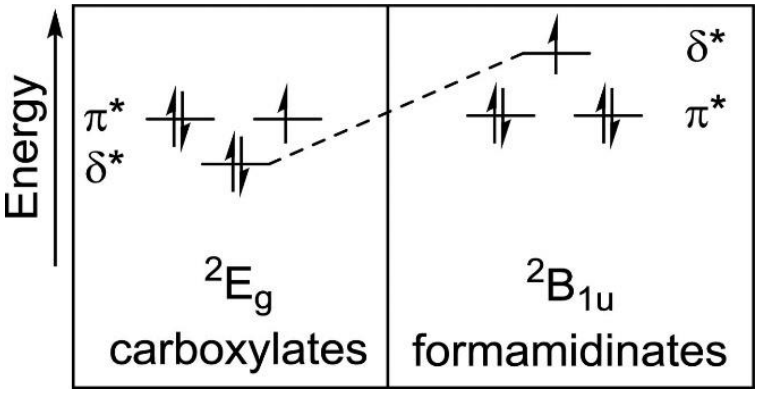

In principle, the ^2E_g and $^2B_{1u}$ states may be distinguished by EPR spectroscopy since the first-order spin−orbit coupling of the former state leads to the appearance of unusual EPR signals,

with g values widely different from the free electron value.[45] In this way, Kawamura and co-workers have shown that a range of Rh_2(II,III) carboxylate (O,O donor) complexes have the ^2E_g ground state, whereas Rh_2(II,III) compounds with N,N donor ligands (e.g., formamidinates) have the $^2B_{1u}$ ground state.[46-49] An interesting question arises in considering Rh_2(II,III) complexes with amidate (N,O donor) ligands: will these compounds have a ^2E_g ground state like the corresponding carboxylate compounds, or is the π-donation of the equatorial ligand field now strong enough that the δ* orbital is raised above the π*, leading to a $^2B_{1u}$ ground state like in the corresponding formamidinate compounds? An acetamidate-supported Rh_2(II,III) complex has been characterized by EPR spectroscopy in acetonitrile and DMSO solution and was found to have g values, $g_\perp \sim 2.1$ and $g_\parallel \sim 1.9$, consistent with a single Kramer's doublet and therefore indicative of a $^2B_{1u}$-type $(\delta^*)^1$ ground state.[50]

Here we address the Rh_2(II,III) GES of $[Rh_2(OAc)_4(L)_n]^{m+}$, **1_(L)$_n$**, $[Rh_2(esp)_2(L)_n]^{m+}$, **2_(L)$_n$**, and $[Rh_2(espn)_2(L)_n]^{m+}$, **3_(L)$_n$** [where L = none with m = 1; L = H_2O, n = 1 or 2 with m = 1; L = Cl^-, n = 1 with m = 0; and L = Cl^-, n = 2, with m = −1] species by EPR spectroscopy and, where applicable, Cl Kedge XAS, as well as by computational approaches including density functional theory (DFT) and ab initio state-averaged complete active space self-consistent field methods (SA-CASSCF), where necessary. Dynamic electronic correlation effects were included by utilizing multireference difference-dedicated configuration interaction theory with two degrees of freedom (MR-DDCI2). We also elucidate the impact of the nature of the GES of these Rh_2(II,III) complexes to the stability and reactivity of their proposed nitrene intermediates by investigating intramolecular C−H amination catalyzed by **2_L** and **3_L** species. Although it is instructive to compare the GES of **2_L** and **3_L** with that of the simplified **1_L** species, the latter species are not included in the reactivity studies because NTC by **1_L** has not been established to utilize the

Rh_2(II,III) oxidation state.

2.4 Results and Discussion

2.4.1 Analysis of the Rh_2(II,III) Compounds.

2.4.1.1 Electronic Structure of Rh_2(II,III) Complexes.

At first, we elucidated the GES of the Rh_2(II,III) complexes using the BP86 density functional method in conjunction with TZVP basis sets[51] for optimization of geometries. Reported DFT energies were derived from single-point B3LYP calculations on the BP86-optimized structures.[52-55] Redox potential calculations were performed using an established methodology.[56] MR-DDCI2:-SA-CASSCF calculations were performed using various active spaces (see the Computational Methods section for more details).

We start our discussion with Rh_2(II,III) tetra-acetate complexes $[Rh_2(OAc)_4]^+$, **1**, $[Rh_2(OAc)_4(H_2O)_2]^+$, **1_(H$_2$O)$_2$**, $[Rh_2(OAc)_4Cl]$, **1_Cl**, and $[Rh_2(OAc)_4(Cl)_2]^-$, **1_Cl$_2$**. Herein, we mostly focus on **1_(H$_2$O)$_2$** and **1_Cl$_2$** for which experimental data are available, but we also compare those to 1 to gauge the effect of axial ligand coordination to the Rh_2(II,III) core. EPR spectra of $[Rh_2(OAc)_4(L)_n]^{m+}$ have been reported with L = H_2O, EtOH, and THF with n = 2 and m = 1, and Cl with n = 2 and m = −1. The spectra are axial with $g_{\parallel}$ = 3.38−4.00 and $g_{\perp}$ = 0.6−1.5.48 These unusual g values are described by Kawamura and co-workers as the result of a first-order spin−orbit interaction derived from the nearly degenerate π^* orbitals of the ^2E_g state, but computational support for these phenomenological assignments is lacking.[46-49]

To validate DFT methods against these experimental data, the GES and EPR parameters for the compounds **1**, **1_(H$_2$O)$_2$**, **1_Cl**, and **1_(Cl)$_2$** were calculated. These DFT calculations converged to the expected ^2E_g GES for all four complexes. However, despite predicting the

anticipated ^2E_g ground state, the DFT-calculated EPR g values are incompatible with the available experimental data: DFT predicts a markedly rhombic g tensor with abnormal values, giving g_1, g_2, and g_3 of 7.36, 2.61, and 2.04 for 1, 3.41, 2.32, and 2.07 for **1_(H2O)2**, 27.4, 2.43, and 2.13 for **1_Cl**, and 18.5, 2.77, and 2.14 for **1_Cl2**, respectively, whereas the experimental spectra are axial with $g_{\parallel} \sim 4.00$ and $g_{\perp} \ll 2.00$ (see Table 2.1).

Table 2.1. Calculated and Experimentally Measured EPR Parameters of the $[Rh_2(OAc)_4(L)_n]^{m+}$, **1_L**, Species (L = None, H_2O, and Cl^-)

species	g_1	g_2	g_3	methods
$[Rh_2(OAc)_4]^+$	7.36	2.61	2.04	RI-B3LYP
	4.00	0.05	0.05	MR-DDCI2:SA-CASSCF(13e/8o)
$[Rh_2(OAc)_4(H_2O)_2]^+$	3.61	1.50	1.50	experiment[48]
	3.41	2.32	2.07	RI-B3LYP
	3.83	0.87	0.87	MR-DDCI2:SA-CASSCF(17e/10o)
$Rh_2(OAc)_4Cl$	27.4	2.43	2.13	RI-B3LYP
	3.99	0.18	0.18	MR-DDCI2:SA-CASSCF(19e/11o)
$[Rh_2(OAc)_4(Cl)_2]^{-a}$	4.00	0.60	0.60	experiment[48]
	18.5	2.77	2.14	RI-B3LYP
	4.01	0.01	0.01	MR-DDCI2:SA-CASSCF(25e/14o)
$[Rh_2(esp)_2]^-$	2.14	2.14	1.93	experiment (this work)
	2.25	2.25	1.89	experiment (this work)
	2.24	2.11	2.06	RI-B3LYP

[a]No crystal structure of $[Rh_2(OAc)_4(Cl)_2]^-$ was available, so the geometry was obtained from the structure of $[Rh_2(OAc)_4Cl_2]^{2-}$.[105]

The aforementioned discrepancy between the experimental and DFT findings can be explained by the multideterminant nature of the ^2E_g electronic state, where the energetic degeneracy of the π^* orbitals presents an inherent problem for all single-determinant-based methods, including DFT.[57] Indeed, a "proper" wave function of the ^2E_g electronic state should include, at least, the following two simplified determinants

$$\Psi(^2E_g) = \frac{1}{\sqrt{2}}[|(\pi_1^*)^2(\pi_2^*)^1| + |(\pi_1^*)^1(\pi_2^*)^2|] \quad (1)$$

because the unpaired electron has an equal probability of being housed in either the π_1^* or the π_2^* orbital. In order to properly describe such a multideterminant system allowing for an accurate prediction of g tensors of the complexes, the CASSCF approach is utilized.

Table 2.2. Leading Configurations in the SA-CASSCF Wave Functions of $[Rh_2(OAc)_4(L)_n]^{m+}$, **1_L**, Species (L = None, H_2O, and Cl^-)[a]

compound	active space	CSFs[b]	weight (%)
$[Rh_2(OAc)_4]^+$	(13,8)	$\delta^2\delta^{*2}\pi_1^2\pi_2^2\sigma^2\pi^{*}_1{}^2\pi^{*}_2{}^1\sigma^{*0}$	43.3
		$\delta^2\delta^{*2}\pi_1^2\pi_2^2\sigma^2\pi^{*}_1{}^1\pi^{*}_2{}^2\sigma^{*0}$	43.3
$[Rh_2(OAc)_4(H_2O)_2]^+$	(17,10)	$\pi^{*}_{2,+}{}^2\sigma^{*}_{+}{}^2\delta^2\delta^{*2}\pi_1^2\pi_2^2\sigma^2\pi^{*}_1{}^2\pi^{*}_{2,-}{}^1\sigma^{*}_{-}{}^0$	43.5
		$\pi^{*}_{2,+}{}^2\sigma^{*}_{+}{}^2\delta^2\delta^{*2}\pi_1^2\pi_2^2\sigma^2\pi^{*}_1{}^1\pi^{*}_{2,-}{}^2\sigma^{*}_{-}{}^0$	43.5
		$\pi^{*}_{2,+}{}^2\sigma^{*}_{+}{}^2\delta^2\delta^{*2}\pi_1^u\pi_2^2\sigma^d\pi^{*}_1{}^2\pi^{*}_{2,-}{}^2\sigma^{*}_{-}{}^u$	4.6
		$\pi^{*}_{2,+}{}^2\sigma^{*}_{+}{}^2\delta^2\delta^{*2}\pi_1^2\pi_2^u\sigma^d\pi^{*}_1{}^2\pi^{*}_{2,-}{}^2\sigma^{*}_{-}{}^u$	4.6
$Rh_2(OAc)_4Cl$	(19,11)	$\delta^2\delta^{*2}\pi_1^2\pi_2^2\pi_{1,nb}{}^2\pi_{2,nb}{}^2\sigma^2\sigma_{nb}{}^2\pi^{*}_1{}^2\pi^{*}_2{}^1\sigma^{*0}$	41.9
		$\delta^2\delta^{*2}\pi_1^2\pi_2^2\pi_{1,nb}{}^2\pi_{2,nb}{}^2\sigma^2\sigma_{nb}{}^2\pi^{*}_1{}^1\pi^{*}_2{}^2\sigma^{*0}$	41.9
		$\delta^2\delta^{*2}\pi_1^2\pi_2^2\pi_{1,nb}{}^2\pi_{2,nb}{}^2\sigma^2\sigma_{nb}{}^0\pi^{*}_1{}^2\pi^{*}_2{}^1\sigma^{*2}$	4.2
		$\delta^2\delta^{*2}\pi_1^2\pi_2^2\pi_{1,nb}{}^2\pi_{2,nb}{}^2\sigma^2\sigma_{nb}{}^0\pi^{*}_1{}^1\pi^{*}_2{}^2\sigma^{*2}$	4.2
$[Rh_2(OAc)_4Cl_2]^{-}$[c]	(25,14)	$\pi_{1,+}{}^2\pi_{2,+}{}^2\pi^{*}_{1,+}{}^2\pi^{*}_{2,+}{}^2\sigma_{+}{}^2\delta^2\delta^{*2}\sigma^{*}_{+}{}^2\pi_{1,-}{}^2\pi_{2,-}{}^2\sigma_{-}{}^2\pi^{*}_{1,-}{}^2\pi^{*}_{2,-}{}^1\sigma^{*}_{-}{}^0$	43.2
		$\pi_{1,+}{}^2\pi_{2,+}{}^2\pi^{*}_{1,+}{}^2\pi^{*}_{2,+}{}^2\sigma_{+}{}^2\delta^2\delta^{*2}\sigma^{*}_{+}{}^2\pi_{1,-}{}^2\pi_{2,-}{}^2\sigma_{-}{}^2\pi^{*}_{1,-}{}^1\pi^{*}_{2,-}{}^2\sigma^{*}_{-}{}^0$	42.8
		$\pi_{1,+}{}^2\pi_{2,+}{}^2\pi^{*}_{1,+}{}^2\pi^{*}_{2,+}{}^2\sigma_{+}{}^2\delta^2\delta^{*2}\sigma^{*}_{+}{}^2\pi_{1,-}{}^u\pi_{2,-}{}^2\sigma_{-}{}^d\pi^{*}_{1,-}{}^2\pi^{*}_{2,-}{}^1\sigma^{*}_{-}{}^u$	5.0
		$\pi_{1,+}{}^2\pi_{2,+}{}^2\pi^{*}_{1,+}{}^2\pi^{*}_{2,+}{}^2\sigma_{+}{}^2\delta^2\delta^{*2}\sigma^{*}_{+}{}^2\pi_{1,-}{}^0\pi_{2,-}{}^u\sigma_{-}{}^d\pi^{*}_{1,-}{}^2\pi^{*}_{2,-}{}^1\sigma^{*}_{-}{}^u$	5.0

[a]Configurations with weight >3% are reported. [b]CSFs = configuration state functions. All orbital symbols have their normal meaning; nb = nonbonding, + and − refer to in-phase and out-of-phase contributions of the equatorial ligands. [c]Geometry for the single-point calculation was obtained without further optimization from the crystal structure of $[(NH_2)_3C]_2[Rh_2(OAc)_4Cl_2]$.[105]

The leading determinants of the SA-CASSCF wave functions with their weights are given in Table 2.2. For all **1_L** compounds, there are two leading determinants that contribute equally, or nearly equally, to their total wave functions. In all cases, these two leading determinants are those that differ in their π_1* and π_2* occupation, as anticipated from the above discussion. Thus, the CASSCF results are fully consistent with ^2E_g-derived ground states for these compounds.

The MR-DDCI2 method was used on the converged SACASSCF wave function to predict the g values of $[Rh_2(OAc)_4]^+$: an axial signal with $g_{\parallel} = 4.00$ and $g_{\perp} = 0.05$ is predicted. As seen in Table 2.1, where we provide all calculated and experimental g values for $[Rh_2(OAc)_4]^+$, $[Rh_2(OAc)_4(H_2O)_2]^+$, $Rh_2(OAc)_4Cl$, and $[Rh_2(OAc)_4Cl_2]^-$, the MR-DDCI2:SA-CASSCF-calculated EPR g values are in close agreement with the experimental values. These findings additionally support that all of these species have a ^2E_g ground state containing a $(\pi^*)^3$ valence electron configuration.

Thus, due to existence of the orbital degeneracy in **1_L**$^+$, the DFT approach is not the best method to calculate the lowest energy electronic states and related properties of these compounds.

To date, only one set of crystallographic data is available for a metastable Rh_2(II,III) complex bearing esp ligands, $[Rh_2(esp)_2Cl_2]^-$.[37] In this paper, we report optimized geometries of the species $[Rh_2(esp)_2]^+$, **2**, $[Rh_2(esp)_2(H_2O)]^+$, **2_H₂O**, and $Rh_2(esp)_2Cl$, **2_Cl**. In Table 2.3, we compare the optimized parameters of these species with the available crystallographic values. As seen from this table, the DFT approach describes the Rh−Rh and Rh−O_{av} distances well.

Table 2.3. Calculated and Experimentally Available Important Geometry Parameters (Distances in Å and Angles in deg) of the [Rh2(esp)2L]+, **2_L**, Species (L = None, H2O, and Cl−)

species	Rh−Rh	Rh−L	Rh−O_{av}	Rh−Rh−L
	Calculated: This work			
$[Rh_2(esp)_2]^+$	2.362		2.041	
$[Rh_2(esp)_2(H_2O)]^+$	2.378	2.253	2.043	178.9
$Rh_2(esp)_2Cl$	2.394	2.361	2.065	180.0
	Experiment[39]			
$[Rh_2(esp)_2(Cl)_2]^-$	2.360(1)	2.475(1)	2.023(1)	174.4(1)

DFT calculations on **2** surprisingly predict a $^2B_{1u}$-derived GES with a $(\delta^*)^1$ electron configuration. Analysis shows that in this compound, like in the case of the $[Rh_2(OAc)_4]^+$ complexes, the δ* orbital has significant antibonding contributions from the O−C−O π* carboxylate (bridging) orbitals. However, unlike the case of $[Rh_2(OAc)_4]^+$ complexes, the δ* orbital of **2** also has a contribution from the m-phenylene moieties of the esp ligands, an apparent through-space interaction at 4.3 Å. This interaction slightly destabilizes the δ* orbital, and, consequently, makes the $^2B_{1u}$-type $(\delta^*)^1$ electronic state more favorable for $[Rh_2(esp)_2]^+$ compared to the $[Rh_2(OAc)_4]^+$ complexes.

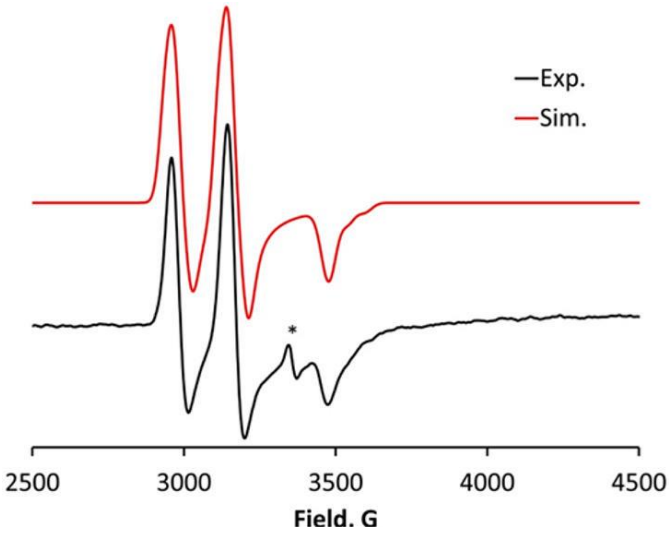

Figure 2.1. X-band EPR spectrum measured at 10 K of an electrochemically oxidized solution of $Rh_2(esp)_2$. The spectrum is modeled with two axially symmetric subspecies present in a 1:1 ratio. Species 1: $g\perp = 2.124$, $g\parallel = 1.928$, $A\perp = 95$ MHz. Species 2: $g\perp = 2.255$, $g\parallel = 1.893$, $A\perp = 93$ MHz, $A\parallel = 150$ MHz. Instrument parameters: mw frequency = 9.3814 GHz, power = 0.6325 dB, attenuation = 25 dB, modulation frequency = 100 kHz, modulation amplitude = 4 G, receiver gain = 70 dB, time constant = 163.84 ms, conversion time = 10 ms.

To experimentally substantiate the computationally predicted $^2B_{1u}$-derived ground state with a $(\delta^*)^1$ orbital configuration of **2**, we turned our attention to spectroscopic studies. As shown previously, $Rh_2(esp)_2$ is not stable in the Rh_2(II,III) redox state, but in CH_2Cl_2 solution, it can be oxidized coulometrically to the corresponding Rh_2(II,III) species **2**. The coulometric oxidation was monitored by UV−vis spectroscopy, which showed near-isosbestic behavior indicative of oxidation to an isostructural product with the possibility of a partial transformation of the oxidized product via a chemical reaction. A sample of electrochemically generated **2** was frozen upon generation and analyzed by EPR spectroscopy. The EPR spectrum given in Figure 2.1 is surprising in two ways. First, the spectrum cannot be simulated by a single S = 1/2 species and therefore indicates that **2** actually contains two Rh_2(II,III) species that are similar in structure, as evidenced by the similarity of their axially symmetric EPR signals. Second, the best-simulated EPR g values, $g_\perp = 2.124$ and $g_\parallel = 1.928$ for the first species and $g_\perp = 2.255$ and $g_\parallel = 1.893$ for the second species, are indicative of a relatively simple S = 1/2 species with a single Kramers' doublet, excluding the

possibility of having a ground state with the $(\pi^*)^3$ orbital configuration for **2**. The observed g values instead fit well in the range of those observed for compounds with a ground state containing a $(\delta^*)^1$ orbital.[50] As for the reason that two EPR-active species are produced during coulometric oxidation of $[Rh_2(esp)_2]$, this is likely due to partial coordination of a solvent or electrolyte species in the axial site of the Rh_2 molecule to generate Rh_2 species such as $Rh_2(esp)_2Cl$, which has been observed in a high-resolution mass spectrum,[35] and is consistent with the imperfect isosbestic behavior of the oxidation. Notably, the EPR parameters predicted by DFT for **2**, $g_1 = 2.24$, $g_2 = 2.11$, $g_3 = 2.06$, differ in symmetry but are close to the experimental values.

Comparison of the DFT-calculated electronic state and aforementioned EPR data clearly shows that the utilized DFT approach provides an adequate description of the ground state wave function of **2** and its derivatives. Thus, DFT can be used to further explore the chemistry of these species.

Recently, Berry and co-workers have reported a new amidate-ligated catalyst, $Rh_2(espn)_2Cl$, **3_Cl**, which can form as any one of four possible isomers: the (cis-2,2)-, (4,0)-, (trans-2,2)-, and (3,1)-isomers. However, the synthesis of **3_Cl** results in two structural isomers (cis-2,2)-(**3_Cl**) and (4,0)-(**3_Cl**), with the cis-2,2 isomer favored in a 4:1 ratio.40 At low concentrations, **3_Cl** dissociates Cl^- in CH_2Cl_2 to form $[Rh_2(espn)_2]^+$, **3**, and it was possible to assign electrochemical features to both the Cl-bound and unbound species.[40]

We report here experimental EPR and XAS measurements aimed at elucidating the nature of the ground state of **3**. EPR data on the $[Rh_2(espn)_2L]^+$ complexes in solution are consistent with an S = 1/2 ground state for these species (

Figure 2.2). Indeed, the spectra of these compounds can be straightforwardly simulated by near-axial S = 1/2 signals showing ^{103}Rh hyperfine splitting of the $g_{\|}$ signal. The best simulations

of these favorably with those reported by Kadish, Bear, and co-workers on Rh_2(II,III) acetamidate analogues, which have $g_\perp = 2.11-2.13$, $g_\parallel = 1.89-1.92$, and $A_\parallel = 79-90$ MHz.[50] These data support the assignment of the GES with a $(\delta^*)^1$ configuration for **3**.

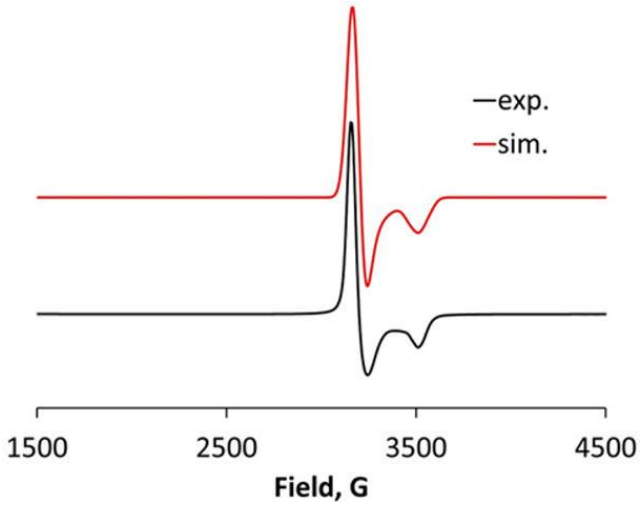

Figure 2.2. X-band EPR spectrum measured at 10 K of 4,0-Rh_2(espn)$_2$Cl. The spectrum is modeled with $g_\perp = 2.105$, $g_\parallel = 1.905$, and $A_\parallel = 135$ MHz. Instrument parameters: mw frequency = 9.3792 GHz, power = 0.6385 mW, attenuation = 25.0 dB, modulation frequency = 100 kHz, modulation amplitude = 4 G, receiver gain = 30 dB, time constant = 327.68 ms, conversion time = 10.0 ms.

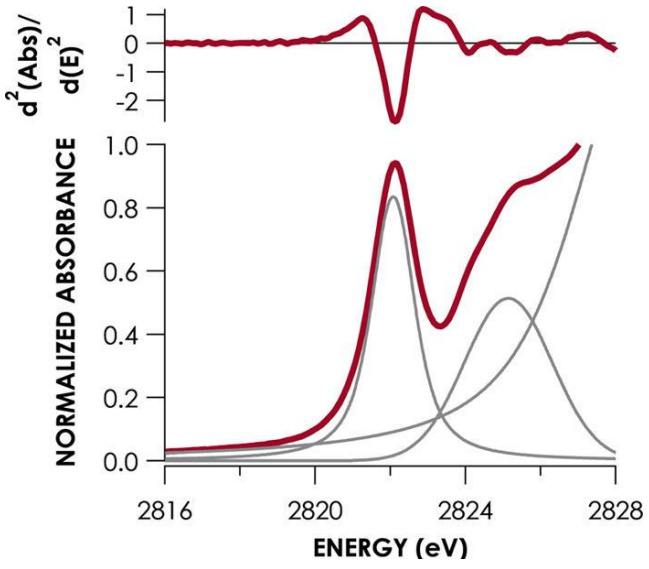

Figure 2.3. Pre-edge region and second derivative plot of (cis-2,2)-Rh_2(espn)$_2$Cl Cl K-edge XAS. Pseudo-Voigt peaks are shown in gray.

Another spectroscopic method that has not yet been used with metal−metal bonded

compounds but, in principle, can distinguish between the $(\pi^*)^3$ and $(\delta^*)^1$ states in $[Rh_2(II,III)]-Cl$ complexes is Cl K-edge X-ray absorption spectroscopy (XAS). Cl K-pre-edge transitions may be formally assigned as Cl 1s → "φ", where φ represents a molecular orbital of the form $[\alpha(Rh\ 4d) + 1 - \alpha^2\ (Cl\ 3p)]$. Here, the presence of Cl 3p character in partially unoccupied valence orbitals is required for nonzero Cl K-pre-edge intensity. From symmetry considerations, Cl character can be mixed into σ- or π-type orbitals in a linear Rh−Rh−Cl structure but cannot be mixed into δ-symmetry orbitals. Thus, a $(\pi^*)^3$ compound should display a pre-edge feature below the main σ* transition corresponding to the partially filled Rh_2 π* level, and a $(\delta^*)^1$ compound should not. Thus, in the case of the anticipated $(\delta^*)^1$ ground state of **3_Cl**, we expect to observe a Cl 1s → σ* pre-edge transition, whereas with a $(\pi^*)^3$ ground state, there would be an additional, resolvable lower-energy transition: Cl 1s → π*. The Cl pre-edge region for **3_Cl** is shown along with its corresponding second-derivative plot and least-squares fit in Figure 2.3. The pre-edge region comprises a single peak at 2822.1 eV. The presence of a single peak is consistent with a GES having a Rh−Rh δ* SOMO.

To support these experimental results, we have computationally investigated the (cis-2,2)- and (4,0)-isomers of $[Rh_2(espn)_2]^+$, **3**, $[Rh_2(espn)_2(H_2O)]^+$, **3_H₂O**, and $Rh_2(espn)_2Cl$, **3_Cl** species. Their calculated and experimental geometries at the ground doublet electronic states (with the unpaired electron in the Rh−Rh δ* orbital) are given in Table 2.4. One should mention that the (4,0)-(**3_L**) species could have two isomers, which differ by coordination of the L ligand to the Rh_2 center surrounded by either four N centers or four O centers. Below, we call these isomers $(4,0)_N$ and $(4,0)_O$, respectively. In general, the $(4,0)_N$-isomer is found to be energetically a few kJ/mol more favorable than the $(4,0)_O$-isomer for both doublet and quartet state species. The energy difference between these isomers is slightly larger for L = Cl than H_2O. For simplicity, below we

discuss only the energetically more stable $(4,0)_N$-isomers of **3_H₂O** and **3_Cl** species, but we include all energy and geometry results for the less stable $(4,0)_O$-isomers of 3_H_2O and **3_Cl** in the Supporting Information.

As seen from Table 2.4, in general, the calculated geometries of the doublet S = 1/2 GESs of **3**, **3_H₂O**, and **3_Cl** with the unpaired electron in the Rh−Rh δ* orbital match closely their experimental values. One major disagreement between the calculated and experimental structures occurs for (cis-2,2)-(**3_Cl**): the experimental structure of this species is polymeric, with Cl^- ions bridging an infinite chain of Rh_2 species. In contrast, its calculated structure is molecular with a monodentate Cl^- ligand. As a result, the Rh−Cl bond distance is severely underestimated in the calculation, which, in turn, leads to an overestimation of the Rh−Rh bond distance. Since the Cl-bridged structure is a feature only of the solid-state packing of this compound and is likely absent in homogeneous solution, the calculated structure is presumably a more accurate model for the compound in solution during catalysis.

Table 2.4. Calculated and Experimentally Available Important Geometry Parameters (Distances in Å) of the (cis-2,2) and (4,0) Isomers of $[Rh_2(espn)_2L]^+$, **3_L**, Species (L = None, H_2O, and Cl^-), at Their Lower-Lying Doublet (S = 1/2) and Quartet (S = 3/2) Electronic States

species	Rh−Rh	Rh−L_{ax}	Rh−N_{eq}	Rh−O_{eq}	*S*
		Calculated: This work			
(*cis*-2,2)-$[Rh_2(espn)_2]^+$	2.40		2.02	2.05	1/2
	2.47		2.03	2.06	3/2
(*cis*-2,2)-$[Rh_2(espn)_2(H_2O)]^+$	2.41	2.28	2.02	2.06	1/2
	2.48	2.48	2.03	2.08	3/2
(*cis*-2,2)-$[Rh_2(espn)_2Cl]$	2.46	2.42	2.01	2.08	1/2
	2.54	2.62	2.02	2.08	3/2
		Experiment[40]			
(*cis*-2,2)-$[Rh_2(espn)_2Cl]_n$	2.4155(9)	2.617(2)	1.970(6)	2.033(5)	1/2
		Calculated: This work			
(4,0)-$[Rh_2(espn)_2]^+$	2.40		2.05	2.03	1/2
	2.47		2.05	2.03	3/2
(4,0)-$[Rh_2(espn)_2(H_2O)]^+$	2.41	2.34	2.05	2.03	1/2
	2.50	2.43	2.05	2.05	3/2
(4,0)-$[Rh_2(espn)_2Cl]$	2.44	2.44	2.04	2.04	1/2
	2.51	2.55	2.07	2.05	3/2
		Experiment[40]			
(4,0)-$[Rh_2(espn)_2Cl]$	2.4136(4)	2.6165(9)	2.003(3)	1.998(2)	1/2

After elucidating the electronic and geometric structures of the aforementioned Rh_2(II,III)

species, we are well-positioned to discuss their redox potentials, which are vital for understanding the stability and reactivity of these species. Based on the above-presented comparison of DFT and experimental data, one may confidently use DFT methods to calculate redox potentials and provide insight into the proclivity for axial ligand binding of the Rh_2(II,III) species **2_L** and **3_L**. We excluded **1_L** species from reactivity studies due to the facts that (a) NTC by **1_L** has not been established to utilize the Rh_2(II,III) oxidation state and (b) the GES of **1** is multiconfigurational and, therefore, may not be accurately described by the DFT approach.

2.4.1.2 Energy Landscape: Redox Potentials and Axial Ligand Effects.

For $[Rh_2(esp)_2]^+$, **2**, experiments showed that the $\mathbf{2}^{0/+}$ redox potential is at 0.80 V vs Fc/Fc^+.[37, 58] DFT predicts a value of 0.78 V, which is in excellent agreement with the experimental value (see Scheme 2.2). The calculated $[\mathbf{2\_Cl}]^{0/-}$ redox potential is −0.72 V vs Fc/Fc^+. Since previous experiments showed that **2** strongly binds Cl^- ions,[35] we also calculated the impact of a second Cl^- ligand binding to $[Rh_2(esp)_2]^+$, **2**. It was found that the binding of two Cl^- ligands to **2** greatly lowers the Rh_2(II,II)/Rh_2(II,III) (in short, $Rh_2^{4+/5+}$) redox potential by 2.27 V. These findings show that increasing the concentration of chloride (or any other anionic axial ligand for that matter) in reaction mixture could strongly favor catalysis in the Rh_2(II,III) regime, though if the concentrations are too high, catalysis could be hindered by blocking of both axial sites.

Scheme 2.2. Energy Landscape of Compounds 2, 2_Cl, and 2_Cl_2[a]

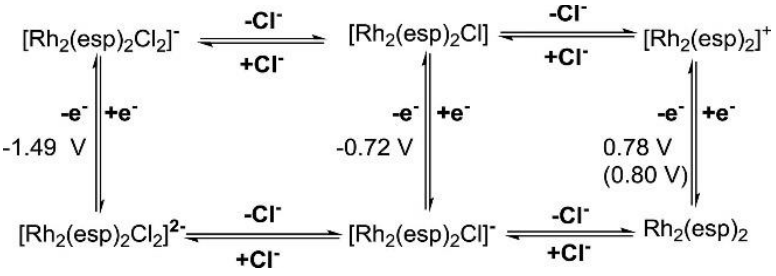

[a]DFT-calculated and experimental redox potentials are given without and with parentheses.

As mentioned above, experiments showed that complex **3_Cl** could have several isomers

among which the (cis-2,2)- and (4,0)-isomers are experimentally observed, with the cis-2,2-isomer favored in a 4:1 ratio.[40] Consistent with this finding, DFT calculations predict the (cis-2,2)_(**3_Cl**)-isomer to be lower in energy than the (4,0)-isomer by 12.1 kJ/mol (see Scheme 2.3). Dissociation of the axial chloride leads to the active cationic catalyst, $[Rh_2(espn)_2]^+$, the (cis-2,2)-**3** isomer of which is higher in energy by 15.5 kJ/mol than its (4,0)-**3**-isomer. The four nitrogen atoms bound to the high-oxidation state Rh^{III} center in the (4,0)-isomer, therefore, appear to provide greater stabilization to the Rh atom than two nitrogen and two oxygen atoms than in the (2,2)-isomer.

Scheme 2.3. Energy Landscape of Compounds (cis-2,2)-**3**, (cis-2,2)-(**3_Cl**), (4,0)-**3**, and (4,0)-(**3_Cl**)[a]

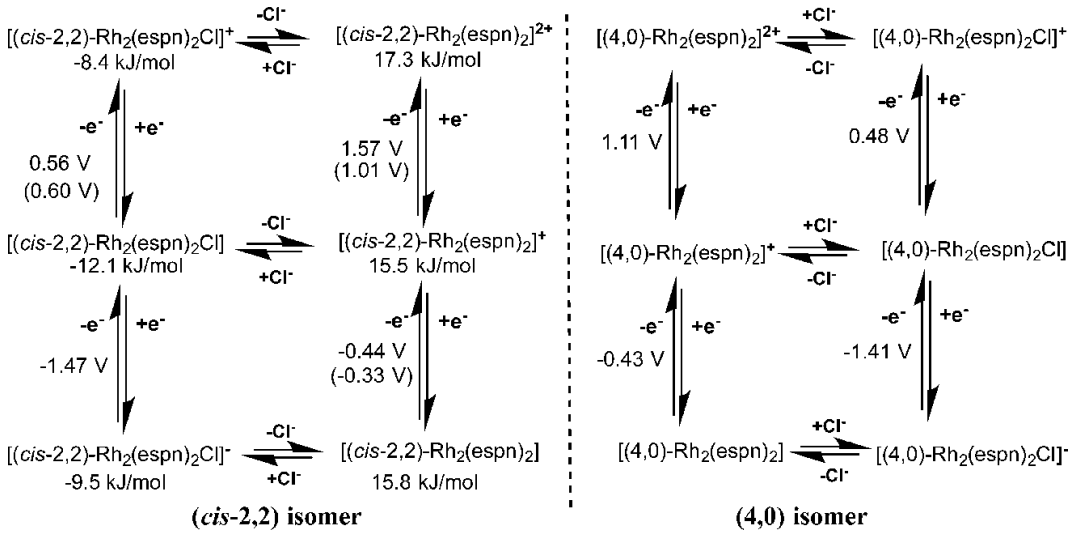

[a]DFT-calculated and experimental redox potentials (listed relative to the Fc/Fc+ couple) are given without and with parentheses, respectively. Presented relative energies (in kJ/mol) are listed relative to the corresponding (4,0)-isomers.

Cyclic voltammetry experiments were performed for (cis-2,2)-**3**, which showed two reversible waves corresponding to $[Rh_2(espn)_2]^{0/+}$ at −0.33 V and $[Rh_2(espn)_2]^{+/2+}$ at 1.01 V. A third quasi-reversible peak was observed at 0.60 V, which was assigned to the chloride-bound $[Rh_2(espn)_2Cl]^{0/+}$ redox couple.[40] For (cis-2,2)-**3**, DFT calculations predicted the $[Rh_2(espn)_2]^{0/+}$ couple at −0.44 V and the $[Rh_2(espn)_2]^{+/2+}$ couple at 1.57 V. The $[Rh_2(espn)_2Cl]^{0/+}$ couple is predicted at 0.56 V. Here, the agreement between calculated and experimentally measured redox

potentials is superb, providing excellent support for the assignments of these waves as well as validation for the DFT methods used (see Computational Methods for more details). The one exception is the redox couple involving the dicationic species $[(cis\text{-}2,2)\text{-}Rh_2(espn)_2]^{2+}$, where the discrepancy is likely the result of stronger solvation effects on the energy of the dication. For the (4,0)-isomer of **3**, the $[Rh_2(espn)_2]^{0/+}$ couple was predicted at −0.43 V and the $[Rh_2(espn)_2]^{+/2+}$ couple at 1.11 V. The $[Rh_2(espn)_2Cl]^{0/+}$ couple was predicted at 0.48 V. All of the calculated and measured redox potentials are summarized in Scheme 2.3.

This analysis of Rh_2 electronic states and redox potentials now positions us to investigate catalytically relevant intermediates of the mixed-valent Rh_2(II,III) complexes **2_L** and **3_L** and study mechanistic details of C−H amination catalyzed by these systems, where L = none, H_2O, and Cl.

2.4.2 Rh_2(II,III) Nitrene Complexes and Mechanism of Intramolecular C−H Amination.

2.4.2.1 Electronic Structure of the Rh_2(II,III)-Nitrene Intermediates.

As mentioned above (see Scheme 2.1), one of the most important intermediates of both intra- and intermolecular C−H amination by the mixed valent Rh_2(II,III) species under oxidative NTC conditions is the transient Rh_2(II,III)-nitrene complex. Since isolation and characterization of these transient complexes has, to date, not been possible, DFT and CASSCF computations, validated above, appear to be the most valuable tool to study the electronic and geometric structures, as well as reactivity of these species.

Table 2.5. Calculated Important Geometry Parameters (Distances in Å and Angles in deg) of the $\{Rh_2(esp)_2[NSO_3(CH_2)_3Ph](L)\}^+$, **2N_L**, Species (L = None, H_2O, and Cl^-), at Their Doublet (S = 1/2) and Quartet (S = 3/2) Electronic States

species	*S*	Rh−Rh	Rh−N	Rh−L	Rh−Rh−L	Rh−Rh−N	Rh−N−S
2N	1/2	2.40	1.92			176	122
	3/2	2.42	1.95			172	125
2N_H_2O	1/2	2.39	1.93	2.31	167	170	129
	3/2	2.42	2.00	2.35	174	170	126
2N_Cl	1/2	2.44	1.93	2.34	165	161	126
	3/2	2.46	2.03	2.40	172	169	124

DFT calculations were used to optimize structures of the **2N_L** and **3N_L** nitrene complexes of the species **2_L** and **3_L**, respectively, as described in more detail in the Computational Methods section. The results are given in Table 2.5 and Table 2.6. In all structures, the Rh−Rh distances of 2.39−2.48 Å are not much changed from those of **2_L** and **3_L**. Importantly, the addition of an L ligand has little effect on the Rh−Rh distances but elongates the Rh−N_{ax} bond distance, more notably in the doublet state for **2N_L**, but the effect is seen in both spin states of **3N_L** compounds. Interestingly, in doublet **2N**, the C^1–H^1 bond of the nitrene fragment interacts with the N center and, already, is partly activated with C^1–H^1, N–H^1, and Rh–N distances of 1.15, 1.65, and 1.92 Å, respectively (see also

Figure 2.8).

Table 2.6. Calculated Important Geometry Parameters (Distances in Å and Angles in deg) of the $\{Rh_2(espn)_2[NSO_3(CH_2)_3Ph](L)\}^+$, **3_L**, Species (L = None, H_2O, and Cl^-), at Their Doublet (S = 1/2) and Quartet (S = 3/2) Electronic States

species	*S*	Rh−Rh	Rh−N_{ax}	Rh−L_{ax}	Rh−N_{eq}	Rh−O_{eq}	Rh−Rh−L	Rh−Rh−N	Rh−N−S
(*cis*-2,2)-**3N**	1/2	2.46	1.94		2.02	2.08		174	119
	3/2	2.45	1.94		2.02	2.09		173	119
(*cis*-2,2)-**3N_H_2O**	1/2	2.44	1.99	2.39	2.03	2.07	174	171	129
	3/2	2.44	1.98	2.39	2.03	2.07	175	171	127
(*cis*-2,2)-**3N_Cl**	1/2	2.48	2.04	2.45	2.02	2.08	167	172	123
	3/2	2.48	2.03	2.46	2.02	2.09	166	172	123
(4,0)-**3N**	1/2	2.48	1.92		2.04	2.07		176	117
	3/2	2.43	1.96		2.05	2.02		176	127
(4,0)-**3N_H_2O**	1/2	2.44	2.00	2.34	2.06	2.03	174	172	128
	3/2	2.44	2.00	2.34	2.06	2.03	175	171	126
(4,0)-**3N_Cl**	1/2	2.48	2.04	2.45	2.02	2.09	166	172	123
	3/2	2.47	2.03	2.47	2.03	2.06	174	170	126

In all **2N_L** and **3N_L** complexes, the doublet and quartet states are predicted by DFT to be quite close in energy. For the **2N_L** series, the doublet states are predicted to be lowest in energy by 9.6 and 13.8 kJ/mol with L = none and Cl^-, respectively. The aquo complex is predicted to have

the quartet state lower in energy by (a practically negligible) 4.6 kJ/mol. For the **3N_L** compounds, the quartet states are all lower in energy, presumably due to the higher destabilization of the δ* orbital by the more electron-donating equatorial N donors. The energy differences to the doublet states range from 9 to 15 kJ/mol for the cis-(2,2)-isomers and from 8 to 11 kJ/mol for the (4,0)-isomers.

Chart 2.2. Molecular Orbital Ordering of [Rh−Rh]−NSO_3R Compounds[a]

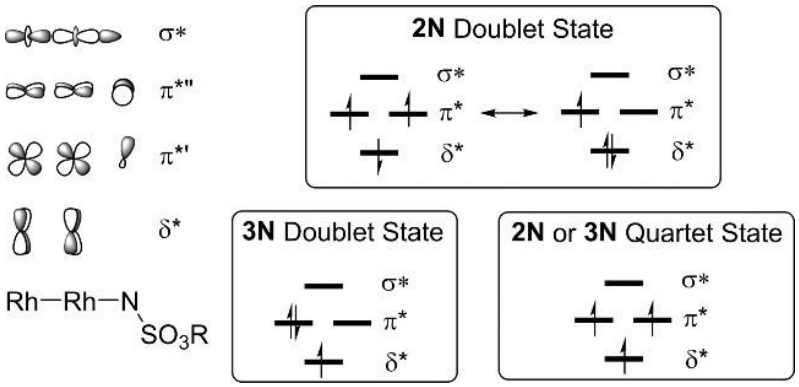

[a]Highlighted electron configurations are of the doublet and quartet states. Only the major electron configuration is shown in each case. Two π* orbitals are shown as degenerate only for simplicity.

In general, the sulfamate nitrene can utilize its σ and two π orbitals to form bonds with the σ- and π-symmetry orbitals of the Rh_2(II,III) core, similar to those previously described for Rh_2-carbene and Ru_2-nitride compounds.[59-67] The important frontier orbitals of the nitrene complexes are the Rh_2-centered δ* orbital, two three-center Rh−Rh−N π* orbitals, and the three-center Rh−Rh−N σ* orbital (see Chart 2.2). The δ* and π* orbitals are expected to be close in energy, as is well-known in other Rh_2 and Ru_2 systems with a similar electron count.[3, 61, 63, 65-68] However, the π* orbitals are expected to differ in energy since one of these two orbitals, denoted π*′, is also involved in the N−S bond of the bent nitrene unit. Thus, the similar energies of the doublet or quartet states for the nitrene complexes are derived from configurations with differing population of the δ* and π* levels. The configuration of the quartet state is $(\delta^*)^1(\pi^{*\prime})^1(\pi^{*\prime\prime})^1$, but there are several possible doublet configurations to consider. Importantly, the major acceptor orbitals for

electrophilic reactivity are the Rh−Rh−N π* orbitals, which are polarized toward the N atoms.

Due to the several possible electron configurations for the doublet state, we may expect the doublet states of **2N** and **3N** to be multiconfigurational, with three valence electrons in the near-degenerate δ*, π*′, and π*″ orbitals. To gauge the importance of this effect, and to extract a useful description of the bonding in these compounds, both DFT and CASSCF calculations on **2N** and **3N** complexes were performed with the simplifying truncation of CH_3 for the organic substituent on the nitrene group (labeled **2N′** and **3N′**). Two distinct DFT models for doublet-state **2N′** were considered containing either a singlet or triplet nitrene coordinated to the Rh_2 unit. As shown in Table S1, these two configurations are nearly isoenergetic but have drastically different spin distributions. For reference, the DFT frontier orbitals of the singlet nitrene configuration are shown in Figure S1. A similar situation arises when the doublet state of **3N′** is examined by DFT methods (Table S1). Two drastically differing doublet states are found to be different by only ∼8 kJ/mol. Due to the ambiguity in the DFT-calculated electronic structure, further analysis of the bonding in these intermediates was made using CASSCF.

Table 2.7. Leading Configurations from CASSCF Calculations on **2N′** and **3N′** in Doublet and Quartet States

complex	S	active space	CSFs[a]	weight (%)
2N′	1/2	(19,12)	$(\pi''_{nb})^2(\sigma_{nb})^2(\delta^*)^2(\pi'^*)^1(\pi''^*)^0(\sigma^*)^0$	46.5
			$(\pi''_{nb})^2(\sigma_{nb})^2(\delta^*)^0(\pi'^*)^1(\pi''^*)^2(\sigma^*)^0$	26.3
			$(\pi''_{nb})^2(\sigma_{nb})^2(\delta^*)^1(\pi'^*)^1(\pi''^*)^1(\sigma^*)^0$	16.7
2N′	3/2	(19,12)	$(\pi''_{nb})^2(\sigma_{nb})^2(\delta^*)^1(\pi'^*)^1(\pi''^*)^1(\sigma^*)^0$	90.5
3N′	1/2	(19,12)	$(\pi''_{nb})^2(\sigma_{nb})^2(\delta^*)^1(\pi'^*)^2(\pi''^*)^0(\sigma^*)^0$	71.5
			$(\pi''_{nb})^0(\sigma_{nb})^2(\delta^*)^1(\pi'^*)^2(\pi''^*)^2(\sigma^*)^0$	14.9
			$(\pi''_{nb})^1(\sigma_{nb})^2(\delta^*)^1(\pi'^*)^2(\pi''^*)^1(\sigma^*)^0$	3.21
3N′	3/2	(19,12)	$(\pi''_{nb})^2(\sigma_{nb})^2(\delta^*)^1(\pi'^*)^1(\pi''^*)^1(\sigma^*)^0$	83.5

[a]CSFs = configuration state functions. All CSFs have six further doubly filled active orbitals.

Table 2.8. Selected Spin Populations in **2N′** and **3N′**, Derived from the CASSCF Wave Functions

complex	S	Mulliken spin population[a]		
		N	Rh_m[b]	Rh_d[b]
2N′	1/2	1.05	0.12	−0.23
2N′	3/2	1.68	0.08	1.07
3N′	1/2	−0.07	0.02	0.93
3N′	3/2	1.09	0.55	1.12

[a]Residual spin populations are located primarily on the SO_3CH_3 group. [b]Rh_m = middle rhodium; Rh_d = distal rhodium.

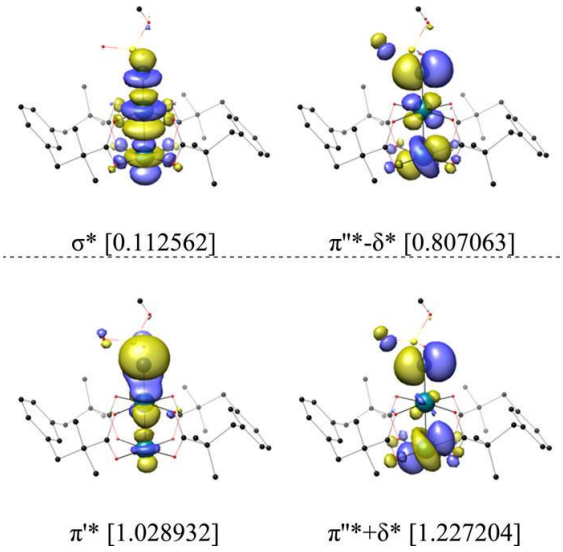

Figure 2.4. Natural frontier orbitals of doublet 2N′ from CASSCF. Occupation numbers are shown in brackets.

The CASSCF electronic configurations of **2N′** and **3N′** and their corresponding weights are given in Table 2.7 and Table 2.7. Leading Configurations from CASSCF Calculations on **2N′** and **3N′** in Doublet and Quartet States

complex	S	active space	CSFs[a]	weight (%)
2N′	1/2	(19,12)	$(\pi''_{nb})^2(\sigma_{nb})^2(\delta^*)^2(\pi'^*)^1(\pi''^*)^0(\sigma^*)^0$	46.5
			$(\pi''_{nb})^2(\sigma_{nb})^2(\delta^*)^0(\pi'^*)^1(\pi''^*)^2(\sigma^*)^0$	26.3
			$(\pi''_{nb})^2(\sigma_{nb})^2(\delta^*)^1(\pi'^*)^1(\pi''^*)^1(\sigma^*)^0$	16.7
2N′	3/2	(19,12)	$(\pi''_{nb})^2(\sigma_{nb})^2(\delta^*)^1(\pi'^*)^1(\pi''^*)^1(\sigma^*)^0$	90.5
3N′	1/2	(19,12)	$(\pi''_{nb})^2(\sigma_{nb})^2(\delta^*)^1(\pi'^*)^2(\pi''^*)^0(\sigma^*)^0$	71.5
			$(\pi''_{nb})^0(\sigma_{nb})^2(\delta^*)^1(\pi'^*)^2(\pi''^*)^2(\sigma^*)^0$	14.9
			$(\pi''_{nb})^1(\sigma_{nb})^2(\delta^*)^1(\pi'^*)^2(\pi''^*)^1(\sigma^*)^0$	3.21
3N′	3/2	(19,12)	$(\pi''_{nb})^2(\sigma_{nb})^2(\delta^*)^1(\pi'^*)^1(\pi''^*)^1(\sigma^*)^0$	83.5

[a]CSFs = configuration state functions. All CSFs have six further doubly filled active orbitals.

Table 2.8. The natural orbitals of the multiconfigurational wave function are shown in Figure **2.4** and Figure 2.5. Both quartet states are quite similar, with the anticipated $(\delta^*)^1(\pi^{*\prime})^1(\pi^{*\prime\prime})^1$ configurations and spin delocalized throughout the Rh−Rh−N unit. The doublet states of **2N′** and **3N′** are electronically distinct. As seen in Figure **2.4**, there is significant mixing of the orbitals of δ* and π*″ symmetry in **2N′** leading to some fluidity in its electronic structure. We may describe the electronic structure as a resonance hybrid between a $(\delta^*)^2(\pi^{*\prime})^1(\pi^{*\prime\prime})^0$ configuration and an antiferromagnetic $(\delta^*)^d(\pi^{*\prime})^u(\pi^{*\prime\prime})^u$ configuration (here d and u denote spin-down and spin-up, respectively). The former configuration may be described in valence bond terms as having a Rh_2(II,II) unit with a coordinated nitrene radical cation, while the latter configuration indicates a Rh_2(II,III) species that is antiferromagnetically coupled to a triplet nitrene group. The view that both of these configurations contribute to the ground state is supported by the Mulliken spin populations showing very little (but negative) spin on the Rh centers and 1.05 spin on the nitrene N atom. It is remarkable that the calculations support partial oxidation of the nitrene moiety, itself a strong oxidant, by the $Rh_2(esp)_2^+$ core. This result is, however, in agreement with the high $Rh_2(esp)_2^{0/+}$ redox potential, but since we have shown the redox potentials to drop considerably upon chloride binding, it is likely that the electronic structure will change significantly as a function of the axial ligands.

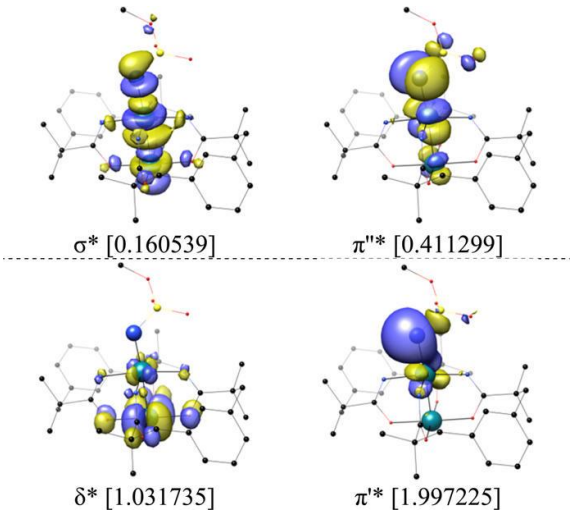

Figure 2.5. Natural frontier orbitals of doublet **3N′** from CASSCF. Occupation numbers are shown in brackets.

As expected from the greater stabilization of higher oxidation states by espn, the major configuration of **3N′**, $(\delta^*)^1(\pi'^*)^2(\pi''^*)^0$, is best described as consisting of a Rh_2(II,III) unit coordinated by a singlet nitrene species (see the orbitals and occupation numbers given in Figure 2.5). Here, the spin population is clearly localized on the Rh_2 unit. In each case, there are other minor configurations contributing up to 26% of the wave function that are due to double and single excitations from the main configuration.

It is instructive at this juncture to compare the electronic structure of **2N′** and **3N′** to Co−porphyrin complexes, which have been shown to undergo metal-centered oxidation upon the binding of alkyl sulfamate nitrenes to give Co(III)(Por)-($NSO_3R^{\bullet-}$) species.[69] As shown in Figure 2.6, the electronic structures of both **2N′** and **3N′** are quite different from that of the Co species. One reason for this difference can be understood from the redox potentials of the respective catalysts. **2** exhibits a $Rh_2^{4+/5+}$ couple at 0.78 V vs Cp_2Fe, and 3 exhibits a $Rh_2^{5+/6+}$ couple at 1.57 V vs Cp_2Fe in CH_2Cl_2 (vide supra). In contrast, Co(TPP) (TPP = tetraphenylporphyrin) has been shown to exhibit three oxidation waves at 0.24, 0.45, and 0.61 V vs Cp_2Fe in CH_2Cl_2, corresponding to one metal-centered and two ring-centered oxidations, respectively.[70] Thus, Co(II)

is able to reduce the nitrene group to a radical anion while neither the $Rh_2(esp)_2^+$ core nor the $Rh_2(espn)_2^+$ core is reducing. In fact, $Rh_2(esp)_2^+$ is highly oxidizing, and there is a contribution to the GES of **2N′** from a Rh_2(II,II) species bearing a nitrene radical cation. In contrast, the $Rh_2(espn)_2^+$ core is content in the Rh_2(II,III) oxidation state and supports a bound singlet nitrene. In addition to the difference in the redox potentials, there is also a difference in the mechanism of C−H amination between the Co(Por) system, which has been proposed to proceed via a stepwise mechanism,[71] whereas we propose here that both Rh_2 systems operate via a concerted mechanism (vide infra).

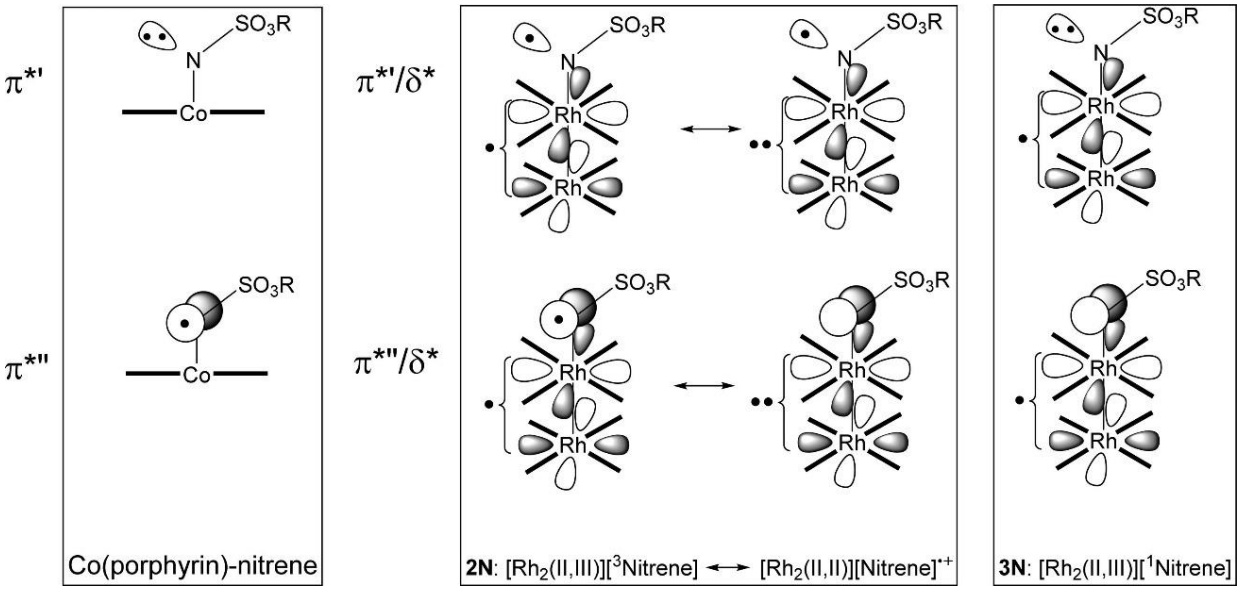

Figure 2.6. Comparison of the electronic structure of Co−porphyrin−nitrene$^{\bullet-}$ species (left) with **2N′** (center) and **3N′** (right). Here, the two π-symmetry orbitals are shown separately and localized on N, and in the Rh_2 cases, the δ* electrons are also shown.

We further investigated, at the DFT level, both doublet and quartet potential energy surfaces for C−H amination via the nitrene complexes $\{Rh_2(esp)_2(L)[NSO_3(CH_2)_3Ph]\}^{n+}$, **2N_L**, and $\{Rh_2(espn)_2(L)[NSO_3(CH_2)_3Ph]\}^{n+}$, **3N_L**, keeping in mind the caveat that the doublet states are multiconfigurational and that the DFT description of their electronic structure does not explicitly take this complexity into account. A full analysis of the potential energy surfaces at the

CASSCF level cannot be performed because it is prohibitively expensive.

2.4.2.2 Mechanistic Details of Intramolecular C−H Amination via 2N_L and 3N_L Nitrene Complexes.

There are two limiting mechanisms for nitrenoid C−H amination that should be considered: concerted (C) and stepwise (S) insertion of the nitrene into a substrate C−H bond (Scheme 2.4). In the C mechanism, there is a single transition state leading to C^1–N bond formation, C^1–H^1 bond cleavage, and N−H^1 bond formation. The S mechanism starts by hydrogen atom (H1) transfer (HAT) to produce a protonated nitrene radical anion and a benzylic radical followed by radical recombination to yield the products. Unpaired spin density on the nitrene N atom is often naively suggested to support HAT in an S mechanism, but there are strong kinetic and thermodynamic arguments against such generalizations.[72] Below, we develop an electronic structure-based approach to understand the differences between a C and S mechanism.

Scheme 2.4. Schematic Presentation of the Concerted (C) and Stepwise (S) Mechanisms of Intramolecular Nitrene Insertion into a Substrate C−H Bond in the **2N_L** and **3N_L** Nitrene Complexes

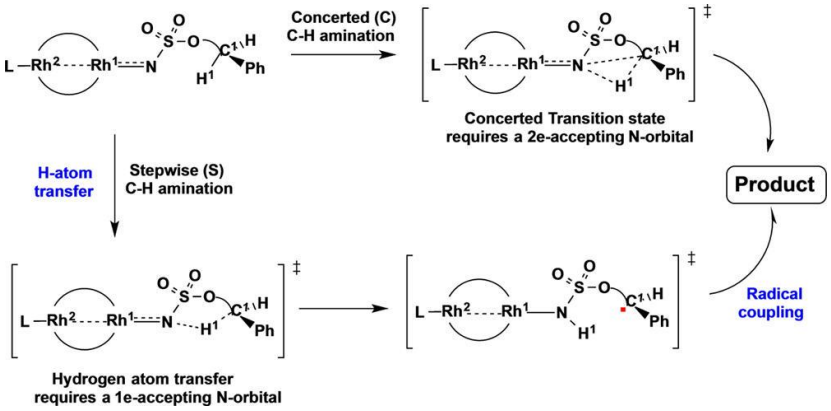

If we consider the orbital requirements for a C mechanism, the three-membered N–C^1–H^1 ring of the transition state will require one orbital from each of the nuclei involved: a N p orbital (or sp^x hybrid), a C^1 p- or sp^x-hybrid orbital, and a H^1 1s orbital. The stabilization of a three-membered ring with three orbitals requires the presence of two electrons to form a 3c/2e bond.

These two electrons obviously originate from the C^1−H^1 bond of the substrate. Thus, this mechanism requires an empty (but energetically accessible) N-centered orbital that can accept two electrons from the C−H bond. The electronic requirements of the S mechanism are different. This mechanism relies on an HAT step and requires the N atom to accept a single electron. Therefore, this mechanism requires either an empty or half-filled N-centered orbital capable to accept the incoming H^1 atom with one unpaired electron. Based on the aforementioned discussion, it can be expected that intramolecular C−H amination in the doublet state nitrene complexes with an empty and easily accessible Rh−Rh−N π* orbital will proceed via a C mechanism. On the other hand, the same process in the quartet state nitrene complexes, having two half-filled Rh−Rh−N π* orbitals, is expected to proceed via the S mechanism. Thus, the spin state of the nitrene intermediate is expected to play a significant role in determining the mechanism of C−H amination. This is not a consequence of differing spin population but orbital populations. Considering the electronic structure in Figure 2.6, one can easily see why the Co−porphyrins use an S mechanism.

Armed with the aforementioned electronic structure-based prediction of the reactivity of the **2N_L** and **3N_L** nitrene species, we set out to investigate the mechanisms (energy and geometries of all transition states, intermediates, and products) and controlling factors of intramolecular benzylic C−H bond amination in $NSO_3(CH_2)_3Ph$. Since the calculated energy difference between the doublet and quartet states of both starting **2N_L** and **3N_L** nitrene species is relatively small and is strongly dependent on the chemical compositions of these complexes, one may not clearly suggest which electronic state (doublet or quartet) of the **2N_L** and **3N_L** species is responsible in the amination reaction in experiments. In principle, depending on the concentrations of exogenous L ligands in solution, any of these electronic states of both **2N_L** and **3N_L** nitrene species could be a catalytically important one. Therefore, we studied the mechanisms

of the intramolecular benzylic C−H bond amination with the $NSO_3(CH_2)_3Ph$ ligand for all these species at their lowest energy doublet and quartet states. The calculated important intermediates, transition states, and products of these reactions with their relative free energies are given in Figure **2.7**. Representative transition state structures are given in

Figure **2.8**. More details of all these structures are given in the Supporting Information.

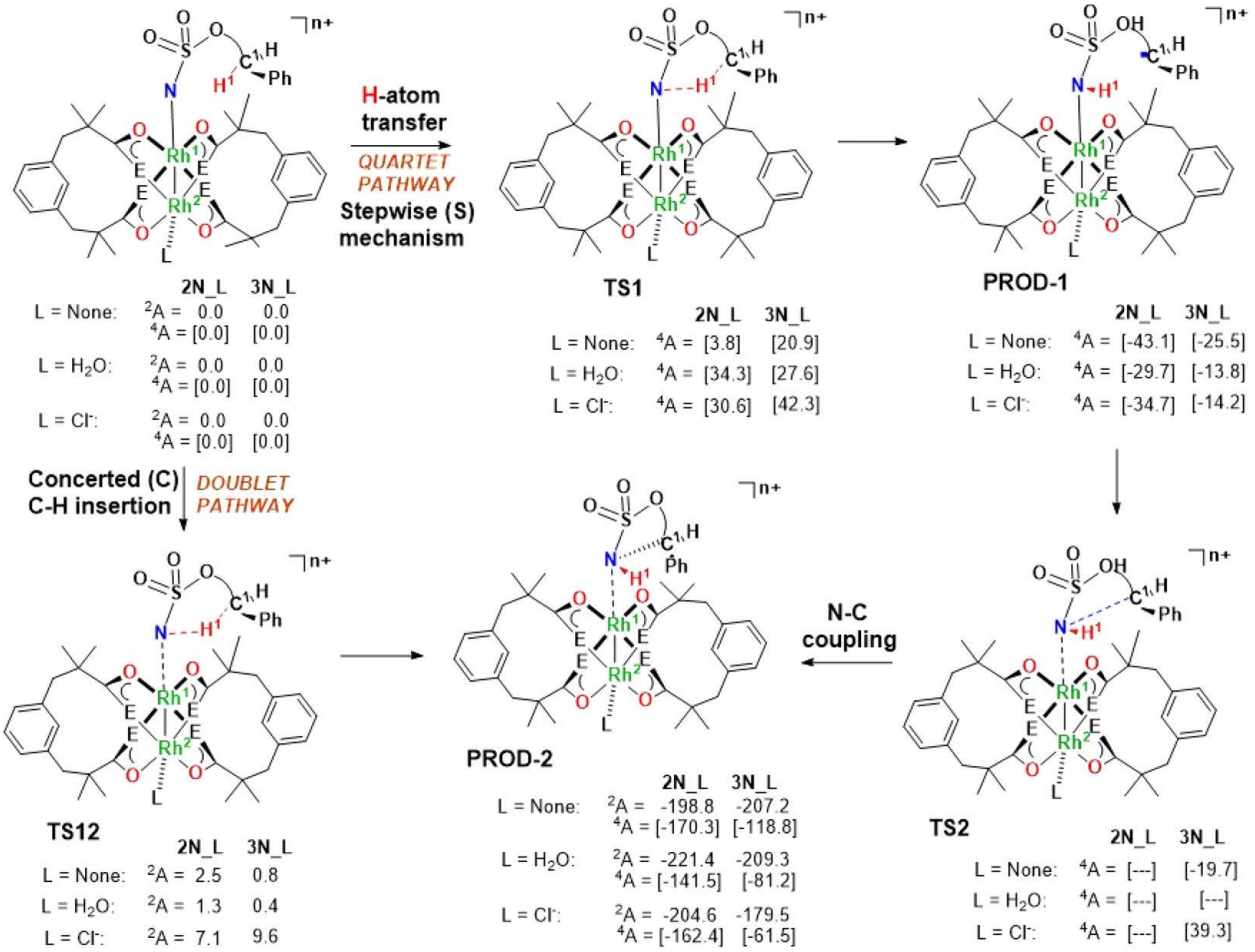

Figure 2.7. Schematic representation of the calculated reactants, intermediates, transition states, and products, alone with their relative energies (relative to the corresponding reactants, in kJ/mol), of the intramolecular C−H amination in the **2N_L** and **3N_L** nitrene complexes.

The exact mechanism of C−H amination is expected to depend strongly on the spin state of the nitrene reactant. As seen in Figure **2.7**, all doublet nitrene species uniformly undergo nearly barrierless (0.4−9.6 kJ/mol, at the transition state TS12), concerted insertion of the nitrene into the C^1–H^1 bond. On the other hand, the quartet nitrene species undergo stepwise C^1–H^1

functionalization via a mechanism involving (1) H^1 atom abstraction with energy barriers of 3.8−42.3 kJ/mol, TS1, followed by (2) radical recombination, TS2. The recombination step is essentially barrierless for the **2N** species but for **3N** is uphill from the intermediate PROD-1 by 5.8−53.5 kJ/mol, due to the different occupancies of the π* orbitals, depending strongly on the identity of L.

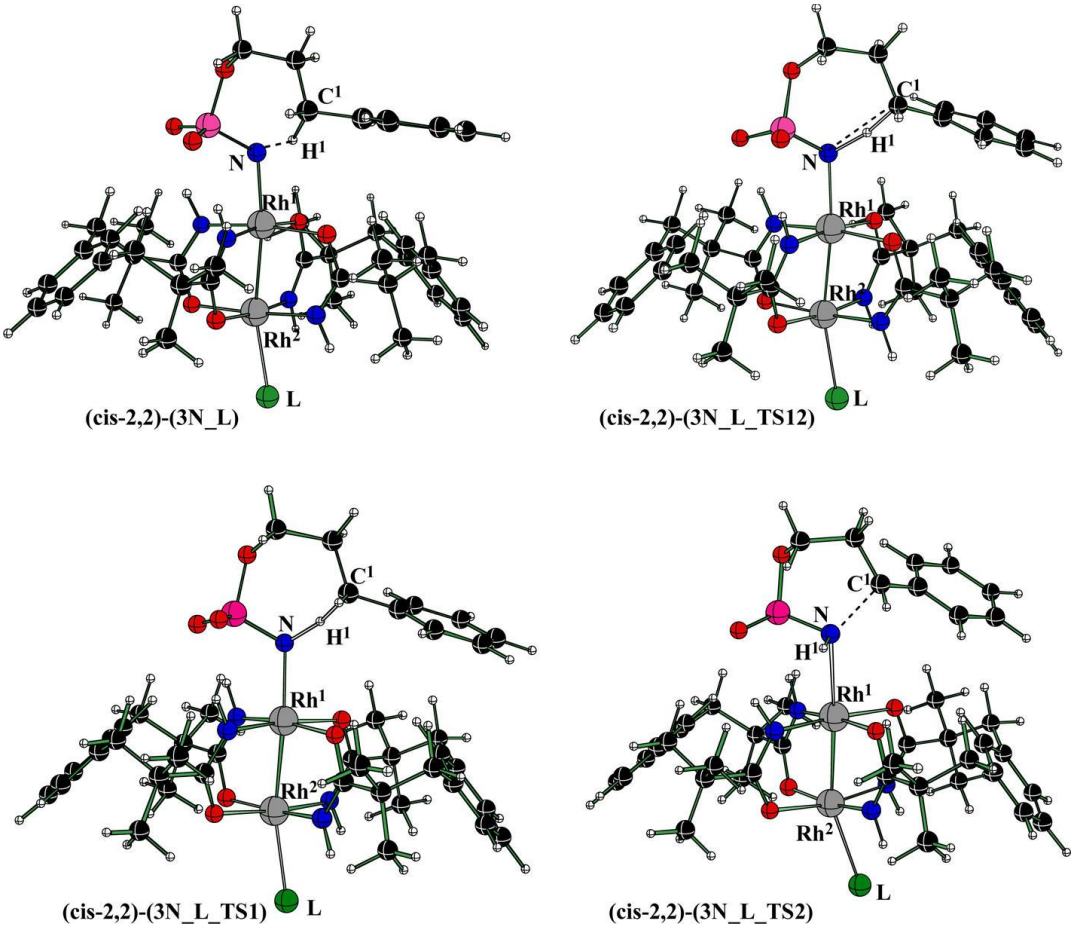

Figure 2.8. Calculated structures of the nitrene complex, and transition states TS1, TS2, and TS12. The structures of L = Cl^- are shown here as an example. See Supporting Information for similar structures for other species.

While it is tempting to assign the concerted pathway as the lowest-energy pathway and therefore the preferred pathway for catalysis, we must also keep in mind that in **3N_L** the quartet states are lower in energy and spin crossover to the doublet surface would be necessary in order to access the fastest rates of the doublet potential energy surface (see Scheme 2.5).[73-74] However, we

should also consider that formation of **3N** is most likely to take place on a doublet surface ($^2Rh_2(II,III) + {}^1PhINSO_3R \rightarrow {}^2$3N + PhI). The main assumption underlying the proposed two-state reactivity for **3N** is that spin-state crossover is fast compared to the other barriers involved in nitrene formation and C−H amination. Under this assumption, the energy barriers are necessarily steeper for the **3N_L** compounds than their **2N_L** analogues since the former must undergo a spin-state change.

Scheme 2.5. Simplified Reaction Coordinate Diagram for C−H Amination by $Rh_2(II,III)$ Complexes

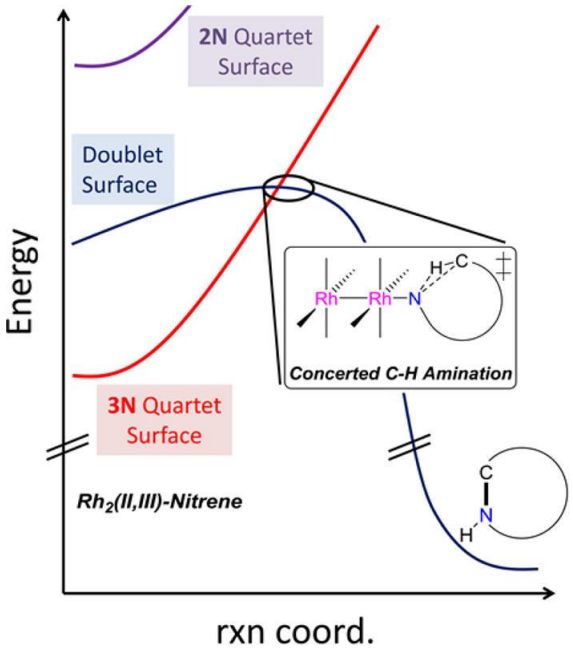

One way to assess the computed reaction pathways is comparison of the predicted and measured kinetic isotope effect (KIE) of the reactions. We have experimentally determined the KIE under identical conditions for compounds 2 and 3 (see Chart 2.3), which are 2.9 and 2.6, respectively. These are remarkably similar, especially considering that catalyst **2** is proposed to utilize both a $Rh_2(II,III)$ and a $Rh_2(II,II)$ mechanism. In comparison, the KIE for **1**, 1.9,76 is somewhat smaller and may suggest that a $Rh_2(II,III)$ pathway is not viable for 1.77(We note that this KIE increases to 2.6 when one uses a longer delay time on the ^{13}C NMR acquisition, as

described in ref 64. Thus, we cannot completely rule out a Rh_2(II,III) pathway for $Rh_2(OAc)_4$) Undoubtedly, the KIE must be a product of all of the potential mechanisms and can even change over the course of a reaction if the nature of the active catalyst is changing, as is likely the case here. Given that KIEs of ~2 are established for concerted nitrene transfer reactions, whereas values of ~6 are associated with HAT steps, the experimental KIE values are more suggestive of a concerted intramolecular nitrene insertion mechanism.[75]

Chart 2.3. Reaction and Conditions for Experimental KIE Measurement

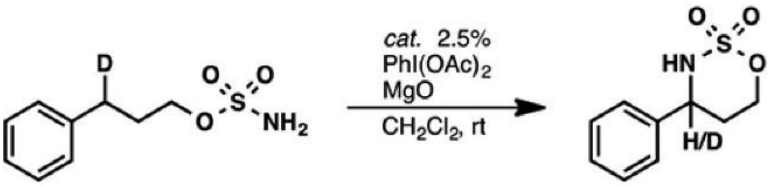

In agreement with this assessment, the calculated KIE values are 3.1, 2.3, and 2.8 for doublet state **2_N_L** with L = none, H_2O, and Cl^-, respectively, while the corresponding values for the quartet surface are 6.3, 6.1, and 5.9. For the 3_N_L catalysts (L = none, H_2O, and Cl^-), the doublet KIEs are calculated to be 2.5, 1.8, and 2.1 and the quartet values are 5.9, 6.3, and 5.4. Thus, the calculated KIEs are significantly larger for the quartet state pathways than they are on the doublet state analogues. Moreover, the quartet values are too large compared to the experimental values. Thus, the doublet transition state appears to be the most important one for defining the C−H amination pathway despite the fact that the **3N_L** nitrene intermediates favor a quartet ground state. It is worth mentioning that since the exact identities of catalytic intermediates and active oxidant remain obscure at this time, we cannot hope to achieve better agreement between the experimental and computed KIEs.

2.5 Conclusion

From the above presented joint computational and experimental studies, we may draw the

following conclusions.

(a) Rh_2(II,III) tetracarboxylate complexes, $[Rh_2^{II,III}(O_2CCH_3)_4(L)_n]^+$ (**1_L**) (L = none, Cl^-, and H_2O), have a ^2E_g-derived ground electronic state with degenerate π* orbitals and a $(\pi^*)^3$ valence electronic configuration; therefore, the electronic structure of these compounds cannot be adequately modeled at the DFT level. CASSCF calculations of the EPR g values are in good agreement with their experimental values.

(b) Unlike typical Rh_2(II,III) tetracarboxylates, $[Rh_2(esp)_2(L)_n]^{m+}$, **2_(L)$_n$**, and $[Rh_2(espn)_2(L)_n]^{m+}$, **3_(L)$_n$** [where L = none with m = 1, L = H_2O, n = 1 or 2, with m = 1, L = Cl^-, n = 1, with m = 0, and L = Cl^-, n = 2, with m = −1], species have a $^2B_{1u}$-derived ground electronic state with a $(\delta^*)^1$ valence electronic configuration, as evidenced by EPR spectroscopy and Cl K-edge XAS. Importantly, this state is not a multireference state and, therefore, can be modeled well using DFT methods.

(c) Nitrene complexes **2N_L** and **3N_L** of $[Rh_2(esp)_2(L)_n]^{m+}$, **2_(L)n**, and $[Rh_2(espn)_2(L)_n]^{m+}$, **3_(L)$_n$**, respectively, are proposed to be reactive intermediates in C−H amination. For **2N**, a complex multideterminental doublet state is predicted to be lowest in energy, whereas **3N** favors a high spin quartet ground electronic state with a $(\delta^*)^1(\pi^*)^2$ valence electronic configuration. Binding π-donor axial ligands destabilizes the quartet state.

(d) The calculated energy barriers for stepwise C−H amination in the quartet state are found to be uniformly higher than for concerted C−H amination in the doublet state. While **2N** is able to access the doublet surface directly, **3N** must undergo a change in spin state first, which leads in effect to higher barriers to C−H amination by the latter species. Thus, the gain in catalyst robustness in changing from carboxylate to amidate equatorial ligands is counterbalanced by a loss in catalyst efficiency.

(e) Experimental KIE measurements yield values that are too low to be in agreement with a stepwise, C−H abstraction/radical recombination pathway and show better agreement with the mechanism outlined in Scheme 2.5.

2.6 Acknowledgements

We thank the Center for Selective C−H Functionalization supported by the National Science Foundation (CHE-1205646). J.F.B. additionally thanks the DOE (DE-FG02-10ER16204). K.M.L. acknowledges NSF CHE-1454455 for support. The authors gratefully acknowledge NSF MRI-R2 grant (CHE-0958205) and the use of the resources of the Cherry Emerson Center for Scientific Computation. The computational and EPR facilities at UW—Madison are supported by grants from the National Science Foundation (CHE-0840494 and CHE-0741901, respectively). The UCSF Chimera package is developed by the Resource for Biocomputing, Visualization, and Informatics at the University of California, San Francisco (supported by NIGMS P41-GM103311). We acknowledge the UW-Madison Center For High Throughput Computing (CHTC) in the Department of Computer Sciences. The CHTC is supported by UW-Madison, the Advanced Computing Initiative, the Wisconsin Alumni Research Foundation, the Wisconsin Institutes for Discovery, and the National Science Foundation, and is an active member of the Open Science Grid, supported by the National Science Foundation and the U.S. Department of Energy Office of Science.

2.7 Experimental Details

2.7.1 4.1. General Reagents and Methods.

Catalysts **1** and **2** were prepared by published methods.[6, 40] All solvents were used as

received without further purification unless otherwise noted. Electrochemical oxidation of 1 was performed according to a published protocol.[37]

2.7.2 Electron Paramagnetic Resonance.

EPR data were acquired using a Varian Line X-band spectrometer equipped with a Varian E102 microwave bridge interfaced with a Linux system. An Oxford Instruments ESR-900 continuous-flow helium flow cryostat and an Oxford Instruments 3120 temperature controller were used to set and maintain the sample temperature. A Hewlett-Packard 432A power meter was used for microwave power calibration. Simulations were performed using EasySpin software.[76] The hyperfine fittings are based on line shape analysis.

2.7.3 X-ray Absorption Spectroscopy.

Cl K-edge XAS spectra were measured at SSRL beamline 4-3 under ring conditions of 3 GeV and 500 mA. Samples were ground to a fine powder and were spread to a vanishing thickness onto 38 μm low-S Mylar tape. All samples were measured in a He atmosphere at room temperature in fluorescence mode using a Lytle detector. The incident beam energy was calibrated by setting the energy of the first inflection point in the Cl K-edge spectrum of KCl to 2824.8 eV. Intensity was normalized with respect to the incident beam using a He-filled ion chamber upstream of the sample. Data represent an average of six scans measured from 2720 to 3150 eV. Data were processed with SIXPACK. Spectra were normalized by fitting a polynomial flattened to energies below 2840 eV to the data and normalizing the region above this energy to unity.

2.7.4 General Procedure for KIE Experiments.

3-Phenylpropyl-3-D-sulfamate (105 mg, 0.48 mmol, 1.0 equiv) was combined with MgO (45 mg, 1.11 mmol, 2.3 equiv), dirhodium catalyst (12 mmol, 0.025 equiv), and 3.0 mL of CH_2Cl_2. The resulting suspension was stirred for 5 min, after which time $PhI(OAc)_2$ (172 mg, 0.534 mmol,

1.1 equiv) was added in a single portion. The reaction flask was sealed, and the mixture was stirred for 12 h. At the conclusion of this period, the suspension was filtered through a short pad of Celite, and the flask and filter cake were rinsed with 5−10 mL of CH_2Cl_2. The filtrate was concentrated under reduced pressure to a purple oil. Purification of this material by chromatography on silica gel (20% EtOAc in hexanes) afforded the desired product mixture as a white solid. The kinetic isotope effect value was determined by ^{13}C NMR analysis using the method of Wang and Adams.[77]

2.8 Computational Methods.

Calculations of g-tensors, redox potentials, and multiconfigurational electronic structures were performed using the ORCA software package version 3.0.3.[78] Potential energy surface calculations were performed by the Gaussian_09 suite of programs.82 [79] Orbitals were visualized using the MOLEKEL software program[80] or UCSF c himera software program.[81]

2.8.1 Calculation of EPR g-Tensors of 1_L and 2_L.

EPR gtensors of **1_L** and [*trans*-$Rh_2(esp)_2]^+$ were calculated on top of DFToptimized geometry according to the method described above. For **1_Cl_2**, the geometry was obtained from the reported crystal structure of $((NH_2)_3C)_2[Rh_2(OAc)_4Cl_2]$ without further optimization. To calculate the g-tensors for all the complexes studied, the B3LYP functional with scalar relativistically recontracted basis set of TZVP (ZORA-def2-TZVP)[82-83] was used. Scalar relativistic effects were accounted for in the Hamiltonian by the zeroth-order regular approximation (ZORA) using the model potential of van Wullen.[84]

Ab initio multireference configuration interaction (MRCI) calculations of the molecular g-tensors for dirhodium tetra-acetate complexes were performed on top of DFT-optimized geometries, except for $[Rh_2(OAc)_4Cl_2]^-$ (vide infra). The DFT geometries were optimized using

the BP86[85-86] functional with the ZORA-def2-TZVPP basis set on Rh and the ZORA-def2-SVP basis set on the rest of the atoms. Scalar relativistic effects were accounted for by ZORA. The evaluation of the Coulomb integrals were approximated by the resolution of identity (RI) approach.[87] Dispersion effects were treated with the D3[88] correction. The MRCI calculations were performed at the state-averaged complete active space self-consistent field (SA-CASSCF)[89] wave functions. Here, the MRCI approach was modeled by the multireference difference-dedicated configuration interaction theory with two degrees of freedom (MR-DDCI2).[90-91] To calculate the molecular g-tensors, first-order perturbation on the converged MRDDCI2:CASSCF wave function using the electronic Zeeman Hamiltonian was performed. The effect of spin−orbit coupling was introduced using the quasi-degenerate perturbation theory,95,96 with the spin−orbit mean-field Hamiltonian. In the SA-CASSCF calculations, we used different active spaces to incorporate the effects of axial ligands. An active space of 13 electrons in eight orbitals (13,8) was used for the axially free $[Rh_2(OAc)_4]^+$ complex to include all metal d orbitals except the two d_{x2-y2} orbitals which are highly antibonding with respect to the equatorial ligands. An active space of (17,10), which includes all spin−orbitals in (13,8) and four electrons in two σ orbitals from both H_2O ligands, was used for the bis(aquo) complex. An active space of (19,11), which includes all spin−orbitals in (13,8) and six electrons in three orbitals from the 3p orbitals of Cl^-, was used for the chloro complex. An active space of 25 electrons in 14 orbitals (25,14), which includes all spin−orbitals in (13,8) and 12 electrons in six orbitals from the 3p orbitals of both Cl^-, was used for the dichloro complex.

CASSCF calculations on the nitrene complexes, **2N** and **3N**, were performed on truncated models, denoting **2N′** and **3N′**, with the organic substituent on the nitrene replaced by a methyl group. A (19,12) active space was used. This active space includes (13,8) from both rhodium atoms

and (7,4) from the nitrene, which are N 2s orbital and nitrene one σ and two π orbitals. The inclusion of the N 2s orbital helps stabilize the convergence of the CASSCF calculations.

2.8.2 Calculation of the Redox Potentials of 2_L and 3_L.

DFT prediction of redox potentials was performed using a slightly modified procedure following an established method.[56] Geometries were optimized in gas phase followed by single-point energy calculations in CH_2Cl_2. Solvation were modeled by conductor-like screening model (COSMO). The Gibbs free energies of the redox half reaction in CH_2Cl_2 were calculated as follows:

$$\Delta G_{solv}^{abs,redox} = \Delta G_{g}^{abs,redox} + \Delta G_{s}^{\circ}(Red)$$

and the calculated Gibbs free energies were converted to absolute electron redox potential according to the Nernst equation:

$$\Delta G_{solv}^{abs,redox} = -FE_{calc}^{abs}$$

where F is the Faraday constant, 96500 C mol−1. The calculated absolute redox potentials of the half-reaction were converted to standard potentials:

$$E_{calc}^{\circ} = E_{calc}^{abs} + E^{abs}(H_2/H^+)$$

where $E^{abs}(H_2/H^+)$ is a literature value of −4.44 V.[92] The calculated standard potentials were converted to referenced potentials (vs Fc/Fc^+):

$$E_{calc}^{Fc} = E_{calc}^{\circ} + E^{\circ}(Fc/Fc^+)$$

where $E^{\circ}(Fc/Fc^+)$ is 0.46 V.[93]

2.8.3 Calculation of the C−H Amination by 2N_L and 3N_L.

Studies of potential energy surfaces of the C−H amination in **2N_L** and **3N_L** complexes used the M06L density functional[94] in conjunction with the 6-31G** basis sets for C, H, N, O, and S atoms[95] and LANL08(f) basis sets (with their corresponding ECPs) for Rh atoms (referred to

below as basis sets BS1).[96-98] All reported structures were fully optimized without any geometry constraints. Pr eviously, it was reported that this computational method describes the energies and geometries of organometallic compounds well.[61, 63, 65, 67] Frequency calculations were carried out to verify the nature of the located stationary points. Graphical analysis of the imaginary vibrational normal modes as well as the performed IRC calculations confirmed the nature of the located transition states. Energetics of the reported structures were improved by performing single-point energy calculations at the M06L level of theory in conjunction with the 6-311+G(df,p) basis sets for C, H, O, N, and S atoms100 and LANL08(f) for the Rh centers (referred to below as basis sets BS2). In these calculations, we used the M06L/BS1 optimized geometries. The reported thermodynamic data were computed at 298.15 K and 1 atm pressure. Solvent effects in dichloromethane were included by means of the PCM method.[99] In these calculations, the free energy of solvation was computed as

$$\Delta\Delta G_{solv} = G_{solv,PCM} - E_{el}$$

where the final free energy in solution is obtained as

$$G_{solv} = G_{gas} - \Delta\Delta G_{solv}$$

2.9 Supplementary Information

The Supporting Information is available free of charge on the ACS Publications website at DOI: 10.1021/jacs.5b12790.

2.10 References

1. Davies, H. M. L.; Manning, J. R., Catalytic C-H functionalization by metal carbenoid and nitrenoid insertion. *Nature* **2008,** *451* (7177), 417-424.
2. Du Bois, J., Rhodium-catalyzed C-H amination. an enabling method for chemical synthesis. *Org. Process Res. Dev.* **2011,** *15* (4), 758-762.

3. Kornecki, K. P.; Berry, J. F.; Powers, D. C.; Ritter, T., Metal·Metal Bond-Containing Complexes as Catalysts for C·H Functionalization. In *Prog. Inorg. Chem.*, 2014; Vol. 58, pp 225-302.
4. Roizen, J. L.; Harvey, M. E.; Bois, J. D., Metal-catalyzed nitrogen-atom transfer methods for the oxidation of aliphatic C-H bonds. *Acc. Chem. Res.* **2012,** *45* (6), 911-922.
5. Zalatan, D. N.; Du Bois, J., Metal-catalyzed oxidations of C-H to C-N bonds. *Top. Curr. Chem.* **2010,** *292*, 347-378.
6. Espino, C. G.; Fiori, K. W.; Kim, M.; Du Bois, J., Expanding the scope of C-H amination through catalyst design. *J. Am. Chem. Soc.* **2004,** *126* (47), 15378-15379.
7. Beltrán, Á.; Lescot, C.; Mar Díaz-Requejo, M.; Pérez, P. J.; Dauban, P., Catalytic C-H amination of alkanes with sulfonimidamides: Silver(I)-scorpionates vs. dirhodium(II) carboxylates. *Tetrahedron* **2013,** *69* (22), 4488-4492.
8. Cui, Y.; He, C., A silver-catalyzed intramolecular amidation of saturated C-H bonds. *Angew. Chem. Int. Ed.* **2004,** *43* (32), 4210-4212.
9. Li, Z.; Capretto, D. A.; Rahaman, R.; He, C., Silver-catalyzed intermolecular amination of C-H groups. *Angew. Chem. Int. Ed.* **2007,** *46* (27), 5184-5186.
10. Rigoli, J. W.; Weatherly, C. D.; Alderson, J. M.; Vo, B. T.; Schomaker, J. M., Tunable, chemoselective amination via silver catalysis. *J. Am. Chem. Soc.* **2013,** *135* (46), 17238-17241.
11. Scamp, R. J.; Rigoli, J. W.; Schomaker, J. M., Chemoselective silver-catalyzed nitrene insertion reactions. *Pure Appl. Chem.* **2014,** *86* (3), 381-393.
12. Breslow, R.; Gellman, S. H., Intramolecular Nitrene C-H Insertions Mediated by Transition-Metal Complexes as Nitrogen Analogues of Cytochrome P-450 Reactions. *J. Am. Chem. Soc.* **1983,** *105* (22), 6728-6729.
13. Liu, Y.; Che, C. M., [FeIII(F_{20}-tpp)Cl] Is an effective catalyst for nitrene transfer reactions and animation of saturated hydrocarbons with sulfonyl and aryl azides as nitrogen source under thermal and microwave-assisted conditions. *Chem. Eur. J.* **2010,** *16* (34), 10494-10501.
14. Liu, Y.; Guan, X.; Wong, E. L. M.; Liu, P.; Huang, J. S.; Che, C. M., Nonheme iron-mediated amination of C(sp^3)-H bonds. Quinquepyridine-supported iron-imide/nitrene intermediates by experimental studies and DFT calculations. *J. Am. Chem. Soc.* **2013,** *135* (19), 7194-7204.
15. Liu, Y.; Wei, J.; Che, C. M., [Fe(F_{20}-TPP)Cl] catalyzed intramolecular C-N bond formation for alkaloid synthesis using aryl azides as nitrogen source. *Chem. Commun.* **2010,** *46* (37), 6926-6928.
16. Mahy, J. P.; Bedi, G.; Battioni, P.; Mansuy, D., Allylic amination of alkenes by tosyliminoiodobenzene: manganese porphyrins as suitable catalysts. *Tetrahedron Lett.* **1989,** *29* (16), 1927-1930.
17. Paradine, S. M.; White, M. C., Iron-catalyzed intramolecular allylic C-H amination. *J. Am. Chem. Soc.* **2012,** *134* (4), 2036-2039.
18. Wang, H.; Li, Y.; Wang, Z.; Lou, J.; Xiao, Y.; Qiu, G.; Hu, X.; Altenbach, H. J.; Liu, P., Iron-catalyzed efficient intermolecular amination of C(sp^3)-H bonds with bromamine-T as nitrene source. *RSC Adv.* **2014,** *4* (48), 25287-25290.
19. Paradine, S. M.; Griffin, J. R.; Zhao, J.; Petronico, A. L.; Miller, S. M.; Christina White, M., A manganese catalyst for highly reactive yet chemoselective intramolecular C(sp^3)-H amination. *Nat. Chem.* **2015,** *7* (12), 987-994.
20. Yu, X. Q.; Huang, J. S.; Zhou, X. G.; Che, C. M., Amidation of saturated C-H bonds catalyzed by electron-deficient ruthenium and manganese porphyrins. A highly catalytic nitrogen

atom transfer process. *Org. Lett.* **2000,** *2* (15), 2233-2236.
21. Au, S. M.; Huang, J. S.; Yu, W. Y.; Fung, W. H.; Che, C. M., Aziridination of alkenes and amidation of alkanes by bis(tosylimido)ruthenium(VI) porphyrins. A mechanistic study. *J. Am. Chem. Soc.* **1999,** *121* (39), 9120-9132.
22. Liang, J. L.; Yuan, S. X.; Huang, J. S.; Che, C. M., Intramolecular C-N bond formation reactions catalyzed by ruthenium porphyrins: Amidation of sulfamate esters and aziridination of unsaturated sulfonamides. *J. Org. Chem.* **2004,** *69* (11), 3610-3619.
23. Milczek, E.; Boudet, N.; Blakey, S., Enantioselective C-H amination using cationic ruthenium(II)-pybox catalysts. *Angew. Chem. Int. Ed.* **2008,** *47* (36), 6825-6828.
24. Bagchi, V.; Paraskevopoulou, P.; Das, P.; Chi, L.; Wang, Q.; Choudhury, A.; Mathieson, J. S.; Cronin, L.; Pardue, D. B.; Cundari, T. R.; Mitrikas, G.; Sanakis, Y.; Stavropoulos, P., A versatile tripodal Cu(I) reagent for C-N bond construction via nitrene-transfer chemistry: Catalytic perspectives and mechanistic insights on C-H aminations/amidinations and olefin aziridinations. *J. Am. Chem. Soc.* **2014,** *136* (32), 11362-11381.
25. Caballero, A.; Díaz-Requejo, M. M.; Belderraín, T. R.; Nicasio, M. C.; Trofimenko, S.; Pérez, P. J., Highly regioselective functionalization of aliphatic carbon-hydrogen bonds with a perbromohomoscorpionate copper(I) catalyst. *J. Am. Chem. Soc.* **2003,** *125* (6), 1446-1447.
26. Díaz-Requejo, M. M.; Belderraín, T. R.; Nicasio, M. C.; Trofimenko, S.; Pérez, P. J., Cyclohexane and benzene amination by catalytic nitrene insertion into C-H bonds with the copper-homoscorpionate catalyst $TpBr_3Cu(NCMe)$. *J. Am. Chem. Soc.* **2003,** *125* (40), 12078-12079.
27. Fructos, M. R.; Trofimenko, S.; Mar Díaz-Requejo, M.; Pérez, P. J., Facile amine formation by intermolecular catalytic amidation of carbon-hydrogen bonds. *J. Am. Chem. Soc.* **2006,** *128* (36), 11784-11791.
28. Gephart, R. T.; Warren, T. H., Copper-catalyzed sp^3 C-H amination. *Organometallics* **2012,** *31* (22), 7728-7752.
29. Pelletier, G.; Powell, D. A., Copper-catalyzed amidation of allylic and benzylic C-H bonds. *Org. Lett.* **2006,** *8* (26), 6031-6034.
30. Powell, D. A.; Fan, H., Copper-catalyzed amination of primary benzylic C-H bonds with primary and secondary sulfonamides. *J. Org. Chem.* **2010,** *75* (8), 2726-2729.
31. Cui, X.; Xu, X.; Jin, L. M.; Wojtas, L.; Zhang, X. P., Stereoselective radical C-H alkylation with acceptor/acceptor-substituted diazo reagents via Co(II)-based metalloradical catalysis. *Chem. Sci.* **2015,** *6* (2), 1219-1224.
32. Huang, G. H.; Li, J. M.; Huang, J. J.; Lin, J. D.; Chuang, G. J., Cooperative effect of two metals: $CoPd(OAc)_4$-catalyzed C-H amination and aziridination. *Chem. Eur. J.* **2014,** *20* (18), 5240-5243.
33. Lu, H.; Hu, Y.; Jiang, H.; Wojtas, L.; Zhang, X. P., Stereoselective radical amination of electron-deficient C(sp^3)-H bonds by Co(II)-based metalloradical catalysis: Direct synthesis of α-amino acid derivatives via α-C-H amination. *Org. Lett.* **2012,** *14* (19), 5158-5161.
34. Lu, H.; Li, C.; Jiang, H.; Lizardi, C. L.; Zhang, X. P., Chemoselective amination of propargylic C(sp^3)-H bonds by cobalt(II)-based metalloradical catalysis. *Angew. Chem. Int. Ed.* **2014,** *53* (27), 7028-7032.
35. Fiori, K. W.; Du Bois, J., Catalytic intermolecular amination of C-H bonds: Method development and mechanistic insights. *J. Am. Chem. Soc.* **2007,** *129* (3), 562-568.
36. Davies, H. M. L.; Morton, D., Guiding principles for site selective and stereoselective intermolecular C-H functionalization by donor/acceptor rhodium carbenes. *Chem. Soc. Rev.* **2011,** *40* (4), 1857-1869.

37. Kornecki, K. P.; Berry, J. F., Evidence for a one-electron mechanistic regime in dirhodium-catalyzed intermolecular C-H amination. *Chem. Eur. J.* **2011,** *17* (21), 5827-5832.
38. Perry, R. H.; Cahill Iii, T. J.; Roizen, J. L.; Du Bois, J.; Zare, R. N., Capturing fleeting intermediates in a catalytic C-H amination reaction cycle. *Proceedings of the National Academy of Sciences of the United States of America* **2012,** *109* (45), 18295-18299.
39. Zalatan, D. N.; Du Bois, J., Understanding the differential performance of $Rh_2(esp)_2$ as a catalyst for C-H amination. *J. Am. Chem. Soc.* **2009,** *131* (22), 7558-7559.
40. Kornecki, K. P.; Berry, J. F., Introducing a mixed-valent dirhodium(ii,iii) catalyst with increased stability in C-H amination. *Chem. Commun.* **2012,** *48* (99), 12097-12099.
41. Doyle, M. P., Perspective on dirhodium carboxamidates as catalysts. *J. Org. Chem.* **2006,** *71* (25), 9253-9260.
42. Norman, J. G.; Renzoni, G. E.; Case, D. A., Electronic Structure of $Ru_2(O_2CR)_4^+$ and $Rh_2(O_2CR)_4^+$ Complexes. *J. Am. Chem. Soc.* **1979,** *101* (18), 5256-5267.
43. *Multiple Bonds between Metal Atoms*. 3 ed.; Springer-Verlag New York: 2005.
44. Lichtenberger, D. L.; Pollard, J. R.; Lynn, M. A.; Cotton, F. A.; Feng, X., Metal-metal bonding in $Rh_2(O_2CCF_3)_4$: Extensive metal-ligand orbital mixing promoted by filled fluorine orbitals. *J. Am. Chem. Soc.* **2000,** *122* (13), 3182-3190.
45. McNaughton, R. L.; Roemelt, M.; Chin, J. M.; Schrock, R. R.; Neese, F.; Hoffman, B. M., Experimental and theoretical EPR study of jahn-teller-active [HIPTN$_3$N]MoL complexes (L = N_2, CO, NH_3). *J. Am. Chem. Soc.* **2010,** *132* (25), 8645-8656.
46. Kawamura, T.; Fukamachi, K.; Sowa, T.; Hayashida, S.; Yonezawa, T., Electronic Structure of the Rh-Rh Bond in $Rh_2(O_2CR)_4(PY_3)_2$ by Electron Spin Resonance Study of Their Cation Radicals. *J. Am. Chem. Soc.* **1981,** *103* (2), 364-369.
47. Kawamura, T.; Katayama, H.; Nishikawa, H.; Yamabe, T., Ligand Dependence of Electronic Configuration of the Rh-Rh Bond in Rh_2^{5+} Complexes As Studied by Electron Spin Resonance and Electrochemistry. *J. Am. Chem. Soc.* **1989,** *111* (21), 8156-8160.
48. Kawamura, T.; Katayama, H.; Yamabe, T., An electron-spin resonance study of $Rh_2(O_2CCH_3)_4(H_2O)_2^+$: evidence of π_{RhRh}ODD electron orbital. *Chem. Phys. Lett.* **1986,** *130* (1-2), 20-23.
49. Kawamura, T.; Maeda, M.; Miyamoto, M.; Usami, H.; Imaeda, K.; Ebihara, M., Geometrical difference and electron configuration of lantern-type $Rh_2^{4+}$and Rh_2^{5+} complexes: X-ray structural and DFT study. *J. Am. Chem. Soc.* **1998,** *120* (32), 8136-8142.
50. Chavan, M. Y.; Lin, X. Q.; Ahsan, M. Q.; Bear, J. L.; Kadish, K. M.; Zhu, T. P., Axial-ligand-dependent electrochemical and spectral properties of a series of acetate and acetamidate-bridged dirhodium complexes. *Inorg. Chem.* **1984,** *23* (26), 4538-4545.
51. Schäfer, A.; Horn, H.; Ahlrichs, R., Fully optimized contracted Gaussian basis sets for atoms Li to Kr. *J. Chem. Phys.* **1992,** *97* (4), 2571-2577.
52. Becke, A. D., A new mixing of Hartree-Fock and local density-functional theories. *J. Chem. Phys.* **1993,** *98* (2), 1372-1377.
53. Lee, C.; Yang, W.; Parr, R. G., Development of the Colle-Salvetti correlation-energy formula into a functional of the electron density. *Phys. Rev. B* **1988,** *37* (2), 785-789.
54. Stephens, P. J.; Devlin, F. J.; Chabalowski, C. F.; Frisch, M. J., Ab Initio calculation of vibrational absorption and circular dichroism spectra using density functional force fields. *J. Phys. Chem.* **1994,** *98* (45), 11623-11627.
55. Vosko, S. H.; Wilk, L.; Nusair, M., *Can. J. Phys.* **1980,** *58*, 1200-1211.
56. Roy, L. E.; Jakubikova, E.; Graham Guthrie, M.; Batista, E. R., Calculation of one-electron

redox potentials revisited. Is it possible to calculate accurate potentials with density functional methods? *J. Phys. Chem. A* **2009,** *113* (24), 6745-6750.
57. Bersuker, I. B., Limitations of density functional theory in application to degenerate states. *J. Comput. Chem.* **1997,** *18* (2), 260-267.
58. Warzecha, E.; Berto, T. C.; Berry, J. F., Axial Ligand Coordination to the C-H Amination Catalyst $Rh_2(esp)_2$: A Structural and Spectroscopic Study. *Inorg. Chem.* **2015,** *54* (17), 8817-8824.
59. Berry, J. F., Terminal nitrido and imido complexes of the late transition metals. *Comments Inorg. Chem.* **2009,** *30* (1-2), 28-66.
60. Berry, J. F., The role of three-center/four-electron bonds in superelectrophilic dirhodium carbene and nitrene catalytic intermediates. *Dalton Trans.* **2012,** *41* (3), 700-713.
61. Harvey, M. E.; Musaev, D. G.; Du Bois, J., A diruthenium catalyst for selective, intramolecular allylic C-H amination: Reaction development and mechanistic insight gained through experiment and theory. *J. Am. Chem. Soc.* **2011,** *133* (43), 17207-17216.
62. Kornecki, K. P.; Briones, J. F.; Boyarskikh, V.; Fullilove, F.; Autschbach, J.; Schrote, K. E.; Lancaster, K. M.; Davies, H. M. L.; Berry, J. F., Direct spectroscopic characterization of a transitory dirhodium donor-acceptor carbene complex. *Science* **2013,** *342* (6156), 351-354.
63. Li, Z.; Boyarskikh, V.; Hansen, J. H.; Autschbach, J.; Musaev, D. G.; Davies, H. M. L., Scope and mechanistic analysis of the enantioselective synthesis of allenes by rhodium-catalyzed tandem ylide formation/[2,3]-sigmatropic rearrangement between donor/acceptor carbenoids and propargylic alcohols. *J. Am. Chem. Soc.* **2012,** *134* (37), 15497-15504.
64. Pap, J. S.; George, S. D.; Berry, J. F., Delocalized metal-metal and metal-ligand multiple bonding in a linear Ru-Ru≡N unit: Elongation of a traditionally short Ru≡N bond. *Angew. Chem. Int. Ed.* **2008,** *47* (52), 10102-10105.
65. Qin, C.; Boyarskikh, V.; Hansen, J. H.; Hardcastle, K. I.; Musaev, D. G.; Davies, H. M. L., D_2-symmetric dirhodium catalyst derived from a 1,2,2-triarylcyclopropanecarboxylate ligand: Design, synthesis and application. *J. Am. Chem. Soc.* **2011,** *133* (47), 19198-19204.
66. Sperger, T.; Sanhueza, I. A.; Kalvet, I.; Schoenebeck, F., Computational Studies of Synthetically Relevant Homogeneous Organometallic Catalysis Involving Ni, Pd, Ir, and Rh: An Overview of Commonly Employed DFT Methods and Mechanistic Insights. *Chem. Rev.* **2015,** *115* (17), 9532-9586.
67. Wang, H.; Guptill, D. M.; Varela-Alvarez, A.; Musaev, D. G.; Davies, H. M. L., Rhodium-catalyzed enantioselective cyclopropanation of electron-deficient alkenes. *Chem. Sci.* **2013,** *4* (7), 2844-2850.
68. Brown, T. R.; Dolinar, B. S.; Hillard, E. A.; Clérac, R.; Berry, J. F., Electronic Structure of Ru_2(II,II) Oxypyridinates: Synthetic, Structural, and Theoretical Insights into Axial Ligand Binding. *Inorg. Chem.* **2015,** *54* (17), 8571-8589.
69. Goswami, M.; Lyaskovskyy, V.; Domingos, S. R.; Buma, W. J.; Woutersen, S.; Troeppner, O.; Ivanović-Burmazović, I.; Lu, H.; Cui, X.; Zhang, X. P.; Reijerse, E. J.; Debeer, S.; Van Schooneveld, M. M.; Pfaff, F. F.; Ray, K.; De Bruin, B., Characterization of porphyrin-Co(III)-'nitrene radical' species relevant in catalytic nitrene transfer reactions. *J. Am. Chem. Soc.* **2015,** *137* (16), 5468-5479.
70. Truxillo, L. A.; Davis, D. G., Electrochemistry of Cobalt Tetraphenylporphyrin in Aprotic Media. *Anal. Chem.* **1975,** *47* (13), 2260-2267.
71. Lyaskovskyy, V.; Suarez, A. I. O.; Lu, H.; Jiang, H.; Zhang, X. P.; De Bruin, B., Mechanism of cobalt(II) porphyrin-catalyzed C-H amination with organic azides: Radical nature and H-atom abstraction ability of the key cobalt(III)-nitrene intermediates. *J. Am. Chem. Soc.*

2011, *133* (31), 12264-12273.
72. Saouma, C. T.; Mayer, J. M., Do spin state and spin density affect hydrogen atom transfer reactivity? *Chem. Sci.* **2014,** *5* (1), 21-31.
73. Harvey, J. N.; Poli, R.; Smith, K. M., Understanding the reactivity of transition metal complexes involving multiple spin states. *Coord. Chem. Rev.* **2003,** *238-239*, 347-361.
74. Schröder, D.; Shaik, S.; Schwarz, H., Two-state reactivity as a new concept in organometallic chemistry. *Acc. Chem. Res.* **2000,** *33* (3), 139-145.
75. Collet, F.; Lescot, C.; Liang, C.; Dauban, P., Studies in catalytic C-H amination involving nitrene C-H insertion. *Dalton Trans.* **2010,** *39* (43), 10401-10413.
76. Stoll, S.; Schweiger, A., EasySpin, a comprehensive software package for spectral simulation and analysis in EPR. *J. Magn. Res.* **2006,** *178* (1), 42-55.
77. Wang, P.; Adams, J., Model Studies of the Stereoelectronic Effect in Rh(II) Mediated Carbenoid C-H Insertion Reactions. *J. Am. Chem. Soc.* **1994,** *116* (8), 3296-3305.
78. Neese, F., The ORCA program system. *Wiley Interdiscip. Rev. Comput. Mol. Sci.* **2012,** *2* (1), 73-78.
79. Frisch, M. J. T., G. W.; Schlegel, H. B.; Scuseria, G. E.;; Robb, M. A. C., J. R.; Scalmani, G.; Barone, V.; Mennucci,; B.; Petersson, G. A. N., H.; Caricato, M.; Li, X.; Hratchian, H.; P.; Izmaylov, A. F. B., J.; Zheng, G.; Sonnenberg, J. L.; Hada, M.;; Ehara, M. T., K.; Fukuda, R.; Hasegawa, J.; Ishida, M.; Nakajima,; T.; Honda, Y. K., O.; Nakai, H.; Vreven, T.; Montgomery, J. A., Jr.;; Peralta, J. E. O., F.; Bearpark, M.; Heyd, J. J.; Brothers, E.; Kudin,; K. N.; Staroverov, V. N. K., R.; Normand, J.; Raghavachari, K.;; Rendell, A. B., J. C.; Iyengar, S. S.; Tomasi, J.; Cossi, M.; Rega,; N.; Millam, J. M. K., M.; Knox, J. E.; Cross, J. B.; Bakken, V.;; Adamo, C. J., J.; Gomperts, R.; Stratmann, R. E.; Yazyev, O.;; Austin, A. J. C., R.; Pomelli, C.; Ochterski, J. W.; Martin, R. L.;; Morokuma, K. Z., V. G.; Voth, G. A.; Salvador, P.;; Dannenberg, J. J. D., S.; Daniels, A. D.; Farkas, Ö.;; Foresman, J. B. O., J. V.; Cioslowski, J.; Fox, D. J., Gaussian 09, revision D01. In *Gaussian 09*, Gaussian, I. W., CT, Ed. 2009.
80. Flükiger, P.; Lüthi, H. P.; Portmann, S.; Weber, J., *MOLEKEL 4.3*. Swiss Center for Scientific Computing: Manno, Switzerland: 2000.
81. Pettersen, E. F.; Goddard, T. D.; Huang, C. C.; Couch, G. S.; Greenblatt, D. M.; Meng, E. C.; Ferrin, T. E., UCSF Chimera - A visualization system for exploratory research and analysis. *J. Comput. Chem.* **2004,** *25* (13), 1605-1612.
82. Pantazis, D. A.; Chen, X. Y.; Landis, C. R.; Neese, F., All-electron scalar relativistic basis sets for third-row transition metal atoms. *J. Chem. Theory Comput.* **2008,** *4* (6), 908-919.
83. Weigend, F.; Ahlrichs, R., Balanced basis sets of split valence, triple zeta valence and quadruple zeta valence quality for H to Rn: Design and assessment of accuracy. *Phys. Chem. Chem. Phys.* **2005,** *7* (18), 3297-3305.
84. Van Wüllen, C., Molecular density functional calculations in the regular relativistic approximation: Method, application to coinage metal diatomics, hydrides, fluorides and chlorides, and comparison with first-order relativistic calculations. *J. Chem. Phys.* **1998,** *109* (2), 392-399.
85. Becke, A. D., Density-functional exchange-energy approximation with correct asymptotic behavior. *Phys. Rev. A* **1988,** *38* (6), 3098-3100.
86. Perdew, J. P., Density-functional approximation for the correlation energy of the inhomogeneous electron gas. *Phys. Rev. B* **1986,** *33* (12), 8822-8824.
87. Weigend, F., Accurate Coulomb-fitting basis sets for H to Rn. *Phys. Chem. Chem. Phys.* **2006,** *8* (9), 1057-1065.
88. Grimme, S.; Antony, J.; Ehrlich, S.; Krieg, H., A consistent and accurate ab initio

parametrization of density functional dispersion correction (DFT-D) for the 94 elements H-Pu. *J. Chem. Phys.* **2010,** *132* (15).
89. Roos, B. O.; Taylor, P. R.; Sigbahn, P. E. M., A complete active space SCF method (CASSCF) using a density matrix formulated super-CI approach. *Chem. Phys.* **1980,** *48* (2), 157-173.
90. Miralles, J.; Castell, O.; Caballol, R.; Malrieu, J. P., Specific CI calculation of energy differences: Transition energies and bond energies. *Chem. Phys.* **1993,** *172* (1), 33-43.
91. Miralles, J.; Daudey, J. P.; Caballol, R., Variational calculation of small energy differences. The singlet-triplet gap in $[Cu_2Cl_6]_2$. *Chem. Phys. Lett.* **1992,** *198* (6), 555-562.
92. Trasa'tti, S., The absolute electrode potential: An explanatory note *Pure Appl. Chem.* **1986,** *58* (7), 955-966.
93. Connelly, N. G.; Geiger, W. E., Chemical redox agents for organometallic chemistry. *Chem. Rev.* **1996,** *96* (2), 877-910.
94. Zhao, Y.; Truhlar, D. G., A new local density functional for main-group thermochemistry, transition metal bonding, thermochemical kinetics, and noncovalent interactions. *J. Chem. Phys.* **2006,** *125* (19).
95. Hehre, W. J.; Radom, L.; Schleyer, P. V. R.; Pople, J. A., *Ab Initio Molecular Orbital Theory*. John Wiley & Sons: New York: 1986.
96. Ehlers, A. W.; Böhme, M.; Dapprich, S.; Gobbi, A.; Höllwarth, A.; Jonas, V.; Köhler, K. F.; Stegmann, R.; Veldkamp, A.; Frenking, G., A set of f-polarization functions for pseudo-potential basis sets of the transition metals ScCu, YAg and LaAu. *Chem. Phys. Lett.* **1993,** *208* (1-2), 111-114.
97. Hay, P. J.; Wadt, W. R., Ab initio effective core potentials for molecular calculations. Potentials for K to Au including the outermost core orbitale. *J. Chem. Phys.* **1985,** *82* (1), 299-310.
98. Roy, L. E.; Hay, P. J.; Martin, R. L., Revised basis sets for the LANL effective core potentials. *J. Chem. Theory Comput.* **2008,** *4* (7), 1029-1031.
99. Tomasi, J.; Mennucci, B.; Cammi, R., Quantum mechanical continuum solvation models. *Chem. Rev.* **2005,** *105* (8), 2999-3093.

3 Catalyst-Controlled and Tunable, Chemoselective Silver-Catalyzed Intermolecular Nitrene Transfer: Experimental and Computational Studies

This chapter has been published:

Dolan, N. S.;† Scamp, R. J.;† Yang, T.;† Berry, J. F.;* Schomaker, J. M.*

Department of Chemistry, University of Wisconsin—Madison, Madison, Wisconsin 53706, USA

†These authors contributed equally to this manuscript.

3.1 My contribution to this work

This is a collaborative work between the computational studies from the Berry and experimental studies from the Schomaker group. This work describes silver-catalyzed ligand-tunable chemoselective intermolecular nitrene transfer. Radical inhibition studies on the ligand-tunable nitrene transfer showed that the differential chemoselectivity was accompanied by different resistance to the addition of TEMPO radical. In addition, bond rearrangements were observed corroborating the susceptibility to radical inhibition.

My contribution to this work was the computational understanding of the experimental ligand-tunable chemoselectivity, susceptibility to radical inhibition, and bond rearrangements. The understanding of the driving force behind the differential chemoselectivity could provide future insights into other potential ligands for the targeted chemoselectivity.

3.2 Abstract

The development of new catalysts for selective nitrene transfer is a continuing area of interest. In particular, the ability to control the chemoselectivity of intermolecular reactions in the presence of multiple reactive sites has been a long-standing challenge in the field. In this paper, we demonstrate examples of silver-catalyzed, non-directed, intermolecular nitrene transfer reactions that are both chemoselective and flexible for aziridination or C–H insertion, depending on the choice of ligand. Experimental probes present a puzzling picture of the mechanistic details of the pathways mediated by $[(^{t}Bu_3tpy)AgOTf]_2$ and (tpa)AgOTf. Computational studies elucidate these subtleties and provide guidance for the future development of new catalysts exhibiting improved tunability in group transfer reactions.

3.3 Introduction

Amines are important functional groups occurring in a diverse array of molecules with significant biological and therapeutic value. One effective strategy for streamlining the synthesis of amines involves the selective introduction of a new C—N bond at a specific site in a hydrocarbon precursor. Diverse transition metals[1-42] are known to catalyze the insertion of metal nitrenes into either a C–H or C=C bond to yield amines or aziridines, respectively. Substrate control has traditionally been the primary factor dictating the chemoselectivity of the amination event; for example, intramolecular aminations of homoallylic sulfamates tend to yield the aziridination product using popular dinuclear Rh(II) tetracarboxylate catalysts.[5, 10, 13-14, 16, 23-24, 27, 36, 40-41] One notable exception is the dinuclear, chiral carboxamidate complex Rh_2(S-nap)$_4$, which can favor intramolecular C-H bond insertion over aziridination.[40] More recently, it has been shown that the chemoselectivity of nitrene transfer can be altered to favor C–H insertion by changing the metal identity to Ru, Co, Mn or Fe, which results in a change from a concerted to a step-wise nitrene transfer event.[20, 29-30, 34-35, 37]

Achieving catalyst control over the chemoselectivity of intermolecular nitrene transfer using a single metal is even more challenging, particularly when compared to metal-catalyzed carbene transfer reactions.[43-47] A rare example of a Rh-based system selective for intermolecular nitrene insertion into allylic C–H bonds employs Rh_2((S)-nta)$_4$ (nta = (S)-N-1,8-naphthoylalanine) in the presence of chiral sulfonimidamides;[24, 48] however, this behavior relies on a strong match between the chiral Rh catalyst and the optically pure nitrene precursor. In general, most dinuclear Rh catalysts that are successful for intramolecular nitrene transfer perform poorly in intermolecular reactions.[49-52] Two major factors impeding the development of more modular and less expensive catalysts for nitrene transfer include a poor understanding of how reactivity differs in intra- vs. intermolecular processes, as well as how the mechanism and selectivity of the nitrene transfer

responds to modifications to the supporting ligands for a particular metal. A better understanding of these issues is necessary to spur further progress towards our ultimate goal of developing new, inexpensive catalysts for predictable, tunable and intermolecular site-selective nitrene transfer reactions, a long-standing goal in the field.

We have demonstrated that silver(I) catalysis offers unique opportunities to tune the chemo- and site-selectivity of intramolecular nitrene transfer (Scheme 3.1A-B).[53-55] Changes to the ligand, the AgOTf:ligand ratio, and the nitrene precursor all influence the coordination geometry and reactivity of the putative nitrene. For example, preference for aziridination or C–H bond insertion in a homoallylic carbamate can be controlled by simply changing the ratio of 1,10-phenanthroline (phen) to AgOTf (Scheme 3.1A).[54] Enforcing different coordination geometries at Ag(I) using diverse ligands, including 4,4'-di-tert-butyl-2,2'-bipyridine (^{t}Bubpy) and tris(2-pyridyl-methyl)amine (tpa), enables site-selective amination of chemically distinct C—H bonds (Scheme 3.1B).[53, 55] Expanding Ag(I) catalysis to tunable, intermolecular nitrene transfer reactions has been challenging; in this work, we describe initial experimental and computational studies to better understand these reactions (Scheme 3.1C).

Scheme 3.1. Ag-catalyzed chemo- and site-selective aminations

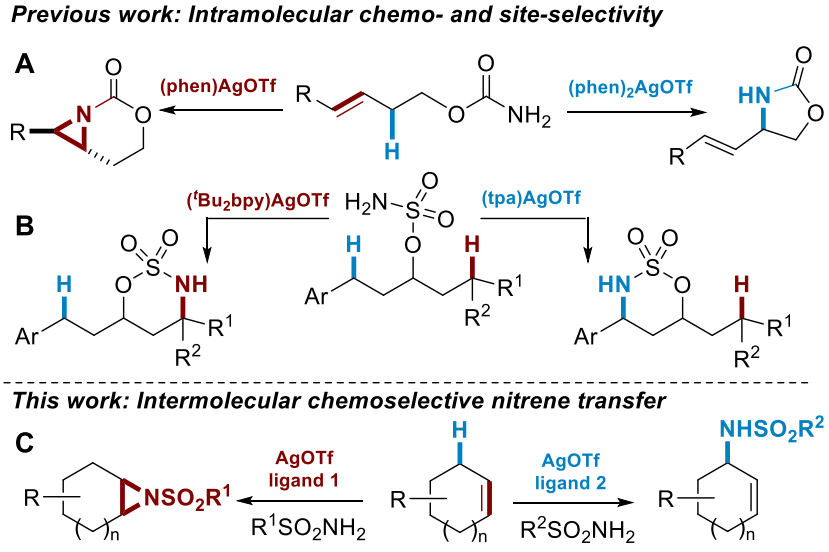

3.4 Results and Discussion

3.4.1 Experimental studies

Initial experimental studies. The reaction of cyclohexene (**1**), 2,2',2"-trichloroethylsulfamate ($TcesNH_2$, **2**) and iodosobenzene (PhIO) with Ag catalysts supported by a variety of readily available N-donor ligands (see the Supporting Information for further details) were carried out (Table 3.1). We found that AgOTf ligated by tert-butylterpyridine **4** (entry 1) gave good selectivity for production of the aziridine **3a** over the allylic amine **3b**.[7-8, 26] X-ray crystallographic and DOSY NMR studies showed that the silver catalyst supported by **4** exists in both the solid and solution states as the dimer $[(^tBu_3tpy)AgOTf]_2$ (hereafter called catalyst **A**), consisting of two three-coordinate Ag centers.[7, 54] Interestingly, employing the tpa ligand **5** (entry 2) resulted in a preference for allylic C–H amination to **3b** over aziridination. A crystal structure of a silver(I) complex bearing a ligand similar to **5** has been reported, suggesting the formula (tpa)Ag(OTf) for catalyst **B**.[56]

Table 3.1. Impact of the ligand on silver-catalyzed nitrene transfer

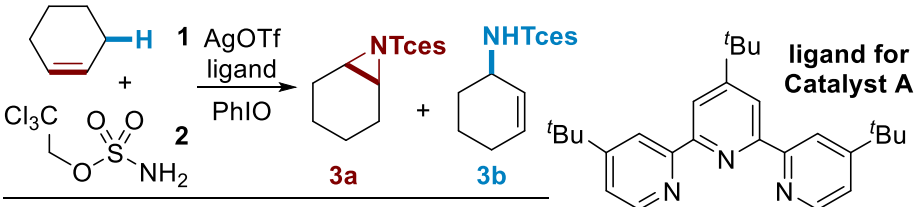

entry[a]	L	PhIO (eq)	h	yield	3a : 3b
1	4	3.5	4	89%	6.4 : 1
2	5	1.2	1	60%	1 : 3.3

[a]NMR yield; Cl_3CCH_2Cl internal standard. Conditions: 5 equiv **1**, 1 equiv **2**, 10 mol% AgOTf, 12 mol% ligand, PhIO, 4 Å MS, CH_2Cl_2.

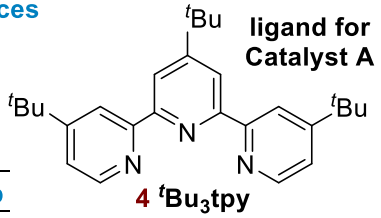

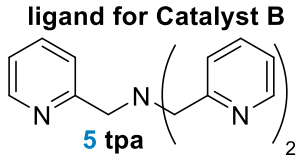

Having demonstrated the ability to control the chemoselectivity of Ag-catalyzed amination by changing the nature of the ligand, the identity of the nitrene precursor was varied in an attempt

to further improve selectivity (Table 3.2). While the **3a:3b** selectivity for aziridination catalyzed by **A** was not improved with alkylsulfamate **2c** as compared to **2a**, the yield did increase to 97%. Other nitrene precursors resulted in either lower yields or decreased selectivity for the aziridine **3a**. When **B** was employed, the C–H amination product was favored to a greater extent employing arylsulfamates **2e-2g**, with **2f** displaying the highest **3b:3a** ratio of 5.8:1. It is worth noting that in the majority of examples, the overall preference of **A** for aziridination and that of **B** for C–H amination is independent of the identity of the nitrene precursor, supporting catalyst-control of nitrene transfer. The one exception is the chiral sulfonimidamide **2d** employed by Dauban in Rh-catalyzed nitrene transfer; in this case, aziridination was preferred using both **A** and **B**.[24, 48]

Table 3.2. Influence of the nitrene precursor on chemoselectivity

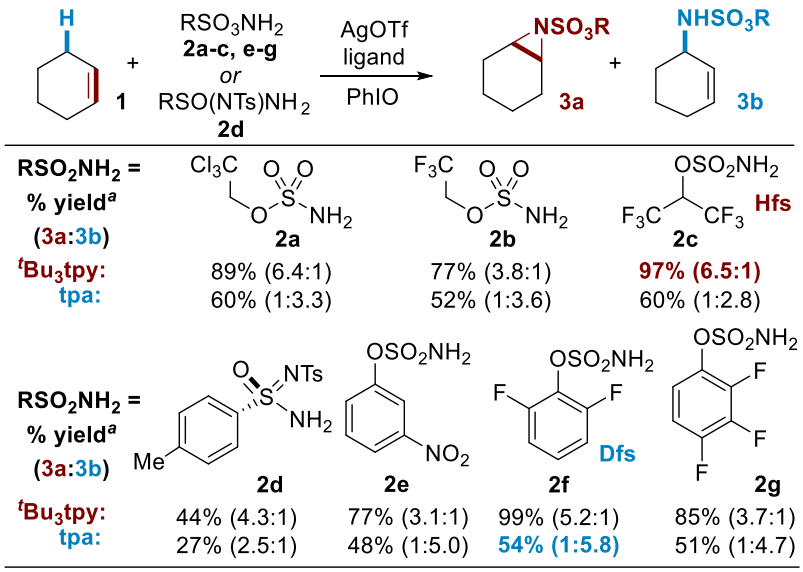

[a]Total NMR yield; Cl_3CCHCl_2 as the internal standard. Conditions: 5 equiv **1**, 1 equiv **2**, 10 mol% AgOTf, 12 mol% ligand, 4 Å MS, CH_2Cl_2, rt. $^tBu_3tpy$ **Catalyst A**: 3.5 equiv PhIO, 4 h. tpa **Catalyst B**: 1.2 equiv PhIO, 30 min.

The scope of tunable nitrene transfer was briefly explored with selected substrates containing both C=C and C–H functionalities (Table 3.3). Five- and six-membered rings (entries 1-4) give chemodivergent amination. However, as the size of the ring increases (entries 5-6), chemoselectivity for the aziridine product also increases with both catalysts **A** and **B**. The lesser

selectivity for C–H amination with **B** in this case may be attributed to poor stabilization of an allylic radical via conjugation with the double bond in the 7-membered ring due to competing transannular interactions, providing indirect evidence that **B** may operate via a step-wise nitrene-transfer pathway. Reaction of trans-hex-2-ene **8** (entries 7-8) gave no isomerization in either aziridination or C–H amination reactions but did show a rearranged product using **B** (entry 8), also indicative of a potential stepwise pathway. **A** is not overly sensitive to steric effects, giving excellent selectivity for aziridination of both tri- and tetrasubstituted alkenes **9** and **10** (entries 9, 11). However, achieving selectivity for C–H insertion in acyclic substrates employing **B** is challenging, as aziridination becomes competitive (entries 10, 12). In order to rationalize these observations and achieve a better understanding of the reasons for the lack of chemocontrol, extensive computational studies were carried out as described later in this report.

Table 3.3. Tunable, catalyst-controlled amination

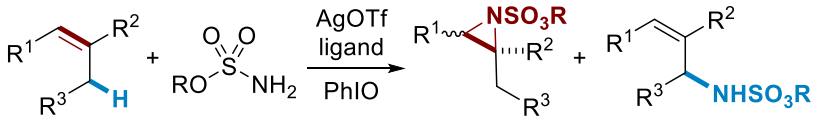

3, 6-10 3a,b 6-10a,b 3c,d 6-10c,d

substrate		entry	ligand	A[a]	I[a]	A : I
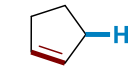	**6**	1	^{t}Bu$_3$tpy	61% **6a**	11% **6c**	**5.5** : 1
		2	tpa	13% **6b**	35% **6d**	1 : **2.7**
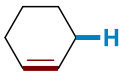	**3**	3	^{t}Bu$_3$tpy	84% **3a**	13% **3c**	**6.5** : 1
		4	tpa	8% **3b**	46% **3d**	1 : **5.8**
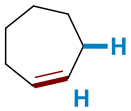	**7**	5	^{t}Bu$_3$tpy	59% **7a**	2% **7c**	**30** : 1
		6	tpa	20% **7b**	24% **7d**	1 : **1.2**
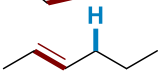	**8**	7	^{t}Bu$_3$tpy	58%[b] **8a**	4%[b] **8c**	**15** : 1
		8	tpa	8% **8b**	25%[c] **8d**	1: **3.1**
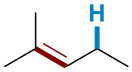	**9**	9	^{t}Bu$_3$tpy	72%[b] **9a**	2%[b] **9c**	**36** : 1
		10	tpa	29% **9b**	25%[d] **9d**	**1.2** : 1
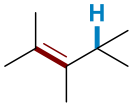	**10**	11	^{t}Bu$_3$tpy	97% **10a**	0% **10c**	**>19** : 1
		12	tpa	25% **10b**	0% **10d**	**>19** : 1

A: HfsNH$_2$ (0.25 mmol), 10 mol% AgOTf, 12 mol% ^{t}Bu$_3$tpy, 3.5 equiv PhIO, CH_2Cl_2, 4 A MS, 4 h, rt. **I**: DfsNH$_2$ (0.25 mmol), 10 mol% AgOTf, 12 mol% tpa, 1.2 equiv PhIO, CH_2Cl_2, 4 A MS, 1 h, rt. [a]Isolated yield. [b]NMR yield, Cl_3CCH_2Cl internal standard. [c]*trans* only, 6% rearranged. [d]3% rearranged.

A series of substituted cyclohexenes of varying complexity were investigated further in tunable silver-catalyzed amination (Table 3.4). Addition of a Me group to the alkene of **11** increases selectivity for aziridination with **A** (entry 1), and improves the preference for C–H amination with **B**; amination of the less hindered allylic C–H_a bond is favored over C–H_b by a ratio of 3.0:1 (entry 2). Aryl-substituted alkenes **12** and **14** (entries 3 and 7) resulted in good selectivity using **A**, but competing epoxidation occurs with electron-rich **13** (entry 5). Excellent selectivity for C–H amination is observed for **12-14** using **B** (entries 4, 6, 8). Catalyst **B** shows sensitivity to steric effects, as amination of the less congested H_a in **12-14** is preferred over the more hindered H_b by a ratio of approximately 6:1 in all three cases. Conjugation of an alkyne with the cyclohexene of **15** gives good chemoselectivity with both catalysts (entries 9-10); however, the aziridine is not stable to chromatography, undergoing rearrangement and hydrolysis to aldehyde **15a**.[57-58] Good site-selectivity for the amination of H_a over H_b was also noted using **15** (entry 10). Moving the Me group from the vinyl carbon of **11** to the allylic position in **16** (entries 11-12) decreases selectivity for aziridination with **A**. In contrast, the selectivity of C–H amination was improved with **B**; however, allylic transposition occurs to give **11d** and **16d**. The addition of an allylic Ph group in **17** further decreases selectivity in aziridination (entry 13), but showed increased preference for insertion to **12d** (entry 14). These experiments provide insights into the mechanistic details of the Ag-catalyzed intermolecular nitrene transfer that will be further discussed in the context of our computational studies (vide infra).

Table 3.4. Tunable amination of C=C and C–H bonds

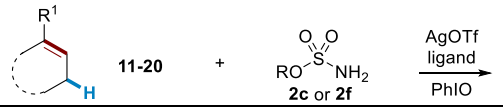

substrate	entry	ligand	A[a]	I (H_a + H_b)[a]	A : I
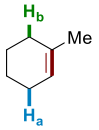 **11**	1	^{t}Bu$_3$tpy	73% **11a**	7% **11c**	**10** : 1
	2	tpa	7% **11b**	61% **11d** 3.0:1 H_a:H_b	1 : **8.7**
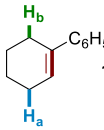 **12**	3	^{t}Bu$_3$tpy	73%[b] **12a**	16% **12c** 3.4:1 H_a:H_b	**4.6** : 1
	4	tpa	20% **12b**	60% **12d** 5.6:1 H_a:H_b	1 : **3.2**
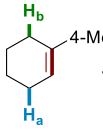 **13**	5	^{t}Bu$_3$tpy	0%[c] **13a**	0% **13c**	----
	6	tpa	2% **13b**	65% **13d** 6.4:1 H_a:H_b	1 : **33**
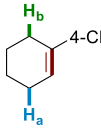 **14**	7	^{t}Bu$_3$tpy	57%[b] **14a**	6% **14c** 5.0:1 H_a:H_b	**9.5** : 1
	8	tpa	3% **14b**	51% **14d** 5.9:1 H_a:H_b	1 : **17**
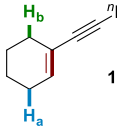 **15**	9	^{t}Bu$_3$tpy	51% **15a**[d]	17% **15c** 9.0:1 H_a:H_b	**3.0** : 1
	10	tpa	8% **15b**	62% **15d** 11:1 H_a:H_b	1 : **7.8**

substrate	entry	ligand	A[a]	I (H_a + H_b)[a]	A : I
 **16**	11	^{t}Bu$_3$tpy	40% **16a** 1:4.8 *syn:anti*	16%[e] **11c**	**2.5** :1
	12	tpa	3% **16b**	39%[e] **11d**	1 : **13**
 **17**	13	^{t}Bu$_3$tpy	22% **17a** 1:19 *syn:anti*	20%[e] **12c**	**1.1** : 1
	14	tpa	2% **17b**	32%[e] **12d**	1 : **16**
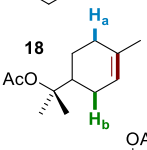 **18**	15	^{t}Bu$_3$tpy	65% **17a** 1:11 *syn:anti*	10% **18c**	**6.5** :1
	16	tpa	12% **18b**	49% **18d** 4.4:1 H_a:H_b	1 : **4.1**
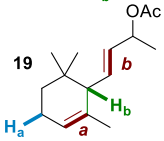 **19**	17	^{t}Bu$_3$tpy	55% **19a** (*dr* 2.4:1) (***a*:*b*** >20:1)	19% **19c** (*dr* 3.9:1)	**2.9** : 1
	18	tpa	3% **19b**	46% **19d** H_a (2.2:1 *anti:syn*)	1 : **15.3**
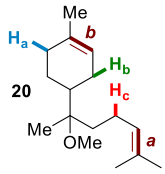 **20**	19	^{t}Bu$_3$tpy	72% **20a** (***a*:*b*** 2.4:1)	0% **20c**	**>19** : 1
	20	tpa	29% **20b** (***a*:*b*** 6.3:1)	18% **20d** >19:1 H_a:H_b	**1.6** : 1

A: 10 mol% AgOTf, 12 mol% ^{t}Bu$_3$tpy, **2c**, 3.5 equiv PhIO, CH_2Cl_2, 4 A MS, 4 h, rt. **I**: 10 mol% AgOTf, 12 mol% tpa, **2f**, 1.2 equiv PhIO, CH_2Cl_2, 4 A MS, 1 h, rt. [a] Isolated yields. [b] Aziridine was opened with MeOH. [c] Formation of the epoxide as the major product. [d] 56% NMR yield of aziridine, isolated as the aldehyde in 51% yield. [e] Transposition of the allylic bond was noted to give the trisubstituted alkene as the product. The ratio of expected to allylic product was approximately 1:1 while transposition was highly dominant for **17**.

A series of natural product-derived substrates **18**-**20**, containing multiple alkene and allylic C–H functionalities, were explored. Alkene **18** gives good selectivity for aziridination and a high 11:1 anti:syn ratio (entry 15). The sensitivity of **B** to steric effects is illustrated in entry 16, where activation of H_a is now preferred over H_b by a ratio of 4.4:1 (compare to entry 2). The α-ionone derivative **19** shows poorer selectivity for aziridination (entry 17), perhaps due to the increased steric demand of the more electron-rich alkene **a**. Both chemo- and site-selectivity for C–H insertion (entry 18) are excellent. Finally, only aziridination of bisabolyl methyl ether **20** is observed with **A** (entry 19), with the exocyclic alkene preferred over the endocyclic alkene by a ratio of 2.4:1. The presence of two electron-rich alkenes in **20** results in poor selectivity for C–H amination (entry 20); however, site-selectivity for the less hindered H_a is excellent, favoring H_a over H_b by a ratio of > 19:1.

Scheme 3.2. Influence of TEMPO on the amination of **11** and **16**

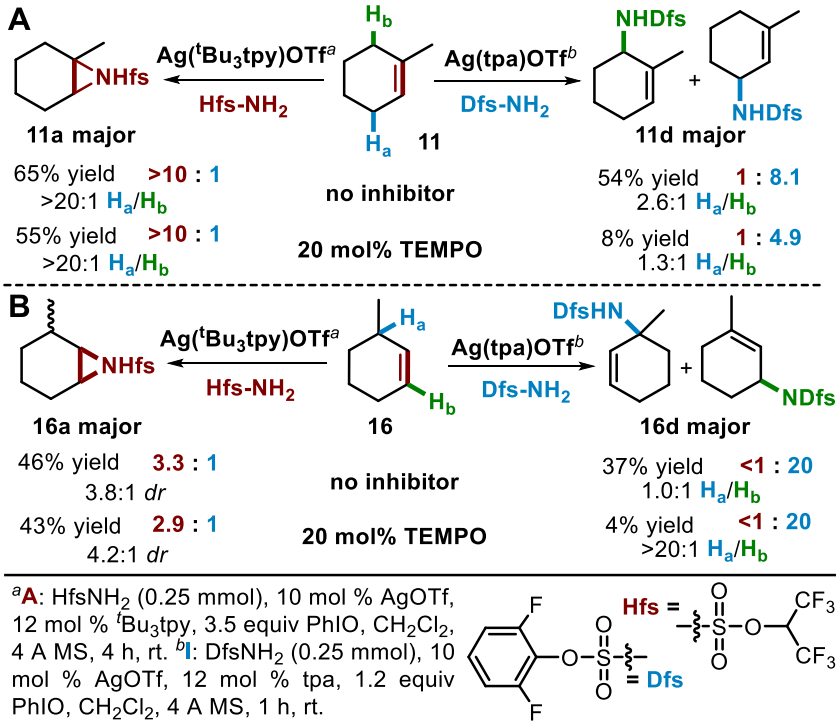

Mechanistic studies. Further experimental studies were carried out to better understand the mechanistic details of amination pathways promoted by **A** and **B** with both cyclic and acyclic substrates. In Scheme 3.2A, subjecting **11** to aziridination conditions in the absence and presence of TEMPO as a radical inhibitor showed a modest 10% decrease in yield, which is not a definitive indication that radical intermediates are involved. In contrast, subjecting **11** to C–H amination conditions did result in a substantial decrease in yield in the presence of TEMPO, indicating the possibility of a radical intermediate. These results suggest that catalysts **A** and **B** operate under mechanistically distinct pathways. However, we note that the C–H amination products of **16** and **17** employing either catalyst **A** or **B** contain a transposed double bond (Table 3.4, entries 11-14). This suggests both silver catalysts are capable of promoting step-wise nitrene transfer pathways involving radical intermediates. Surprisingly, TEMPO inhibition studies with **16** (Scheme 3.2B) show decreased yields of the insertion product, but have little effect on the aziridination yield. Explaining these puzzling results is important for developing better Ag(I) catalysts and were

addressed using computational studies (vide infra).

Scheme 3.3. Influence of the radical inhibitor TEMPO on the amination of acyclic alkene **21**

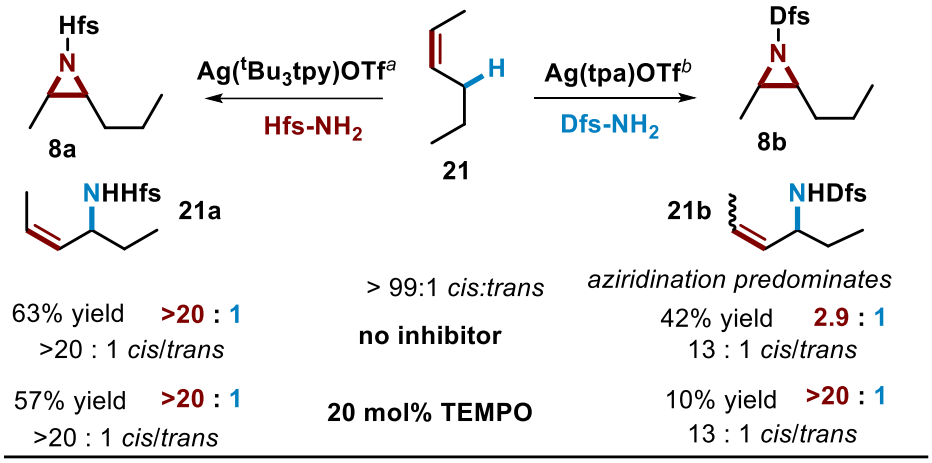

[a]**A**: $HfsNH_2$ (0.25 mmol), 10 mol % AgOTf, 12 mol % $^tBu_3tpy$, 3.5 equiv PhIO, CH_2Cl_2, 4 A MS, 4 h, rt. [b]**I**: $DfsNH_2$ (0.25 mmol), 10 mol % AgOTf, 12 mol % tpa, 1.2 equiv PhIO, CH_2Cl_2, 4 A MS, 1 h, rt.

Further mechanistic studies with acyclic alkenes (Scheme 3.3 and Scheme 3.4) reveal that catalyst **A** generates **21a** exclusively as the cis isomer (Scheme 3.3), while **B** gives **21b** as a 13:1 mixture of cis:trans isomers. Both catalysts favor aziridination, although the selectivity with **B** (2.9:1) is much lower than that observed with **A** (>20:1). Slight isomerization of the alkene from >20:1 cis:trans to 13:1 cis:trans in the C–H amination product **21b** occurs in both the absence and presence of TEMPO.

While the addition of TEMPO using catalyst **B** supported the presence of radical intermediates in the nitrene transfer pathway, the minimal isomerization of **21** (Scheme 3.3) with both **A** and **B** was unexpected. To shed more insight into this question, a sterically congested alkene **22** was subjected to both aziridination and C–H amination conditions (Scheme 3.4). These experiments suggest the presence of radical intermediates in both pathways, as transposition of the alkene double was noted using both catalysts. The question was why catalyst **A** appeared in many cases to give concerted nitrene transfer, as opposed to the clear-cut evidence that **B** proceeded through a stepwise nitrene transfer pathway.

Scheme 3.4. Allylic isomerization studies

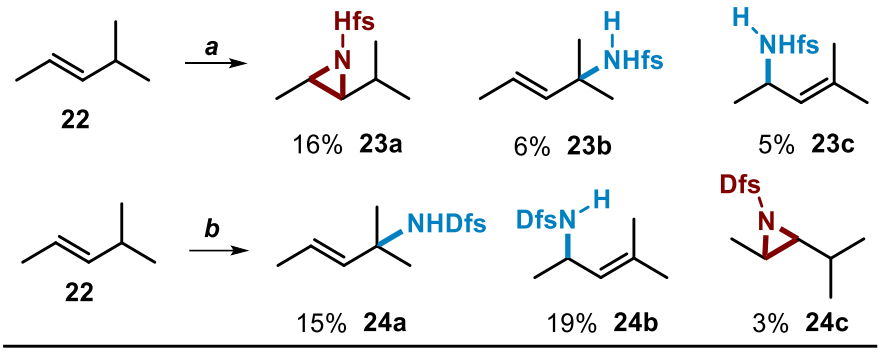

a: 5 equiv **22**, 1 equiv $HfsNH_2$, 10 mol % AgOTf, 12 mol % $^tBu_3tpy$, 3.5 equiv PhIO, 0.05 M CH_2Cl_2, 4 A MS, 4 h, rt. *b:* 5 equiv **22**, 1 equiv $DfsNH_2$, 10 mol % AgOTf, 12 mol % tpa, 1.2 equiv PhIO, 0.05 M CH_2Cl_2, 4 A MS, 1 h, rt.

3.4.2 Computational studies

The only previously reported, extensive computational study on Ag-catalyzed nitrene transfer explores aziridination using a tris-pyrazolyl borate complex (catalyst **C**).[31] Aziridination was found to proceed through an initial hydrogen-atom transfer (HAT) step, but a minimum energy crossing point (MECP) between the triplet and closed-shell singlet surface induces direct formation of the aziridine from the HAT transition state, resulting in retention of the stereochemistry of the alkene. The reactivity observed with our ligands on Ag(I) led to an initial hypothesis that catalyst **A** follows a single-step mechanism similar to that described by Pérez and coworkers, and catalyst **B** follows a stepwise pathway.[31] However, our experimental probes of the mechanism (Scheme 3.2, Scheme 3.3, and Scheme 3.4) yield puzzling results. Experiments in Scheme 3.2 on cyclic alkenes appear to support our hypothesis, as the use of TEMPO as a radical inhibitor did not impact the aziridination pathways involving catalyst **A**. The same is true for the acyclic alkene **21** in Scheme 3.3; however, the data in Scheme 3.4 suggest that even catalyst **A** is capable of promoting step-wise nitrene transfer, as allylic C=C double bond transposition is observed. To find a mechanistic explanation for these seemingly contradictory observations, as well as to investigate the reasons for the chemoselectivity differences between **A** and **B**, we decided

to employ quantum chemical methods to study the reactivity of these two catalysts at the level of density functional theory. Here, B3LYP-D3 is used for the structures of critical points along the reaction coordinates and we employ complete active space self-consistent field (CASSCF) for the electronic structure of the nitrene complexes. The validity of our choice of B3LYP-D3 is demonstrated by benchmarking various functionals against the crystal structure of catalyst **A** and B3LYP-D3 was found to be one of the most robust functional in reproducing the crystal structure (see the Supporting information for quantitative assessments of the functionals).

Structural features of nitrene intermediates. To begin our computational studies, the nitrene complex of **B**, (tpa)Ag(OTf)(NSO_3R) **B(N)**, was optimized with the nitrene ligand bound in the equatorial site (cis to the tertiary amine) and the OTf^- ion bound in the axial site. This nitrene complex of catalyst **B** was chosen for computational studies of its reactivity owing to the fact that the chemoselectivity of **B** is affected by the identity of the Ag salt employed supporting the hypothesis that the anionic OTf ligand remains bound to **B(N)** during catalysis (See the Supporting Information for the discussion of other potential structure of **B(N)**). Catalyst **A** has been shown to exist as a dimer with one of the two OTf ions dissociated in its crystal structure, leaving two inequivalent Ag sites.[7] Ag_N has a coordination sphere composed entirely of $^tBu_3$tpy N atoms, while Ag_O also has a coordinated OTf ion. To improve computational efficiency, the tert-butyl groups on the $^tBu_3$tpy ligand were replaced by H atoms ($[(tpy)AgOTf]_2^+$, called **A′**). The nitrene complex of **A'** was optimized with the nitrene ligand bound to the Ag_N, denoted as **A′(N)**. This coordination isomer was chosen due to the fact that catalyst **A** displays minimal counteranion effects. The effect of the truncation on the structures of **A** and **A(N)** is also assessed in Figures S3 and S4 in the Supporting Information (see Tables S9, S20, and S22 for a quantitative comparison and **A′(N)** and **A′(N_O)**, nitrene binding to the Ag_O atom of catalyst **A**, between **A** and **A′**, and **A(N)** and **A′(N)**,

respectively).The optimized structures of **B(N)** and **A′N** are shown in Figure 3.1.

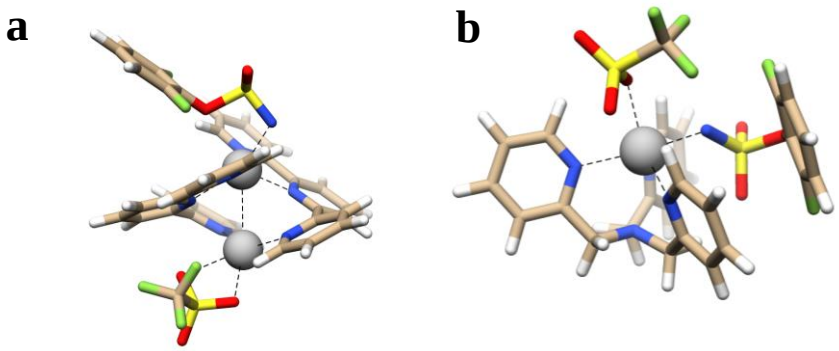

Figure 3.1. The optimized structures of the Ag-nitrene intermediates investigated. **B(N_{eq})** and **A'(N)** are shown on the left (**a**) and right (**b**), respectively.

Electronic features of nitrene intermediates. The electronic structures of **B(N)** and **A'(N)** have been investigated both at the density functional (DFT) and complete active space self-consistent field (CASSCF) levels of theory. For both **B(N)** and **A'(N)**, the lowest energy state was found by DFT to be a triplet state, in which a Ag(II) ion is ferromagnetically coupled to a doublet nitrene anion radical (Ag(II)↑–↑{NSO_3R}$^-$). The ferromagnetic alignment of spins in this complex is due to the orthogonality of the Ag–N σ* and N p_π magnetic orbitals. Analysis of the Kohn-Sham orbitals shows that the Ag–N bond is composed of a 3-electron σ component and a 3-electron π component, with an overall calculated Mayer bond order of 0.56 and 0.57 for the (antiferromagnetically coupled) open-shell (OS) singlet and triplet **B(N)**, respectively, and 0.63 and 0.55 for OS singlet and triplet **A'(N)**, respectively. The σ* orbital in both complexes is strongly covalent with ~20% polarization toward Ag, whereas the π* orbital is strongly polarized towards the nitrene N atom by 85–90%. The OS singlet excited state is low-lying, at 4.13 and 8.27 kcal·mol^{-1} above the triplet ground state for **B(N)** and **A'(N)**, respectively. The frontier orbitals are shown in Figure S5. Analysis of the CASSCF wave function indicates that there is only one configuration that contributes strongly to the electronic structure of both complexes in their triplet state. This configuration can be described as $(\sigma)^2(\pi'^*)^2(\pi''^*)^1(\sigma^*)^1$. On the other hand, the OS singlet has

multi-configurational character with a major configuration (~70%) of $(\sigma)^2(\pi'^*)^2(\pi''^*)^2(\sigma^*)^0$ and a minor configuration (~30%) of $(\sigma)^2(\pi'^*)^2(\pi''^*)^0(\sigma^*)^2$. A second closed-shell (CS) singlet excited state, discussed previously in the literature,[31] was located 7.23 and 12.1 kcal·mol^{-1} above the triplet ground state for **B(N)** and **A'(N)**, respectively. This particular excited state, which could be described as either a Ag(I) ion bound to a singlet nitrene or a Ag(III)-imido complex, is not discussed due to its high energy.

We recently discussed the necessity for a metal-nitrene intermediate to have a pair of empty α and β molecular orbitals with N character in order to be able to undergo concerted nitrene transfer.[59] Given this constraint, we would expect nitrene transfer from these silver complexes with triplet ground states (i.e., having two empty β molecular orbitals with N character) to occur via a stepwise mechanism. However, Pérez and coworkers found in their computational study that it is possible for intersystem crossing to occur directly following an initial single-electron transition state in such a way as to avoid radical-containing intermediate species.[31] Thus, an examination of the nitrene transfer potential energy surface (PES) for both **A'(N)** and **B(N)** is warranted.

Reactivity landscape for nitrene transfer. PESs for nitrene transfer from **B(N)** to substrate **1** modeling experimental chemoselectivity. Two distinct transition states (TSs) have been located as substrate **1** approaches **B(N)**. The first involves partial formation of an N–H bond (C–H bond amination (**I**), $\mathbf{TS_{tpa,I,1}}$, the numerical subscript denotes the substrate identity) on either the triplet (^{3}**TS**) or OS singlet (^{OS1}**TS**) potential energy surface (PES). The second TS involves partial formation of a C–N bond (aziridination (**A**), $\mathbf{TS_{tpa,A,1}}$) on the triplet (^{3}**TS**) PES. Both $^{OS1}\mathbf{TS_{tpa,I,1}}$ and $^{3}\mathbf{TS_{tpa,I,1}}$ were found to be lower in energy than the $^{3}\mathbf{TS_{tpa,A,1}}$ (10.1 and 10.2 vs 10.7 kcal·mol^{-1}, respectively), consistent with the experimentally observed chemoselectivity. After HAT is complete, intermediates (**Int**) were found on both the OS singlet ($^{OS1}\mathbf{Int_{tpa,I,1}}$) and triplet ($^{3}\mathbf{Int_{tpa,I,1}}$)

PES (–19.2 and –19.7 kcal·mol^{-1}, respectively), with a slight favoring of the triplet state. Radical rebound occurs without an energetic barrier after the complete formation of ^{OS1}**Int**$_{tpa,I,1}$ on the OS singlet surface to give the aminated product and regenerate catalyst **B** (–71.4 kcal·mol^{-1}). The complete reaction coordinate for both reactions catalyzed by **B(N)** is shown in Figure 3.2. The presence of an intermediate after hydrogen-atom abstraction on both the OS singlet and triplet PESs and the fact that the two intermediates are close in energy suggest that the ^{3}**Int**$_{tpa,I,1}$ could be long-lived enough to be trapped by radical inhibitors. This finding is consistent with our experimental observations that a radical quencher lowers the yield of the C–H inserted product of **1N**$_{eq}$ in the reactions of **11** and **21** (Scheme 3.2-Scheme **3.3**). In contrast, substrate aziridination by **B(N)** occurs on the triplet PES via ^{3}**TS**$_{tpa,A,1}$; no ^{OS1}**TS**$_{tpa,A,1}$ was located. Complete formation of the C–N bond gives ^{3}**Int**$_{tpa,A,1}$; a reorganization of the electronic structure is presumed to occur to give ^{OS1}**Int**$_{tpa,A,1}$ (kcal·mol^{-1} in terms of vertical excitation energy), which then leads to the formation of the aziridine product, ^{1}**PC**$_{A,tpa,1}$. Similar to the case for C–H insertion, the presence of ^{3}**Int**$_{tpa,A,1}$, along with the absence of a concerted ^{OS1}**TS**$_{tpa,A,1}$, suggest that trapping by radical inhibitors is possible (vide infra), a hypothesis that is consistent with our experimental observations.

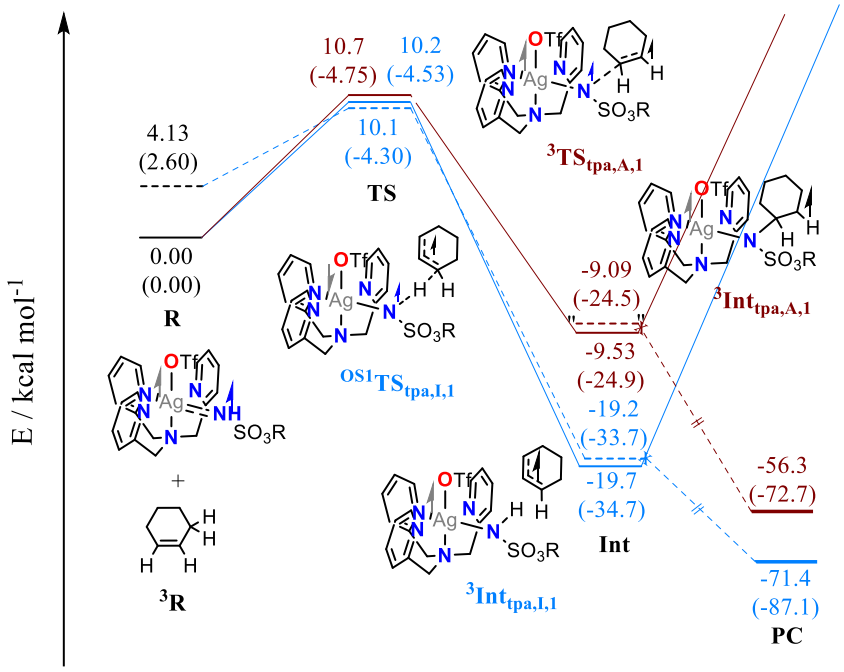

Figure 3.2. Reaction coordinate of nitrene transfer from **B(N)** to **1** to give either the C–H amination (**blue**) or aziridine product (**brown**). **R** = reactant, **TS** = transition state, **Int** = intermediate, and **PC** = product complex. Subscript **I** = C–H insertion and **A** = aziridination; superscript **OS1** and **3** denote open-shell singlet and triplet spin states, respectively. Solid lines denote the triplet potential energy surface (PES) and dashed lines denote the open-shell singlet PES. Arrows and the size of the arrows represent α or β spin populations for the electrons on Ag (silver), blue for N (blue), and black (organic substrate). Black arrows inside the ring indicate that electron density is delocalized over the allylic radical and arrows outside the ring represent electron density localized on the carbon proximal to the arrow. Numbers shown are Gibbs free energies; numbers enclosed in parentheses are enthalpies, both taking into account the solvent (CH_2Cl_2). Note: the energy for the blue dashed line enclosed by quotation marks was obtained from converging the single point energy at the OS singlet state based on the geometry of the solid blue line below it.

PESs for nitrene transfer from **A'(N)** to substrate **1** modeling experimental chemoselectivity. Four distinct **TSs** are located as **1** approaches **A'(N)**. Partial formation of the N–H bond ($\mathbf{TS_{tpy,I,1}}$) or C–N bond ($\mathbf{TS_{tpy,A,1}}$) occurs on either the triplet or OS singlet PES. $^{3}\mathbf{TS_{tpy,I,1}}$ and $^{3}\mathbf{TS_{tpy,A,1}}$ are lower in energy than $^{OS1}\mathbf{TS_{tpy,I,1}}$ and $^{OS1}\mathbf{TS_{tpy,A,1}}$ by 5.10 and 7.62 kcal·mol^{-1}, respectively. $^{3}\mathbf{TS_{tpy,A,1}}$ was found to be lower in energy than $^{3}\mathbf{TS_{tpy,I,1}}$ (9.38 vs 11.4 kcal·mol^{-1}) in agreement with the experimental selectivity. Both $^{3}\mathbf{TS_{tpy,I,1}}$ and $^{3}\mathbf{TS_{tpy,A,1}}$ lead to the formation of triplet state intermediates, $^{3}\mathbf{Int_{tpy,I,1}}$ and $^{3}\mathbf{Int_{tpy,A,1}}$ (–16.0 and –8.32 kcal·mol^{-1}, respectively). However, these intermediates do not evolve to form products on the triplet surface. Instead, it was

found that ^{OS1}**TS**$_{tpy,I,1}$ and ^{OS1}**TS**$_{tpy,A,1}$ lead to the direct formation of product complexes, ^{1}**PC**$_{tpy,I,1}$ and ^{1}**PC**$_{tpy,A,1}$, respectively (–81.7 and –62.5 kcal·mol^{-1}, respectively) without accessing an intermediate. The complete reaction coordinate for both reactions by **A'(N)** is shown in Figure 3.3. The experimental observation that **A** is resistant to inhibition by TEMPO (Scheme 3.2 and Scheme 3.3) suggests that direct access of the OS PES after ^{3}**Int**$_{tpy}$ (the crosses in Figure 3.3) to yield products is the major reaction pathway (vide infra).

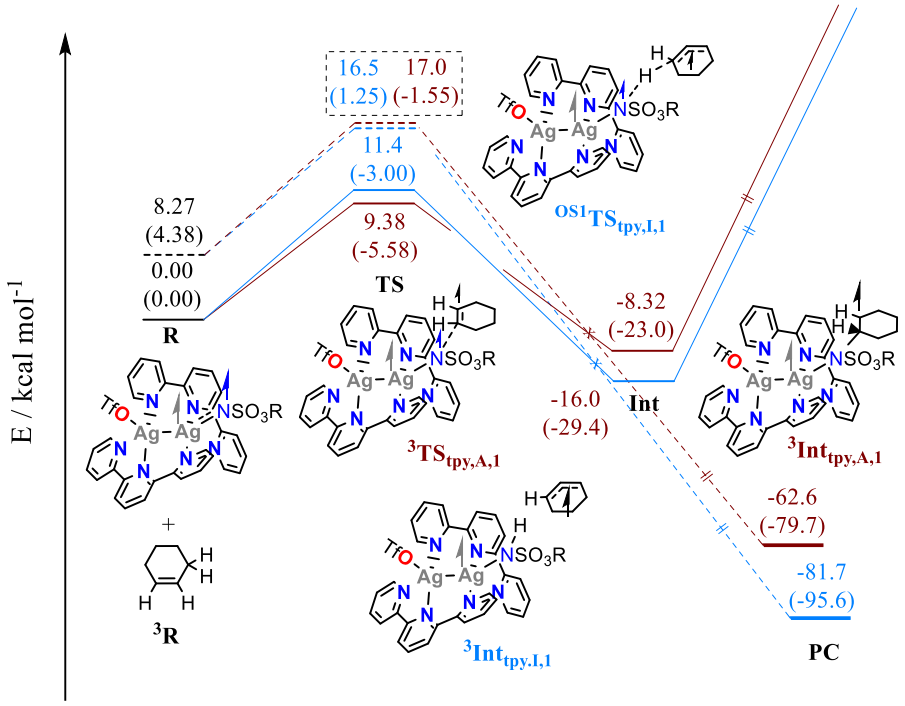

Figure 3.3. Reaction coordinate of nitrene transfer from **A'(N)** to **1** to give either C-H insertion (**blue**) or aziridine products (**brown**). **R** = reactant, **TS** = transition state, **Int** = intermediate, and **PC** = product complex. Subscript **I** = C–H insertion and **A** = aziridination and superscript OS1 and 3 denote open-shell singlet and triplet spin states, respectively. Solid lines denote the triplet potential energy surface (PES) and dashed lines denote the open-shell singlet PES. Arrows and the size of the arrows represent α or β spin populations for the electrons on Ag (silver), N (blue), and organic substrate (black). Black arrows inside the ring represent electron density delocalized over the allylic radical and arrows outside the ring represent electron density localized on the carbon proximal to the arrow. Numbers shown are Gibbs free energies and numbers enclosed in parentheses are enthalpies, both taking into account the solvent (CH_2Cl_2).

The shape of the PES and the experimentally observed tolerance of the aziridination pathway towards radical inhibition are strongly reminiscent of the system described by Pérez and

coworkers for Ag complexes supported by tripodal ligands.[31] These resemblances prompted us to perform a comparison between **B(N)**, **A'(N)**, and the Pérez (Tp^{Me2})Ag(NTs) (**C(N)**; Tp^{Me2} = hydro(3,5-dimethyl-1-pyrazolylborate) system in order to achieve a deeper understanding of reactivity in our silver-catalyzed intermolecular nitrene transfer reactions.

Differential mechanisms for nitrene transfer from **B(N)**, **A'(N)**, and **C(N)** to organic substrates. Results for the reaction coordinates of nitrene transfer from **B(N)** and **A'(N)** to substrate **1** (vide supra) contrast with those recently reported for Ag-nitrene intermediates supported by tripodal Tp ligands.[31, 60] In previously reported examples, only a triplet and CS singlet state were located, with the triplet favored in energy by 7.6 kcal·mol^{-1}.[31] The large spin population of 1.32 on the N atom, along with the inability to locate an OS singlet state, led to the description of **C(N)** as a Ag(I) complex with a coordinated triplet nitrene ligand. In contrast, we located OS singlet states for **B(N)** and **A'(N)** with spin populations (–0.78 on N and 0.78 on (tpa)Ag for **B(N)** and –0.74 on N and 0.67 on $(tpy)_2Ag_2$ for **A'(N)**), which prompt us to describe these silver nitrene complexes as Ag(II) ions coupled to nitrene anion radicals, despite the fact that spin densities on the triplet states are similar to that of **C(N)** (1.26 on N and 0.74 on (tpa)Ag for **B(N)** and 1.27 on N and 0.64 on $(tpy)_2Ag_2$ for **A'(N)**).

Scheme 3.5. Comparisons among **A'(N)**, **B(N)**, and **C(N)**

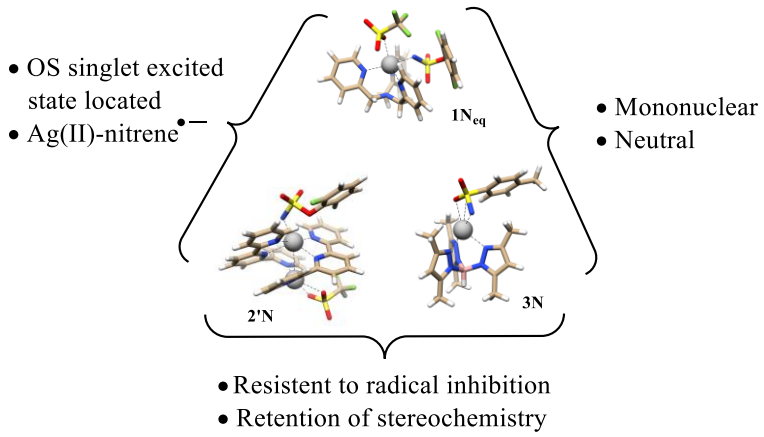

Unlike either **A′(N)** or **C(N)**, **B(N)** performs nitrene transfer via a mechanism that generates **Int$_{tpa}$** on both the triplet and OS singlet PESs. This allows radical inhibition of the reaction, in contrast to the tolerance towards TEMPO exhibited by **A′(N) C(N)** (**Scheme 3.5**). Importantly, the divergence in mechanism between these three catalysts occurs after the initial transition state. Therefore, the differences in the mechanism for nitrene transfer from **B(N)**, **A'(N)**, and **C(N)** are not likely due to their different ground state electronic structures. Instead, the nature of the transition states needs to be examined along with the thermodynamic driving forces en route to product formation.

Scheme 3.6. Diagrams of concerted and HAT transition state geometries for C–H amination, including the features of stepwise transition states vs those leading to barrierless rebound

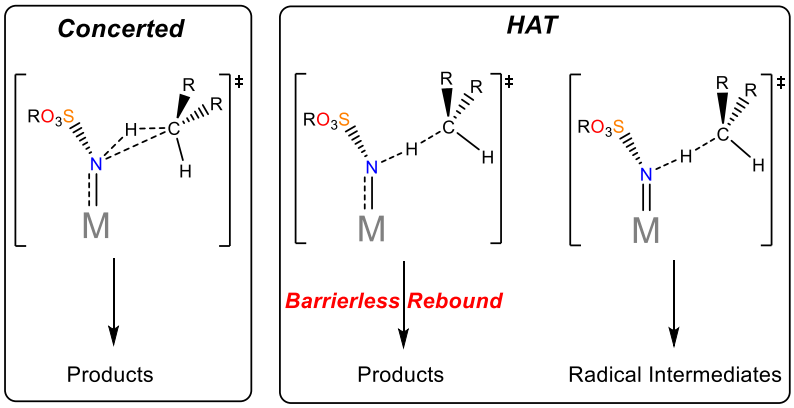

Nature of the C–H amination transition states from **A(N)**, **B(N)**, and **C(N)**. It is useful to examine the general geometrical features of nitrene transfer transition states. For simplicity, we will analyze in detail only the C–H amination transition states. In concerted insertions of nitrenes into C–H bonds, as is seen in Rh_2-catalyzed reactions, the transition state involves simultaneous (though asynchronous) C–N and N–H bond formation and C-H cleavage.[59] These three interactions take place within a triangular, three-membered ring transition state (left, Scheme 3.6). Stepwise reactions proceed first through a hydrogen atom transfer (HAT) transition state leading to radical intermediates. The transition state involves a linear N···H···C geometry (right, Scheme 3.6). These geometries are electronically dictated: the three-membered ring transition state requires a stabilizing pair of electrons and therefore an empty N orbital (or a pair of α/β holes with N

characters for broken symmetry cases) to accept the electrons of the C–H bond. The linear N···H···C structures result from three-center/three(or four)-electron bonds and are seen for the more electron-rich systems. All silver-nitrene complexes are electron rich and will therefore use HAT transition states for C–H amination (and corresponding single-electron transition states for aziridination). The major question of this work, however, is to explain when the HAT transition state leads to the formation of radical intermediates vs when it is followed by a barrierless rebound.

Table 3.5. Geometrical features of optimized transition states

C–C Amination Transition States			
Catalyst	**Spin State[a]**	**∠N···H···C, °**	**Δd(Ag–N)[b], Å**
A′	Singlet	171	0.03
	Triplet	172	0.05
B	Singlet	173	–0.03
	Triplet	176	0.01
Aziridination Transition States			
Catalyst	**Spin State[a]**	**Δd(N–C)[c], Å**	**Δd(Ag–N)[b], Å**
A′	Singlet	0.627	0.01
	Triplet	0.736	0.06
B	Triplet	0.626	0.03
C	Singlet	0.335	–0.06
	Triplet	0.625	0.04

[a] The singlet spin states are all optimized open-shell singlets. [b] Δd(Ag–N) is defined as the difference in Ag–N(nitrene) bond distance between the transition state geometry and the reactant complex geometry. [c] Δd(N–C) is defined as the difference between the two N···C distances in the transition state.

Geometric details of the C–H amination transition states of catalysts **A**, **B**, and **C** are given in Table 3.5 (a more complete set of data for catalyst **A′** and **B** is given in Tables S23, S24 and Tables S27 and S28, respectively, in the Supporting Information). Since catalyst **A** performs C–H

amination via a barrierless recombination pathway and **B** via a stepwise pathway, it is useful to compare their geometric differences. Both catalysts feature typical HAT transition states with N···H···C angles very close to linearity. However, the lowest-energy transition state (triplet) for catalyst **A′** also clearly shows signs of Ag–N bond cleavage character, since its Ag–N bond length is increased by 0.05 Å from the geometry of **A′(N)**. The Ag–N bond length for **B** is unchanged (0.01 Å). The observation that transition states leading to barrierless recombination involve Ag–N bond cleavage is also true of aziridination transition states. Catalysts **A** and **C** undergo aziridination via barrierless rebound, and their Ag–N bond distances are elongated by 0.06 and 0.04 Å, respectively in their transition state geometries.

This geometrical observation is also supported by an energetic analysis. First, we compare $\Delta H^{\ddagger}$ of the singlet and triplet transition states. In contrast to **B(N)**, which has a similar enthalpic driving force at both $^{\mathbf{OS1}}\mathbf{TS_{tpa,I,1}}$ and $^{\mathbf{3}}\mathbf{TS_{tpa,I,1}}$ ($\Delta\Delta H^{\ddagger,OS1-3}_{CH_2Cl_2}$= 0.23 kcal·mol^{-1}), $^{\mathbf{OS1}}\mathbf{TS_{tpy,1}}$ for **A′(N)** is much less exothermic than $^{\mathbf{3}}\mathbf{TS_{tpy,1}}$ ($\Delta\Delta H^{\ddagger,OS1-3}_{CH_2Cl_2}$ = 3.08 kcal·mol^{-1} for $\mathbf{TS_{tpy,A,1}}$ and $\Delta\Delta H^{\ddagger,OS1-3}_{CH_2Cl_2}$ = 3.34 kcal·mol^{-1} for $\mathbf{TS_{tpy,I,1}}$). Since the $\Delta H^{\ddagger}_{CH_2Cl_2}$ for the formation of the first C–N bond in aziridination and the N–H bond in C–H insertion should be very similar on both PESs, the difference in $\Delta H^{\ddagger}_{CH_2Cl_2}$ between $^{\mathbf{3}}\mathbf{TS_{tpy}}$ and $^{\mathbf{OS1}}\mathbf{TS_{tpy}}$ must result mainly from the breaking of the Ag–N bond during $^{\mathbf{OS1}}\mathbf{TS_{tpy}}$. Comparing the Ag–N bond lengths in **B(N)** and **A'(N),** they differ by ~ 0.07 Å, a difference that may be attributed to partial chelating character of the nitrene ligand in **A′(N)**, which contains a weak Ag···O interaction of 2.7 Å, reminiscent of the quasi-bidentate nitrene coordination mode in **C(N)**. This implies that the bond between Ag and N is stronger in the OS singlet **A'(N)** than in the triplet **A'(N)**; thus, it takes more energy to break the Ag–N bond during $^{\mathbf{OS1}}\mathbf{TS_{tpy}}$ to form the bond with the incoming atom from the substrate ($\Delta(Ag–N)_{\mathbf{TS–R}}$ = +0.062 Å for $^{\mathbf{OS1}}\mathbf{TS_{tpy,A,1}}$ and $\Delta(Ag–N)_{\mathbf{TS–R}}$ = +0.077 Å for $^{\mathbf{OS1}}\mathbf{TS_{tpy,I,1}}$ vs $\Delta(Ag–N)_{\mathbf{TS–R}}$ = -0.01 Å

for ^{OS1}**TS$_{tpa,I}$**). Once past ^{OS1}**TS$_{tpy}$**, the Ag–N bond has elongated enough to form ^{1}**PC$_{tpy}$** in a barrierless radical recombination step. The transient process leading to the formation of ^{1}**PC$_{tpy}$** means that the **A'(N)**-substrate complex must cross from ^{3}**TS$_{tpy}$** to ^{1}**PC$_{tpy}$** through an MECP (where dashed and solid lines cross in Figure 3.2 and Figure 3.3). Through this analysis, we observe that nitrene complexes with a semi-chelating coordination mode to Ag lead to nitrene transfer transition states having significant Ag–N bond cleavage character, which results in barrierless recombination and an absence of radical intermediates.

Interplay of enthalpy and entropy of activation on the differential chemoselectivity of nitrene transfer from **B(N)** and **A'(N)** to substrate **1**. The differential chemoselectivity of nitrene transfer from **B(N)** and **A'(N)** to substrate **1** is satisfactorily reproduced by DFT studies of the reaction coordinates on both the triplet and OS singlet PESs ($(P_I{:}P_A)^{calc}_{1N_{eq}} \approx (k_I{:}k_A)^{calc}_{1N_{eq}} = 2.60{:}1$ using ^{OS1}**TS$_{tpa,1,I}$** or $(k_I{:}k_A)^{calc}_{1N_{eq}} = 2.3{:}1$ using ^{3}**TS$_{tpa,1,I}$** vs $(P_I{:}P_A)^{exp}_{1N_{eq}} = 5.8{:}1$; $(P_I{:}P_A)^{calc}_{2'N} \approx (k_I{:}k_A)^{calc}_{2'N} = 1{:}30.7$ vs $(P_I{:}P_A)^{expt}_{2'N} = 1{:}5.2$; see below for the origin of the approximately equal signs). The agreement with experiment justifies a further analysis of thermodynamic parameters, namely enthalpy, entropy, and Gibbs free energy of activation/formation. Activation of the C=C bond on the triplet PES is the most exothermic step among all TSs for both **B(N)** and **A'(N)** (Table 3.6). This is sensible, as breaking the C=C π-bond in an alkene is less energetically costly than breaking the C–H σ-bond at an allylic position.[61-62] However, when the entropy of activation is taken into account, **B(N)** suffers more than **A'(N)** for both C–N bond formation and HAT. The fact that **B(N)** is more negatively impacted by $\Delta S_A^{\ddagger}$ is due to steric hindrance around the nitrene site, which restricts the flexibility of the incoming substrate, as can be seen from space-filling models of **B(N)** and **A'(N)** (

Figure 3.4). This larger negative entropic contribution of ^{3}**TS$_{tpa,1}$** in general, and of

^{3}**TS$_{tpa,A,1}$** compared to ^{3}**TS$_{tpa,I,1}$**, is the major thermodynamic factor in the differential chemoselectivity of **B(N$_{eq}$)** and **A'(N)**. Hence, the chemoselectivity of **A'(N)** towards aziridination of **1** is enthalpy-driven while that of **B(N)** towards amination of **1** is entropy-driven.

Table 3.6. Enthalpy (kcal·mol^{-1}), entropy (cal·mol^{-1}·K^{-1}), and Gibbs free energy (kcal·mol^{-1}) of activation for nitrene transfer from **B(N$_{eq}$)** to **1** and **21** on either the triplet or OS singlet surface

TS	substrate	$\Delta H^{\ddagger}_{CH_2Cl_2}$	$\Delta S^{\ddagger}$	$\Delta G^{\ddagger}_{CH_2Cl_2}$
^{OS1}**TS$_{tpa,I}$**	**1**	–4.30	–48.3	10.1
^{3}**TS$_{tpa,I}$**	**1**	–4.53	–49.5	10.2
^{3}**TS$_{tpa,A}$**	**1**	–4.75	–51.7	10.7
^{3}**TS$_{tpy,I}$**	**1**	–3.00	–48.3	11.0
^{3}**TS$_{tpy,A}$**	**1**	–5.58	–50.2	9.38
^{OS1}**TS$_{tpa,I}$**	**21**	–4.89	–57.0	12.1
^{3}**TS$_{tpa,I}$**	**21**	–0.51	–47.5	13.7
^{3}**TS$_{tpa,A}$**	**21**	–4.69	–53.4	11.2

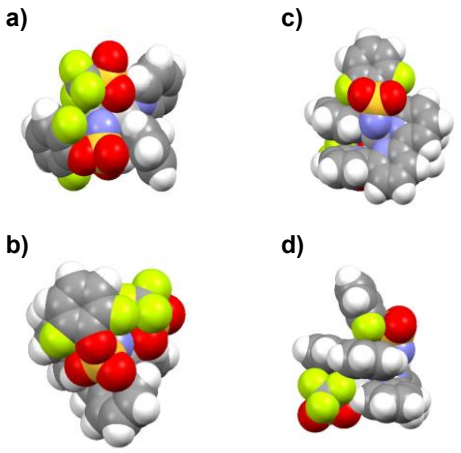

Figure 3.4. Space-filling models of **B(N$_{eq}$)** a) viewed from the top of the nitrene and b) viewed from the side. Space-filling models of **A'(N)** c) viewed from the top of the nitrene and d) viewed from the side. Color code: Ag:grey, S:yellow, F:green, O:red, N:blue, C:black, and H:white.

Fine-tuning the chemoselectivity of nitrene transfer from **B(N)** to cyclic vs acyclic alkenes. To further examine our hypothesis that the interplay of $\Delta H^{\ddagger}$ and $\Delta S^{\ddagger}$ fine-tunes the

chemoselectivity of Ag-nitrene complexes, the reaction coordinate for nitrene-transfer from **B(N)** to acyclic substrate **21** was studied. Replacing cyclic alkenes by acyclic alkenes (i.e., **1** by **21**) changes the experimental chemoselectivity of **B(N)**. Correspondingly, we found that the lowest energy **TS** is the aziridination transition state ^{3}**TS**$_{\mathbf{tpa,A,21}}$, which is 0.89 kcal·mol^{-1} more stable than the lowest energy C–H amination transition states **TS**$_{\mathbf{tpa,I,21}}$, ^{OS1}**TS**$_{\mathbf{tpa,I,21}}$. This gives $k_A/k_I = 4.52 \approx P_A/P_I$, assuming that the product-determining steps are the rate-determining steps. Note that there are only two internal secondary allylic C–H bonds in **21**, compared to four accessible C=C sites comprised of C2-re, C2-si, C3-re and C3-si. This could potentially increase P_A/P_I to 9.04. The calculated product ratios match the experimental product ratio of 2.9:1 well and, more importantly, the observed chemoselectivity. To understand the influence of $\Delta H^{\ddagger}$ and $\Delta S^{\ddagger}$ on the change of chemoselectivity from **1** to **21**, their contributions to the **TS**$_{\mathbf{tpa}}$ are summarized in Table 3.6. $\Delta H^{\ddagger}_{CH_2Cl_2}$ is more favorable for HAT than C–N bond formation for **21** as compared to **1**, because the migrating allylic C–H bond can adopt a nearly coplanar alignment with the π orbitals of the C=C bond to allow some degree of resonance stabilization as the C–H bond starts to break. This stabilization is less prominent in **1** due to the constraint imposed by the cyclic structure (Figure 3.5). However, the staggered conformation of **21** forces the propyl substituent to impose steric hindrance on **B(N)**, a feature that is absent in **1**. The reason for this is the constraint imposed by the cyclic structure of **1** that forces C4 to stay in a pseudo-gauche conformation with respect to the C=C bond (Figure 3.6). This steric effect reflects heavily on $\Delta S^{\ddagger}$, hence making ^{3}**TS**$_{\mathbf{tpa,A,21}}$ more energetically accessible than ^{OS1}**TS**$_{\mathbf{tpa,I,21}}$.

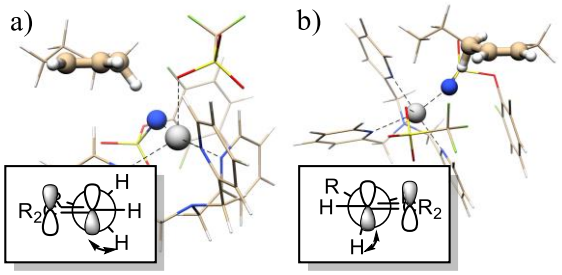

Figure 3.5. Structure of ^{OS1}**TS**$_{tpa,I,1}$ (a) and ^{OS1}**TS**$_{tpa,I,21}$ (b). The allylic group, nitrene N atom, and the Ag atom are shown in spheres for emphasis. Insets: Neumann projections of substrate looking down along C2–C3 bond (a) or C3–C4 bond (b).

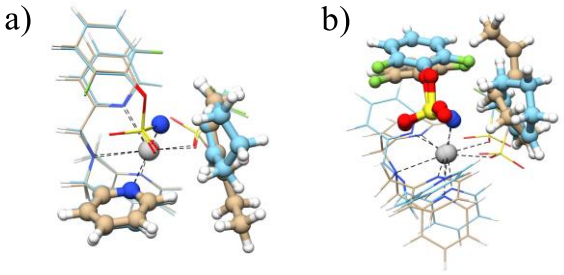

Figure 3.6. a) Overlay of ^{3}**Int**$_{tpa,A,21}$ (mostly in beige) and ^{3}**Int**$_{tpa,A,1}$ (mostly in blue). Ag, the nitrene N, the pyridyl group closest to substrates, and substrates are shown in spheres for clarity. b) Overlay of ^{3}**Int**$_{tpa,I,21}$ (mostly in beige) and ^{3}**Int**$_{tpa,I,1}$ (mostly in blue). Ag, the aryl sulfamate, and substrates are shown in spheres for clarity.

The C=C cis/trans isomerization of acyclic alkene **21** during nitrene transfer from **B(N)**. Radical intermediates are found on both triplet and OS singlet surfaces for **B**, with ^{3}**Int**$_{tpa,I}$ lower in energy by only 0.6 kcal·mol^{-1}. However, ^{3}**Int**$_{tpa,I}$ cannot lead to the formation of products without first accessing ^{OS1}**Int**$_{tpa,I}$ via a minimum energy crossing point (MECP: where crosses are located in Figure 3.3) to allow the conservation of spin symmetry. The presence of an MECP after the initial formation of ^{3}**Int**$_{tpa,I}$ suggest that this species will be relatively long-lived. In turn, this increased lifetime allows cis/trans isomerization of the allylic C=C bond via C–C rotation of the diradical ^{3}**Int**$_{tpa,I}$ species to occur. This also explains why TEMPO inhibition is observed (Scheme 3.3). Similar arguments apply to **Int**$_{tpa,A,}$. To further support this hypothesis, the trans-isomer of **Int**$_{tpa,21}$ (**Int**$^{iso}_{tpa,21}$) was considered. Indeed, ^{3}**Int**$^{iso}_{tpa,A,21}$ and ^{3}**Int**$^{iso}_{tpa,I,21}$ were located and found to

be more stable than their cis-isomers (–7.02 kcal·mol^{-1} for $^{3}\mathbf{Int}^{\mathbf{iso}}_{\mathbf{tpa,I,21}}$ and –3.55 kcal·mol^{-1} for $^{3}\mathbf{Int}^{\mathbf{iso}}_{\mathbf{tpa,A,21}}$). This result implies that a pre-equilibrium between the two isomers occurs before radical recombination to yield the trans isomer as the major product. However, the distribution of different isomers also depends on the kinetic barrier of the isomerization, which, in turn, depends on the specific steric constraints of the substrate and the degree of C=C bond character in $\mathbf{Int}_{\mathbf{tpa,21}}$, i.e. the C=C bond is completely broken in $\mathbf{Int}_{\mathbf{tpa,A,1}}$ to give a carbon radical at C3 while the C=C bond is half broken in $\mathbf{Int}_{\mathbf{tpa,I,1}}$ to stabilize the carbon radical at C4 after HAT through resonance (Figure 3.7). This can be seen structurally in Figure 3.7a where the methyl group on C2 and the propyl group on C3 are no longer coplanar in $^{3}\mathbf{Int}_{\mathbf{tpa,A,21}}$ and $^{3}\mathbf{Int}^{\mathbf{iso}}_{\mathbf{tpa,A,21}}$. Hence, we would expect more cis/trans isomerization in the aziridine products than in the aminated products, which is indeed what we observe experimentally (see Scheme 3.3).

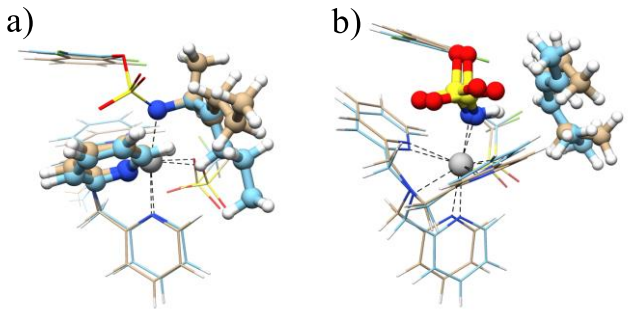

Figure 3.7. a) Overlay of $^{3}\mathbf{Int}_{\mathbf{tpa,21,A}}$ (mostly in beige) and $^{3}\mathbf{Int}^{\mathbf{iso}}_{\mathbf{tpa,21,A}}$ (mostly in blue). The rest of the molecule except Ag, nitrene N, the pyridyl group closed to **21**, and substrate **21** is omitted for clarity. b) Overlay of $^{3}\mathbf{Int}_{\mathbf{tpa,I,21}}$ (mostly in beige) and $^{3}\mathbf{Int}^{\mathbf{iso}}_{\mathbf{tpa,I,21}}$ (mostly in blue), the rest of the molecule except Ag, the sulfamate, and substrate **21** is omitted for clarity.

Timing of intersystem crossing and C=C bond transposition. MECPs are required to be present after the transition states in the reaction trajectories from both **A'(N)** and **B(N).** Yet, the two Ag-nitrene complexes display dissimilar reactivity. As discussed above, for catalyst **B**, the MECP must occur after intermediate formation and this feature "delays" the formation of products allowing a by-product shunt to occur through bimolecular collision of $\mathbf{Int}_{\mathbf{tpa}}$ with TEMPO. On the

other hand, for catalyst **A**, the MECP must occur before the formation of intermediates, because no radical byproducts are observed, with the exception of C=C bond transposition products seen with substrate **16**. Thus, the potential energy surface for this substrate was examined more closely. For this substrate, as the allylic C–H bond on **16** breaks in the (triplet) transition state, electronic reorganization occurs almost instantaneously, as compared to the nuclear movement to form the C–N bond giving products**.** The HAT nature of the transition state yields an allylic radical with the unpaired electron with spin population on both C1 and C3. Bond formation between C1 and N occurs immediately on the OS singlet PES to give **16d**. The driving force favoring C1 over C3, which is mostly steric, is due to $\Delta S^{\ddagger}$ (vide infra), hence giving the thermodynamic product. Indeed, **16d** is formed directly (with no intermediates) as the product after $^{OS1}\mathbf{TS}_{\mathbf{tpy}}$, consistent with experimental observations (Table 3.1 and Scheme 3.2. Influence of TEMPO on the amination of 11 and 16). Thus, although C=C double bond transposition in this case was initially suggestive of a stepwise mechanism with radical intermediates, we find computationally that this transposition can occur via a barrierless recombination and does not necessitate a long-lived diradical intermediate. This reactivity is therefore consistent with an HAT mechanism with barrierless rebound from **A'(N)**.

3.5 Conclusion

In conclusion, we have reported the first examples of simple silver catalysts capable of tunable, non-directed and intermolecular chemoselective amination. We have found catalyst systems that demonstrate complementary chemoselectivities in alkenes containing sites for both aziridination and C–H amination in nitrene transfer, largely independent of substrate identities. Computational studies showed that the tunable chemoselectivity between tpa and ^{t}bu$_3$tpy ligands

is a result of the steric profile around the Ag-nitrene intermediates. The means to tune the steric bulk around the nitrene site without changing the electronic structure of the silver-nitrene intermediates, such as the size of the bound counteranion, could potentially afford an additional tunability within the same ligand system. Furthermore, two distinct nitrene-transfer mechanisms are observed in the computational results, the first involving HAT from catalyst **A** to yield radical intermediates, and the second having HAT from **B** followed by a barrierless recombination step that preserves stereochemistry. The major distinction between these two mechanisms appears to be the extent to which the Ag–N bond breaks during the HAT transition state. Future studies are focused on the development of increasingly selective amination catalysts using a broader array of supporting ligands and counteranions. The ability to correlate the coordination geometry of the catalyst with both reaction mechanism pathways and selectivity are goals currently under investigation.

3.6 Acknowledgements

J.F.B. thanks the Center for Selective C−H Functionalization supported by the National Science Foundation (CHE-1700982). The computational facility at Madison is supported in part by National Science Foundation Grant CHE-0840494 and at the UW—Madison Center for High Throughput Computing (CHTC) in the Department of Computer Sciences. The CHTC is supported by UW—Madison, the Advanced Computing Initiative, the Wisconsin Alumni Research Foundation, the Wisconsin Institutes for Discovery, and the National Science Foundation, and is an active member of the Open Science Grid, which is supported by the National Science Foundation award 1148698 and the U.S. Department of Energy's Office of Science.

3.7 Supplementary Information

The Supporting Information is available free of charge on the ACS Publications website at DOI: 10.1021/jacs.5b12790.

3.8 References

1. Bagchi, V.; Paraskevopoulou, P.; Das, P.; Chi, L.; Wang, Q.; Choudhury, A.; Mathieson, J. S.; Cronin, L.; Pardue, D. B.; Cundari, T. R.; Mitrikas, G.; Sanakis, Y.; Stavropoulos, P., A versatile tripodal Cu(I) reagent for C-N bond construction via nitrene-transfer chemistry: Catalytic perspectives and mechanistic insights on C-H aminations/amidinations and olefin aziridinations. *J. Am. Chem. Soc.* **2014,** *136* (32), 11362-11381.
2. Barman, D. N.; Nicholas, K. M., Copper-catalyzed intramolecular C-H amination. *Eur. J. Org. Chem.* **2011,** (5), 908-911.
3. Collet, F.; Dodd, R. H.; Dauban, P., Catalytic C-H amination: Recent progress and future directions. *Chem. Commun.* **2009,** (34), 5061-5074.
4. Collet, F.; Lescot, C.; Dauban, P., Catalytic C-H amination: The stereoselectivity issue. *Chem. Soc. Rev.* **2011,** *40* (4), 1926-1936.
5. Collet, F.; Lescot, C.; Liang, C.; Dauban, P., Studies in catalytic C-H amination involving nitrene C-H insertion. *Dalton Trans.* **2010,** *39* (43), 10401-10413.
6. Cramer, S. A.; Jenkins, D. M., Synthesis of aziridines from alkenes and aryl azides with a reusable macrocyclic tetracarbene iron catalyst. *J. Am. Chem. Soc.* **2011,** *133* (48), 19342-19345.
7. Cui, Y.; He, C., Efficient Aziridination of Olefins Catalyzed by a Unique Disilver(I) Compound. *J. Am. Chem. Soc.* **2003,** *125* (52), 16202-16203.
8. Cui, Y.; He, C., A silver-catalyzed intramolecular amidation of saturated C-H bonds. *Angew. Chem. Int. Ed.* **2004,** *43* (32), 4210-4212.
9. Dauban, P.; Sanière, L.; Tarrade, A.; Dodd, R. H., Copper-catalyzed nitrogen transfer mediated by iodosylbenzene PhI=O. *J. Am. Chem. Soc.* **2001,** *123* (31), 7707-7708.
10. Dequirez, G.; Pons, V.; Dauban, P., Nitrene chemistry in organic synthesis: Still in its infancy? *Angew. Chem. Int. Ed.* **2012,** *51* (30), 7384-7395.
11. Díaz-Requejo, M. M.; Pérez, P. J., Coinage metal catalyzed C - H bond functionalization of hydrocarbons. *Chem. Rev.* **2008,** *108* (8), 3379-3394.
12. Duran, F.; Leman, L.; Ghini, A.; Burton, G.; Dauban, P.; Dodd, R. H., Intramolecular PhI=O mediated copper-catalyzed aziridination of unsaturated sulfamates: A new direct access to polysubstituted amines from simple homoallylic alcohols. *Org. Lett.* **2002,** *4* (15), 2481-2483.
13. Espino, C. G.; Du Bois, J., A Rh-catalyzed C-H insertion reaction for the oxidative conversion of carbamates to oxazolidinones. *Angew. Chem. Int. Ed.* **2001,** *40* (3), 598-600.
14. Espino, C. G.; Fiori, K. W.; Kim, M.; Du Bois, J., Expanding the scope of C-H amination through catalyst design. *J. Am. Chem. Soc.* **2004,** *126* (47), 15378-15379.
15. Fantauzzi, S.; Caselli, A.; Gallo, E., Nitrene transfer reactions mediated by metallo-porphyrin complexes. *Dalton Trans.* **2009,** (28), 5434-5443.
16. Fiori, K. W.; Du Bois, J., Catalytic intermolecular amination of C-H bonds: Method development and mechanistic insights. *J. Am. Chem. Soc.* **2007,** *129* (3), 562-568.

17. Fructos, M. R.; Trofimenko, S.; Mar Díaz-Requejo, M.; Pérez, P. J., Facile amine formation by intermolecular catalytic amidation of carbon-hydrogen bonds. *J. Am. Chem. Soc.* **2006,** *128* (36), 11784-11791.
18. Gómez-Emeterio, B. P.; Urbano, J.; Díaz-Requejo, M. M.; Pérez, P. J., Easy alkane catalytic functionalization. *Organometallics* **2008,** *27* (16), 4126-4130.
19. Halfen, J. A., Recent advances in metal-mediated carbon-nitrogen bond formation reactions: Aziridination and amidation. *Curr. Org. Chem.* **2005,** *9* (7), 657-669.
20. Harvey, M. E.; Musaev, D. G.; Du Bois, J., A diruthenium catalyst for selective, intramolecular allylic C-H amination: Reaction development and mechanistic insight gained through experiment and theory. *J. Am. Chem. Soc.* **2011,** *133* (43), 17207-17216.
21. Hennessy, E. T.; Liu, R. Y.; Iovan, D. A.; Duncan, R. A.; Betley, T. A., Iron-mediated intermolecular N-group transfer chemistry with olefinic substrates. *Chem. Sci.* **2014,** *5* (4), 1526-1532.
22. Lebel, H.; Lectard, S.; Parmentier, M., Copper-catalyzed alkene aziridination with N-tosyloxycarbamates. *Org. Lett.* **2007,** *9* (23), 4797-4800.
23. Lebel, H.; Spitz, C.; Leogane, O.; Trudel, C.; Parmentier, M., Stereoselective rhodium-catalyzed amination of alkenes. *Org. Lett.* **2011,** *13* (20), 5460-5463.
24. Lescot, C.; Darses, B.; Collet, F.; Retailleau, P.; Dauban, P., Intermolecular C-H amination of complex molecules: Insights into the factors governing the selectivity. *J. Org. Chem.* **2012,** *77* (17), 7232-7240.
25. Li, Z.; Capretto, D. A.; Rahaman, R.; He, C., Silver-catalyzed intermolecular amination of C-H groups. *Angew. Chem. Int. Ed.* **2007,** *46* (27), 5184-5186.
26. Li, Z.; He, C., Recent advances in silver-catalyzed nitrene, carbene, and silylene-transfer reactions. *Eur. J. Org. Chem.* **2006,** (19), 4313-4322.
27. Liang, C.; Robert-Peillard, F.; Fruit, C.; Müller, P.; Dodd, R. H.; Dauban, P., Efficient diastereoselective intermolecular rhodium-catalyzed C-H amination. *Angew. Chem. Int. Ed.* **2006,** *45* (28), 4641-4644.
28. Llaveria, J.; Beltrán, A.; Sameera, W. M. C.; Locati, A.; Díaz-Requejo, M. M.; Matheu, M. I.; Castillón, S.; Maseras, F.; Pérez, P. J., Chemo-, regio-, and stereoselective silver-catalyzed aziridination of dienes: Scope, mechanistic studies, and ring-opening reactions. *J. Am. Chem. Soc.* **2014,** *136* (14), 5342-5350.
29. Lu, H.; Subbarayan, V.; Tao, J.; Zhang, X. P., Cobalt(II)-catalyzed intermolecular benzylic C-H amination with 2,2,2-trichloroethoxycarbonyl azide ($TrocN_3$). *Organometallics* **2010,** *29* (2), 389-393.
30. Lu, H.; Zhang, X. P., Catalytic C-H functionalization by metalloporphyrins: Recent developments and future directions. *Chem. Soc. Rev.* **2011,** *40* (4), 1899-1909.
31. Maestre, L.; Sameera, W. M. C.; Díaz-Requejo, M. M.; Maseras, F.; Pérez, P. J., A general mechanism for the copper- and silver-catalyzed olefin aziridination reactions: Concomitant involvement of the singlet and triplet pathways. *J. Am. Chem. Soc.* **2013,** *135* (4), 1338-1348.
32. Müller, P.; Fruit, C., Enantioselective catalytic aziridinations and asymmetric nitrene insertions into CH bonds. *Chem. Rev.* **2003,** *103* (8), 2905-2919.
33. Nakanishi, M.; Salit, A. F.; Bolm, C., Iron-catalyzed aziridination reactions. *Adv. Synth. Catal.* **2008,** *350* (11-12), 1835-1840.
34. Paradine, S. M.; Griffin, J. R.; Zhao, J.; Petronico, A. L.; Miller, S. M.; Christina White, M., A manganese catalyst for highly reactive yet chemoselective intramolecular $C(sp^3)$-H amination. *Nat. Chem.* **2015,** *7* (12), 987-994.

35. Paradine, S. M.; White, M. C., Iron-catalyzed intramolecular allylic C-H amination. *J. Am. Chem. Soc.* **2012,** *134* (4), 2036-2039.
36. Roizen, J. L.; Harvey, M. E.; Bois, J. D., Metal-catalyzed nitrogen-atom transfer methods for the oxidation of aliphatic C-H bonds. *Acc. Chem. Res.* **2012,** *45* (6), 911-922.
37. Ruppel, J. V.; Kamble, R. M.; Zhang, X. P., Cobalt-catalyzed intramolecular C-H amination with arylsulfonyl azides. *Org. Lett.* **2007,** *9* (23), 4889-4892.
38. Srivastava, R. S.; Tarver, N. R.; Nicholas, K. M., Mechanistic studies of copper(I)-catalyzed allylic amination. *J. Am. Chem. Soc.* **2007,** *129* (49), 15250-15258.
39. Yang, M.; Su, B.; Wang, Y.; Chen, K.; Jiang, X.; Zhang, Y. F.; Zhang, X. S.; Chen, G.; Cheng, Y.; Cao, Z.; Guo, Q. Y.; Wang, L.; Shi, Z. J., Silver-catalysed direct amination of unactivated C-H bonds of functionalized molecules. *Nature Communications* **2014,** *5*.
40. Zalatan, D. N.; Du Bois, J., A chiral rhodium carboxamidate catalyst for enantioselective C-H amination. *J. Am. Chem. Soc.* **2008,** *130* (29), 9220-9221.
41. Zalatan, D. N.; Du Bois, J., Metal-catalyzed oxidations of C-H to C-N bonds. *Top. Curr. Chem.* **2010,** *292*, 347-378.
42. Zheng, Q. Z.; Jiao, N., Ag-catalyzed C-H/C-C bond functionalization. *Chem. Soc. Rev.* **2016,** *45* (16), 4590-4627.
43. Davies, H. M.; Dick, A. R., Functionalization of carbon-hydrogen bonds through transition metal carbenoid insertion. *Top. Curr. Chem.* **2010,** *292*, 303-345.
44. Davies, H. M. L.; Beckwith, R. E. J., Catalytic enantioselective C-H activation by means of metal-carbenoid-induced C-H insertion. *Chem. Rev.* **2003,** *103* (8), 2861-2903.
45. Doyle, M. P.; Duffy, R.; Ratnikov, M.; Zhou, L., Catalytic carbene insertion into C-H bonds. *Chem. Rev.* **2010,** *110* (2), 704-724.
46. Doyle, M. P.; Phillips, I. M., Cyclopropanation versus carbon-hydrogen insertion. The influences of substrate and catalyst on selectivity. *Tetrahedron Lett.* **2001,** *42* (18), 3155-3158.
47. Padwa, A.; Austin, D. J.; Price, A. T.; Semones, M. A.; Doyle, M. P.; Protopopova, M. N.; Winchester, W. R.; Tran, A., Ligand Effects on Dirhodium(II) Carbene Reactivities. Highly Effective Switching between Competitive Carbenoid Transformations. *J. Am. Chem. Soc.* **1993,** *115* (19), 8669-8680.
48. Liang, C.; Collet, F.; Robert-Peillard, F.; Müller, P.; Dodd, R. H.; Dauban, P., Toward a synthetically useful stereoselective C-H amination of hydrocarbons. *J. Am. Chem. Soc.* **2008,** *130* (1), 343-350.
49. Karlin, K. D., *Progress in Inorganic Chemistry*. John Wiley&Sons, Inc.: Hoboken, NJ: 2014; Vol. 58, p 225-302.
50. Kornecki, K. P.; Berry, J. F., Evidence for a one-electron mechanistic regime in dirhodium-catalyzed intermolecular C-H amination. *Chem. Eur. J.* **2011,** *17* (21), 5827-5832.
51. Kornecki, K. P.; Berry, J. F., Dirhodium catalysts that bear redox noninnocent chelating dicarboxylate ligands and their performance in intra-and intermolecular C-H amination. *Eur. J. Inorg. Chem.* **2012,** (3), 562-568.
52. Kornecki, K. P.; Berry, J. F., Introducing a mixed-valent dirhodium(ii,iii) catalyst with increased stability in C-H amination. *Chem. Commun.* **2012,** *48* (99), 12097-12099.
53. Alderson, J. M.; Phelps, A. M.; Scamp, R. J.; Dolan, N. S.; Schomaker, J. M., Ligand-controlled, tunable silver-catalyzed C-H amination. *J. Am. Chem. Soc.* **2014,** *136* (48), 16720-16723.
54. Rigoli, J. W.; Weatherly, C. D.; Alderson, J. M.; Vo, B. T.; Schomaker, J. M., Tunable, chemoselective amination via silver catalysis. *J. Am. Chem. Soc.* **2013,** *135* (46), 17238-17241.

55. Scamp, R. J.; Jirak, J. G.; Dolan, N. S.; Guzei, I. A.; Schomaker, J. M., A General Catalyst for Site-Selective C(sp^3)-H Bond Amination of Activated Secondary over Tertiary Alkyl C(sp^3)-H Bonds. *Org. Lett.* **2016,** *18* (12), 3014-3017.
56. Williams, N. J.; Gan, W.; Reibenspies, J. H.; Hancock, R. D., Possible steric control of the relative strength of chelation enhanced fluorescence for zinc(II) compared to cadmium(II): Metal ion complexing properties of tris(2-quinolylmethyl)amine, a crystallographic, UV-visible, and fluorometric study. *Inorg. Chem.* **2009,** *48* (4), 1407-1415.
57. Li, D. R.; Xia, W. J.; Tu, Y. Q.; Zhang, F. M.; Shi, L., A novel $AlEt_3$-promoted tandem reductive rearrangement of 1-benzyloxy-2,3-epoxides: New route to 2-quaternary 1,3-diol units. *Chem. Commun.* **2003,** *9* (6), 798-799.
58. Li, X.; Wu, B.; Zhao, X. Z.; Jia, Y. X.; Tu, Y. Q.; Li, D. R., An interesting $AlEt_3$-promoted stereoselective tandem rearrangement/reduction of α-hydroxy (or amino) heterocyclopropane. *Synlett* **2003,** (5), 623-626.
59. Varela-Álvarez, A.; Yang, T.; Jennings, H.; Kornecki, K. P.; Macmillan, S. N.; Lancaster, K. M.; Mack, J. B. C.; Du Bois, J.; Berry, J. F.; Musaev, D. G., Rh_2(II,III) Catalysts with Chelating Carboxylate and Carboxamidate Supports: Electronic Structure and Nitrene Transfer Reactivity. *J. Am. Chem. Soc.* **2016,** *138* (7), 2327-2341.
60. Besora, M.; Braga, A. A. C.; Sameera, W. M. C.; Urbano, J.; Fructos, M. R.; Pérez, P. J.; Maseras, F., A computational view on the reactions of hydrocarbons with coinage metal complexes. *J. Organomet. Chem.* **2015,** *784*, 2-12.
61. Blanksby, S. J.; Ellison, G. B., Bond dissociation energies of organic molecules. *Acc. Chem. Res.* **2003,** *36* (4), 255-263.
62. Luo, Y. R., *Comprehensive Handbook of Chemical Bond Energies*. CRC Press: Boca Raton, FL: 2007.

4 Numerical Nuclear Second Derivatives on a Computing Grid: Enabling and Accelerating Frequency Calculations on Complex Molecular Systems

This chapter has been submitted:

Yang, T.;* Berry, J. F.*

Department of Chemistry, University of Wisconsin—Madison, Madison, Wisconsin 53706, USA

4.1 Abstract

The computation of nuclear second derivatives of energy, or the nuclear Hessian, is an essential routine in quantum chemical investigations of ground and transition states, thermodynamic calculations, and molecular vibrations. Analytic nuclear Hessian computations require the resolution of costly coupled-perturbed self-consistent field (CP-SCF) equations while numerical differentiation of analytic first derivatives has an unfavorable 6N (N = number of atoms) prefactor. Herein, we present a new method in which grid computing is used to accelerate and/or enable the evaluation of the nuclear Hessian via numerical differentiation: NUMFREQ@Grid. Nuclear Hessians were successfully evaluated by NUMFREQ@Grid at the DFT level as well as using RIJCOSX-ZORA-MP2 or RIJCOSX-ZORA-B2PLYP for a set of linear polyacenes with systematically increasing size. For the larger members of this group, NUMFREQ@Grid was found to outperform the wall clock time of analytic Hessian evaluation; at the MP2 or B2LYP levels, these Hessians cannot even be evaluated analytically. We also evaluated a 156-atom catalytically relevant open-shell transition metal complex, and found that NUMFREQ@Grid is faster (7.7 times shorter wall clock time) and less demanding (4.4 times less memory requirement) than an analytic Hessian. Capitalizing on the capabilities of parallel grid computing, NUMFREQ@Grid can

outperform analytic methods in terms of wall time, memory requirements, and treatable system size. The NUMFREQ@Grid method presented herein demonstrates how grid computing can be used to facilitate embarrassingly parallel (also referred to as pleasantly parallel) computational procedures and is a pioneer for future implementations.

4.2 Introduction

The computation of second derivatives of the energy with respect to nuclear displacements χ and ζ, or the nuclear Hessian, is an essential task in quantum chemical investigations for validating the curvature of potential energy surfaces at critical points, calculating or predicting vibrational spectroscopic features of molecules, and evaluating partition functions. The formulation of analytic methods to calculate the Hessian for SCF wavefunctions was reported in 1958[1] followed by another formulation based on the Hellmann-Feynman theorem in 1968.[1-3] However, practical formulation of the SCF analytic Hessian based on molecular orbitals (MO) was not presented until 1979[4] due to the high demand on memory and disk storage required for calculation of an analytic Hessian. The analytic Hessian for wavefunction methods that include dynamic electron correlation was later derived, e.g., MP2,[5-6] CI,[7-8] CCSD,[9] and CCSD(T),[10] and for those that include static electron correlation, such as MCSCF.[11] Following the development of Density Functional Theory (DFT),[12-16] the analytic Hessian based on DFT was also developed.[17] Detailed reviews on the development of the analytic Hessian for various theoretical methods can be found in the literature.[18-22]

The computation of the analytic Hessian requires the resolution of CP-SCF equations, and exerts high demands on CPU and storage due to the asymptotic cubic order scaling of these equations with respect to the number of atom-centered basis functions, i.e. $O(N_{basis}^3)$, and $O(N_{basis}^4)$ scaling of input and output (I/O),[23] rendering the application of analytic Hessians to large molecules intractable. To reduce the steep scaling of the CP-SCF equations, recent work seeks to streamline evaluation of the two-electron integrals by taking advantage of the fast decay of basis functions (e.g. the continuous fast-multipole expansion,[24] the chain-of-sphere approximation[25]) and function expansion of basis functions (e.g. the resolution of the

identity,[26-27] occupied orbital RI-K,[28] J matrix engine,[29] pseudospectral[30]) to enable Hessian evaluations for large systems. Detailed comparisons of these approximations can be found in the literature.[31-33]

It was noted by Almlof and coworkers in 1982 that development of central processing units (CPU) had allowed faster evaluations of integrals while the storage of these integrals exerted a high demand on the disk space, causing an I/O bottleneck. Hence, they proposed the integral handling method "direct SCF", in which integrals from trial density matrices are recalculated for every SCF cycle resulting in a longer computing time in exchange for less temporary disk file storage enabling integral evaluations for larger molecules.[34] Based on the philosophy of direct SCF, Ahlrichs and coworkers suggested a combined integral handling, "semi-direct", which selectively stores costly integral batches (i.e. integral batches formed by higher angular momentum bases) and reduces the amount of recalculations by minimizing the difference between the previous and the new trial density matrices.[35] Multiprocessor computers, such as high performance clusters (HPC), have allowed parallel computations of direct SCF[36-40] and direct CP-SCF[41-42] equations over multiple CPUs. Parallel computations based on semi-direct SCF were also developed.[43] Parallel implementation of post SCF methods has been developed as well.[44-46] The emergence of specialized computer hardware such as graphics processing units (GPU) has allowed quantum chemistry to achieve even faster and more capable parallel SCF[47-51] and post SCF [52-56] calculations. However, there are no implementations of CP-SCF on GPU architectures to our knowledge.

Despite ongoing theoretical efforts in approximating two-electron integrals and computing efforts in improving memory/storage management and parallelization of computations, the resolution of $3N-6(5)$ CP-SCF equations is still the most time consuming step in the computation of analytic Hessians.[42] It was suggested by Pulay in 1969 that numerical differentiation of analytic first derivatives (analytic gradients), or semi-numerical Hessian evaluation, provides a strategy to bypass the resolution of CP-SCF equations.[57] Numerical differentiation truncated at the first order is evaluated via

$$E^{\chi\zeta}(q_i) \approx \frac{E^{\chi}(\zeta_i + h, \dots, \zeta_{3N}) - E^{\chi}(\zeta_i - h, \dots, \zeta_{3N})}{2h} \tag{1}$$

where h is the step size.

Circumventing the resolution of the costly CP-SCF equations reduces the memory and disk demand on the processor, allowing Hessian evaluations to be performed for larger system sizes. However, the pre-scaling factor of semi-numerical Hessians presents another challenge for conventional HPCs due to the fact that a molecule with N atoms will require 3N (forward or backward) or 6N (central difference) independent evaluations of the analytic forces, resulting in one order of magnitude higher scaling than the calculation of analytic forces.

To remedy the unfavorable prefactor of the semi-numerical Hessian, we exploit here recent developments in computing hardware, optical fibers, the Internet, and protocols for internetwork communication. Computing grids have arisen from these tools as a new form of computing infrastructure taking advantage of the curation of computer clusters at most academic institutions. Grid computing consists of a collection of distributed computing resources that are geographically disperse[58] yet allows users to access thousands of nodes across the globe. However, due to the decentralized nature of the network, less communication among nodes can be achieved than on a conventional HPC. This fact renders parallel computations that demand frequent communication and file sharing among nodes slower despite the increased amount of CPU hours available. On the other hand, calculations that are embarrassingly parallel (a feature of numerical differentiations such as the semi-numerical Hessian) can benefit greatly from grid computing. In this article, we present our new approach to performing semi-numerical Hessian calculations on a grid platform: NUMFREQ@Grid. The advantage of NUMFREQ@Grid compared to the conventional numerical Hessian is that the scaling of NUMFREQ@Grid is simply that of analytic gradients because the 6N prefactor of the central differentiation is eliminated by concurrently running all 6N calculations across the computing grid. We describe its implementation using the computing grid Open Science Grid (OSG),[59-60] including issues with and a solution to hardware inhomogeneity associated with the computing grid. At the level of DFT, the performance of NUMFREQ@Grid compared to the analytic Hessian is benchmarked to a series of polyacenes with a systematic increase in molecule size and is found to excel for larger catalytically relevant transition metal containing complexes. The efficiency of NUMFREQ@Grid in terms of CPU and wall time and memory for RIJCOSX-MP2 is also investigated.

4.3 Implementation

4.3.1 The workflow of NUMFREQ@Grid.

To implement NUMFREQ@Grid, we take advantage of one of the available computing grids in the United States, OSG. OSG allows users to access computing resources at other organizations through the protocols Globus and the job batch system HTCondor, in the form of HTCondor-G.[61] HTCondor-G allows users to easily bring their software packages and input commands to external locations, and allows for straightforward management of jobs using the HTCondor utility Direct Acyclic Graph Manager (DAGMan), which allows the execution of jobs with declared dependencies.[62] This latter feature is essential for NUMFREQ@Grid because of the stringent fault tolerance of numerical differentiation—any error in one of the analytic gradients results in artifacts in the calculated Hessian—and because the numerical differentiation can only be performed after all the analytic gradients are complete.

DAGMan provides a mechanism for job preparation (PRE SCRIPT), execution (JOB), monitoring and processing (POST SCRIPT), retry (RETRY), and child job execution (CHILD; for example, if thermodynamic parameters are to be calculated based on the Hessian). We therefore utilize these functions of DAGMan to (i) generate perturbed coordinates ($\zeta_i \pm h, \dots \zeta_{3N}$) based on an N-atom initial coordinate ($\zeta_i, \dots, \zeta_{3N}$) and a given increment of perturbation (h), (ii) submit concurrently duplicates of all $6N$ analytic gradient calculations based on the perturbed coordinates, (iii) verify convergence of the analytic gradients and (iv) retry if not converged and remove duplicates after the first in the duplicate set is complete, (v) differentiate each pair of analytic gradients numerically using eq. 1 to produce the Hessian vector, and (vi) assemble all $3N$ Hessian vectors into the Hessian matrix (Scheme 4.1).

Scheme 4.1. Workflow of NUMFREQ@Grid. All the arrows are controlled by the DAGMan utility. (i) A PRE SCRIPT is used to generate perturbed geometries based on a given initial geometry, (ii) each perturbed geometry is submitted as a JOB to the OSG to compute the analytic gradient (i.e. eq. 12), (iii) a POST SCRIPT checks the convergence of the computation after each completion of a JOB, (iv) RETRY is demanded if convergence was not detected in (iii), and (v) a *P*OST SCRIPT to numerically differentiate E^{χ} at the first order (eq. 13) and (vi) assemble each numerically differentiated $E^{\chi}(q_i)$ to give the Hessian matrix.

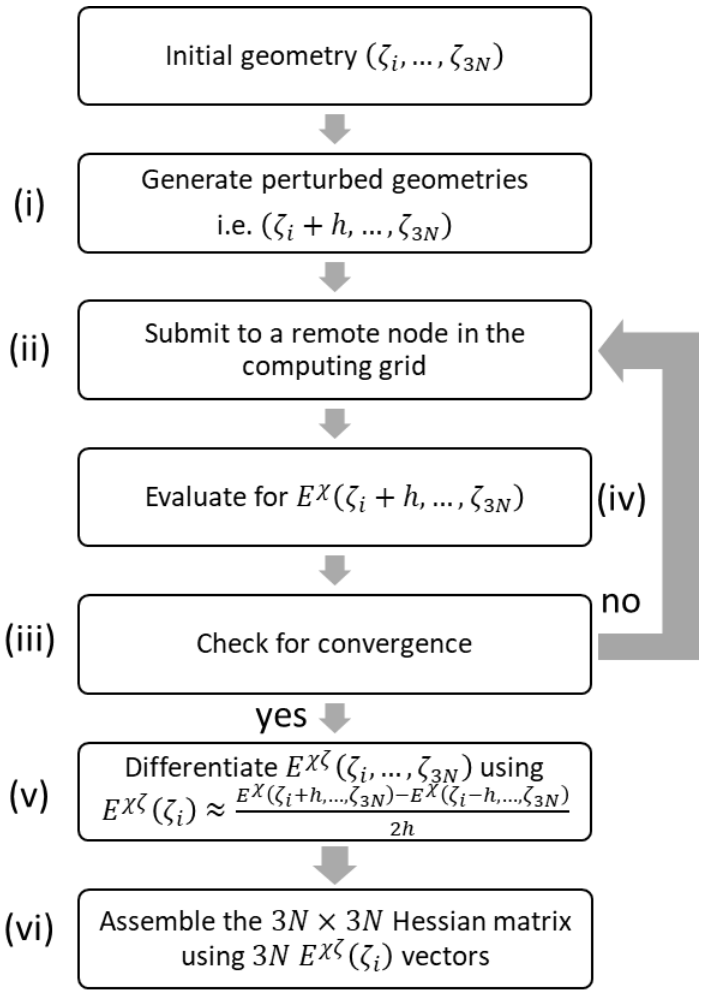

4.3.2 Effect of the size of finite displacements used for NUMFREQ@Grid on the accuracy of Hessian

The NUMFREQ@Grid method takes advantage of the lower memory and disk requirement of numerical differentiation to enable and/or accelerate Hessian evaluation using expensive theoretical methods and of the high scalability of computing grids to mitigate the unfavorable $6N$ prefactor associated with central differences to accelerate Hessian evaluations using less expensive theoretical methods. However, numerical methods are approximate to analytic methods and the size of the finite displacements (h) used in numerical differentiations can have various impacts on the resulting Hessian, i.e. too small a displacement leads to large numerical error while too large a displacement introduces contaminations from higher order derivatives, which is mitigated by

central differences.[19] This issue was previously investigated and a step size of 0.005 Bohr yields surprisingly accurate and robust harmonic vibrational frequencies as compared to the analytic Hessian for various molecules.[63] Nonetheless, we investigate here the error introduced by various sizes of *h* used in semi-numerical Hessian calculations on the calculated harmonic vibrational frequencies of C_6H_6 using RIJCOSX-ZORA-B3LYP (*vida infra* for computational details).

Table 4.1. The effect of the size of finite displacements[a] used in NUMFREQ@Grid on the calculated harmonic vibrational frequencies of C_6H_6

analytic Hessian[b]	**NUMFREQ@Grid[c]**			
	0.0025	**0.005**	**0.01**	**0.02**
413.970 (e_{2u})	413.150 (0.20)	416.970 (0.73)	413.900 (0.02)	412.68 (0.31)
414.060 (e_{2u})	415.250 (0.29)	419.060 (1.20)	415.280 (0.29)	414.77 (0.17)
620.680 (e_{2g})	618.700 (0.32)	619.420 (0.20)	620.050 (0.10)	619.97 (0.11)
620.760 (e_{2g})	619.560 (0.19)	620.800 (0.01)	620.720 (0.01)	620.61 (0.02)
683.160 (a_{2u})	685.330 (0.32)	685.880 (0.40)	686.390 (0.47)	684.14 (0.14)
RMSD[d]	1.53	0.83	0.91	0.63
MAD[e]	3.60	2.07	2.25	1.46

[a]The sizes of finite displacements are reported in the unit of Bohr. [b]Irreducible representation of the vibrations are shown in parentheses. [c]Numbers enclosed in parentheses are absolute percentage deviation (%AD) from the values obtained using analytic Hessian. [d]RMSD = root-mean-square deviation, cm^{-1}. [e]MAD = maximum absolute deviation, cm^{-1}.

Four values of *h* are investigated, 0.0025. 0.005, 0.01, and 0.02 Bohr, and the calculated frequencies can be found in the Supplementary Information. We show the five lowest energy vibrations of C_6H_6 calculated using either an analytic Hessian or NUMFREQ@Grid. The absolute percent deviation (%AD) of NUMFREQ@Grid from the analytic Hessian of these five vibrations, the root-mean-square deviations (RMSD), and maximum absolute deviations (MAD) derived from

all the vibrations are given in Table 4.1. The vibration with the largest %AD, 0.73 %, among the four in Table 4.1 has a frequency of 416.970 cm^{-1}, corresponding to the torsional vibration along an in-plane axis bisecting a pair of C–C bonds. Among the four finite displacements employed, 0.02 Bohr yielded the largest %AD for this vibration. When all vibrations are considered, 0.02 Bohr yields the lowest RMSD and MAD with 0.005 Bohr second in both criteria. As numerical differentiations are sensitive to the size of finite displacements and large finite displacements are known to introduce contaminations from higher order derivatives,[19] results using 0.005 Bohr for NUMFREQ@Grid are reported in the remaining text. Results using 0.0025, 0.01, and 0.02 Bohr for the studies in this work can be found in the Supporting Information.

4.3.3 Effect of grid inhomogeneity on wall time.

Grid computing suffers from computer hardware inhomogeneity, which reduces the efficiency of NUMFREQ@Grid since *all* aNFS evaluations for a given set of coordinates have to finish before numerical differentiation can be performed to generate the Hessian matrix. Because of the opportunistic nature of grid computing, users have marginal control over the computer hardware on which their computing jobs are being executed. This issue causes the completion time of NUMFREQ@Grid to fluctuate substantially for replicates of any given calculation. To investigate how the fluctuation in wall time affects NUMFREQ@Grid, we performed NUMFREQ@Grid on C_6H_6 five times and the wall time of all the analytic gradients in each replicate is shown on the left in Figure 4.1. Because there are multiple computations of analytic gradients for each NUMFREQ@Grid, the wall times for all these calculations are shown in percentile bars with the thicker portion representing the mid-range 25–75% timings. It can be seen that 75% of all the analytic gradients for C_6H_6 finished within 100 seconds after execution. However, the whole NUMFREQ@Grid computation can take up to almost double the time of the 75^{th} percentile due to the variation in hardware on the computing grid. In addition, the variation in the total wall time (the 100^{th} percentile) of the six replicates varies by 33%.

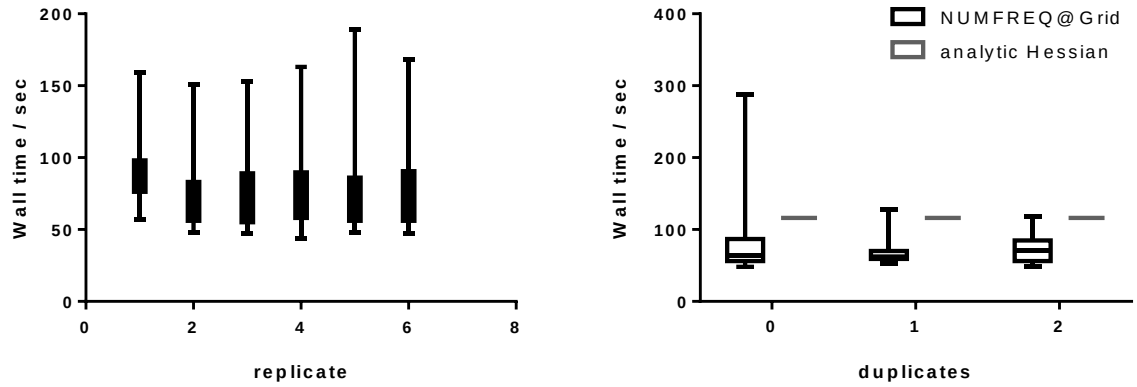

Figure 4.1. Variation in the wall time within each set of analytic gradients and among replicates of NUMFREQ@Grid on C_6H_6 (left) and the wall time performance of NUMFREQ@Grid on C_6H_6 using duplicates of submissions (right)

4.3.4 Mitigation of grid inhomogeneity with duplicate submissions

Inhomogeneity of the computing grid causes a skewed distribution of wall times within a set of analytic gradients for one NUMFREQ@Grid calculation, delaying the completion of the NUMFREQ@Grid calculation. As seen on the right in Figure 4.1, the NUMFREQ@Grid calculation on C_6H_6 without duplicates has 75% of the analytic gradient calculations finished within 100 seconds, consistent with those in the left figure. However, the inhomogeneity of the computer hardware in the OSG becomes clear upon analysis of the two slowest analytic gradient calculations, which finished after 288 seconds and 189 seconds, respectively. These outliers are uncontrollable, as one can observe in Figure 4.1 that the tail of the skewed distribution of the wall time of NUMFREQ@Grid calculation on C_6H_6 without duplicates can vary significantly.

To mitigate this inherent issue of grid computing, we take advantage of the high throughput aspect of the cyberinfrastructure. The probability of two identical submissions finishing at the same time in the computing grid is almost negligible; one calculation almost always finishes earlier than the other. Hence, we may submit duplicates of each analytic gradient calculation to remedy the delay due to hardware heterogeneity of the computing grid.The results of the distribution of wall time of NUMFREQ@Grid on C_6H_6 using one and two duplicates as compared to that without any duplicates are shown on the right in Figure 4.1. It can be seen that the completion time is reduced by a factor of two by using one duplicate of

NUMFREQ@Grid, making the time performance of NUMFREQ@Grid comparable to that of an analytic Hessian. Including two duplicates only marginally improves the wall time for NUMFREQ@Grid compared to that using one duplicate. To reduce the amount of computing resources wasted in computing duplicates of the individual analytic gradients, we utilized the POST SCRIPT function in DAGMan to remove the slow duplicate executions on-the-fly once one analytic gradient calculation is complete in a set of duplicates.

4.4 Computational Details

To implement and test the NUMFREQ@Grid method with the OSG, unless specified otherwise, we used the hybrid generalized gradient approximation (hGGA) functional B3LYP[64-65] (note that the LDA component of B3LYP employed in this study uses was VWN-5) under the zeroth order regular approximation for scalar relativistic corrections (ZORA)[66] using the one-center approximation with the resolution of the identity and the chain-of-sphere approximations (RIJCOSX-ZORA-B3LYP) with the recontracted def2-SVP basis set, ZORA-def2-SVP (recontracted def2-TZVPP, ZORA-def2-TZVPP was employed on transition metals)[67-68] and the corresponding density fitting basis set[69-70] on C_6H_6 (186 primitive Gaussian functions (GFs) contracted to 114 basis functions (BF) and 516 primitive Gaussian basis sets for density fitting (DFGFs) contracted to 360 aux-basis functions (ABF)), $C_{10}H_8$ (296 GFs contracted to 180 BFs and 828 DFGFs contracted to 578 ABFs), $C_{14}H_{10}$ (406 GFs contracted to 246 BFs and 1140 DFGFs contracted to 796 ABFs), $C_{18}H_{12}$ (516 GFs contracted to 314 BFs and 1452 DFGFs contracted to 1014 ABFs), $C_{22}H_{14}$ (626 GFs contracted to 378 BFs and 1764 DFGFs contracted to 1232 ABFs), $C_{26}H_{16}$ (736 GFs contracted to 444 BFs and 2076 DFGFs contracted to 1450 ABFs), and $C_{30}H_{18}$ (846 GFs contracted to 510 BFs and 2388 DFGFs contracted to 1668 ABFs). The contractions are as following: H, 4s1p to 2s1p {31/1}; C, N, O, F, 7s4p1d to 3s2p1d {511/31/1}; S, 10s7p1d to 6s3p1d {511111/511/1}; and Ag, 19s14p9d1f to 12s9p5d1f {811111111111/611111111/51111/1}. Step sizes of 0.0025, 0.005, 0.01, and 0.02 Bohr are used for the numerical differentiation (except for RIJCOSX-ZORA-MP2/def2-TZVPP where only 0.005 Bohr was used for step size for computational convenience). Results using 0.005 Bohr are

reported in the article. Results using the other step sizes can be found in the Supporting Information. The geometries of the polyacenes tested in this article were optimized using same methods. The geometry of the silver-nitrene complex was obtained from the literature.[71] To apply NUMFREQ@Grid to RIJCOSX-ZORA-MP2 and RIJCOSX-ZORA-B2PLYP methods, the same basis sets were employed and no frozen core was applied. All calculations except RIJCOSX-ZORA-B2PLYP[72] calculations (Orca 4.0.0[73] was used instead) were performed with the Orca 3.0.3 program package[74] for its compatibility with various types of computer platforms in the computing grid. For each analytic gradient calculation in one NUMFREQ@Grid calculation, we used *one core per job*. For analytic Hessians performed on our HPC, we used *twelve cores per job*. For comparing the time performance of NUMFREQ@Grid to analytic Hessians, wall time is therefore more useful than comparing CPU time.

4.5 Applications

4.5.1 Accelerating DFT calculation of nuclear Hessians using NUMFREQ@Grid

Hessian matrices for a set of linear polyacenes were computed using either NUMFREQ@Grid or an analytic Hessian. The wall time for either method is shown on the right in Figure 4.2. It can be found that NUMFREQ@Grid outcompetes the analytic Hessian in terms of wall time as the number of polyacenes becomes larger than three.

DFT calculations of vibrational frequencies are commonly employed to assist the assignment of experimental vibrational spectra. The errors associated with the numerical differentiation of DFT analytic forces are assessed against their analytic Hessian counterparts and the result is shown on the left in Figure 4.2. It can be found that the root-mean-square deviations (RMSDs) of the harmonic vibrational frequencies calculated using NUMFREQ@Grid are within 1 cm^{-1} from those calculated using analytic Hessian. The maximum absolute deviations (MADs) from NUMFREQ@Grid calculations are around 2 cm^{-1} except for hexacene, where the MAD is about 3.5 cm^{-1}. Furthermore, the error associated with the numerical differentiation is significantly smaller than the error compared to experimental vibrations. For example, an

RMSE of 65.4 cm^{-1} and MAD of 142 cm^{-1} are found when analytic frequencies are compared to experimental values for C_6H_6.[75] [76]Thus, numeric frequencies calculated using NUMFREQ@Grid are of comparable utility to analytic frequencies for interpreting experimental vibrational spectra.

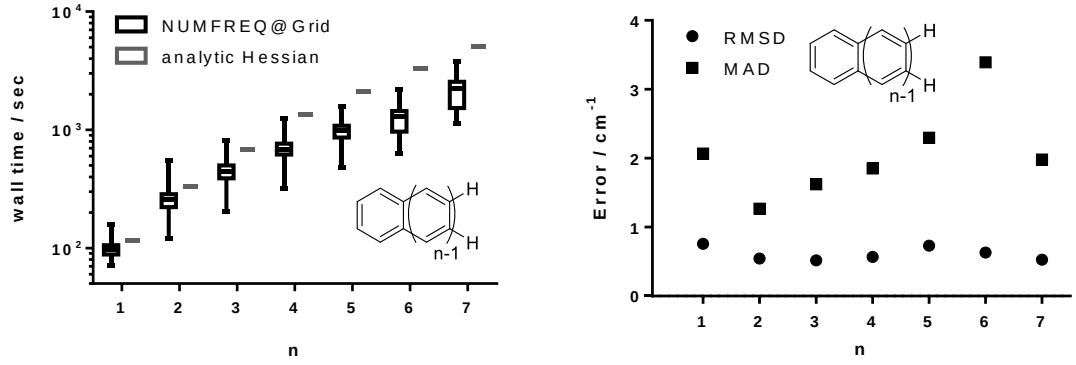

Figure 4.2. Wall time (left) and error (right; RMSD and MAD) for linear polyacene molecules performed by NUMFREQ@Grid versus analytic Hessian.

4.5.2 Enabling Hessian evaluation using theoretical methods that are prohibitively expensive for large molecules by NUMFREQ@Grid

4.5.2.1 Hessian evaluation using RIJCOSX-ZORA-MP2/def2-SVP for linear polyacenes

Analytic Hessian calculations using canonical MP2 scale formally as $O(N_{basis}^6)$.[5-6] The steep scaling renders the analytic Hessian intractable for large molecules on a conventional HPC. In comparison, energy and gradient calculations using canonical MP2 are one order more tractable, formally scaling as $O(N_{basis}^5)$ with system size.[77] Therefore, NUMFREQ@Grid is computationally more accessible for larger molecules compared to analytic Hessians as the unfavorable $6N$ prefactor is mitigated by the grid approach. To study the wall time and memory performance of NUMFREQ@Grid *vs.* the analytic Hessian, we computed the RIJCOSX-ZORA-MP2 Hessian matrix of the seven polyacenes using NUMFREQ@Grid or an analytic Hessian and the results are shown in

Figure ***4.3***. It is evident that NUMFREQ@Grid outperforms the analytic Hessian in both

wall time and memory usage, where NUMFREQ@Grid is 8.6 times faster and 13 times less memory-intensive for C_6H_6 and 5.6 times faster and 46 times less memory-intensive for $C_{10}H_8$ than is the analytic Hessian using 12 cores. An analytic Hessian could not even be completed for larger linear polyacenes using RIJCOSX-ZORA-MP2 without further approximations.

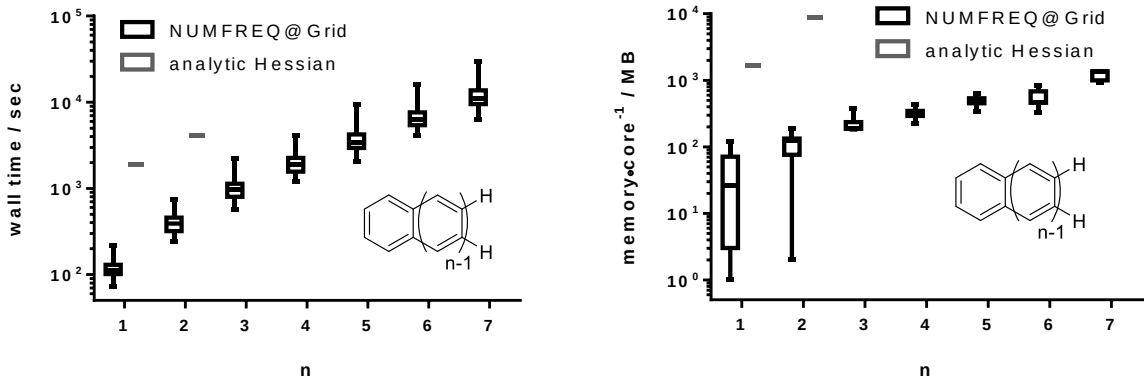

Figure 4.3. Wall time (left) and memory usage per core (right) for linear polyacenes by NUMFREQ@Grid (black percentile bars) and analytic Hessian (only tractable for C_6H_6 and $C_{10}H_8$; grey bars) using RIJCOSX-ZORA-MP2 are shown.

4.5.2.2 Hessian evaluation using RIJCOSX-ZORA-MP2/def2-TZVPP for linear polyacenes

The performance of MP2 is sensitive to the size of basis sets.[78] However, the use of large basis sets limits the applicability of MP2 to calculating frequencies for larger molecules due to the steep scaling of MP2 with respect to the size of the basis set (*vida infra*). NUMFREQ@Grid lessens this issue with MP2 as discussed above. The effect of an increase in basis set size on the calculated vibrational frequencies of C_6H_6 and $C_{10}H_8$ is shown in Table 4.2. It can be found that the numerical agreement between the calculated and the experimental frequencies improves significantly upon the increase in basis set size. Performance of B3LYP (*vida infra*) is also included for comparison. It is also worth mentioning that the increase in the basis set size also eliminates unphysical negative frequencies calculated using RIJCOSX-MP2 (see Supporting Information). This further emphasizes the need of larger basis sets for wavefunction-based

correlation methods and the strength of NUMFREQ@Grid for enabling semi-numerical nuclear Hessian evaluation using large basis set for RIJCOSX-MP2 frequencies. The wall time performance of NUMFREQ@Grid using RIJCOSX-ZORA-MP2/ZORA-def2-TZVPP compared to its smaller basis set analogue is shown in Figure 4.4 (the analytic Hessian is not tractable). The increase in wall clock time and memory requirement is below one order of magnitude.

Table 4.2. Basis set effect on the RIJCOSX-ZORA-MP2 calculated vibrational frequencies using NUMFREQ@Grid on C_6H_6, $C_{10}H_8$,and $C_{14}H_{10}$ as compared to experimental values[a]

Molecule	**Method**	**Basis set**	**RMSD[b]**	**MAD[c]**
C_6H_6	MP2	def2-SVP	95.5	194
	MP2	def2-TZVPP	45.3	92.9
	B3LYP	def2-SVP	67.0	143
$C_{10}H_8$	MP2	def2-SVP	99.9	281
	MP2	def2-TZVPP	60.6	160
	B3LYP	def2-SVP	46.8	102
$C_{14}H_{10}$	MP2	def2-SVP	90.1	200
	MP2	def2-TZVPP	35.6	81.5
	B3LYP	def2-SVP	58.9	151

[a]The sizes of finite displacement is 0.005 Bohr. See ref [75] for experimental vibrations for C_6H_6, ref [76] for $C_{10}H_8$ and ref [79] for $C_{14}H_{10}$. [b]RMSD = root-mean-square deviation, cm^{-1}. [c]MAD = maximum absolute deviation, cm^{-1}.

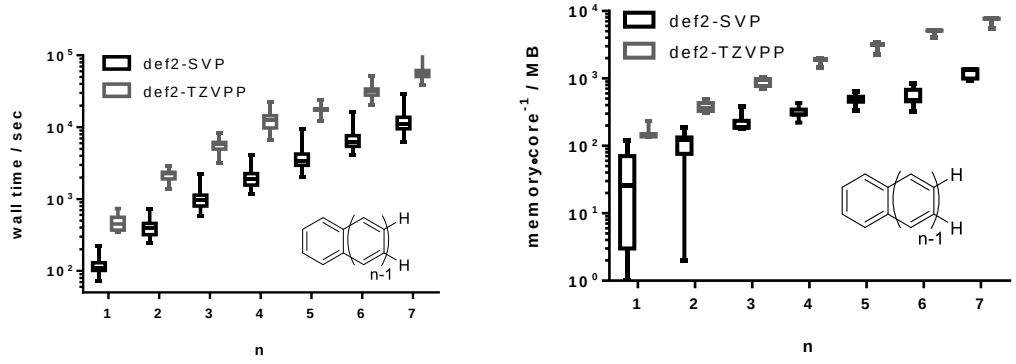

Figure 4.4. Wall time (left) and memory usage per core (right) for various molecules of linearly polyacenes by NUMFREQ@Grid using RIJCOSX-ZORA-MP2 with ZORA-def2-SVP (black percentile bars) or ZORA-def2-TZVPP (grey percentile bars) are shown.

4.5.2.3 Hessian evaluation using RIJCOSX-ZORA-B2PLYP for various numbers of polyacenes

Double hybrid density functionals (DHDFs) are an emerging rung on the Jacob's Ladder of density functionals that demonstrate improved performance, compared to the already successful hybrid DFT, for their improved recovery of nonlocal correlation energy.[80] The wall time performance of NUMFREQ@Grid using a DHDF, RIJCOSX-ZORA-B2PLYP, is shown in Figure 4.5. It can be found that RIJCOSX-ZORA-B2PLYP frequencies can easily become routine for systems as big as $C_{30}H_{18}$, finishing within 6 hours (*vida supra* for the number of GFs and DFGFs). Inspecting the distribution of total wall time among various components of the RIJCOSX-ZORA-B2PLYP analytic gradient calculation, it becomes apparent that more than 50% of the wall time was invested in preparing and solving the MP2 correction of the nonlocal exchange (Figure 4.5). Any improvement, such as parallel calculation, in the MP2 timing would significantly accelerate the wall time of NUMFREQ@Grid. However, parallel calculation of each analytic gradient calculation of NUMFREQ@Grid using more than one core in one remote computer node significantly reduces the number of available nodes in the computing grid, hence, lengthening the queue time of each analytic gradient calculation. One potential way to mitigate the time investment in the MP2 module is to partition the correlation space into small orbital fragments and distribute

each fragment to a remote node in the computing grid, transforming the MP2 amplitude calculation into an embarrassingly parallel task, further taking advantage of the high scalability of the computing grid. Future deqqvelopment of NUMFREQ@Grid to incorporate various types of fragmentation methods, such as divide-expand-consolidate,[81] is foreseeable.

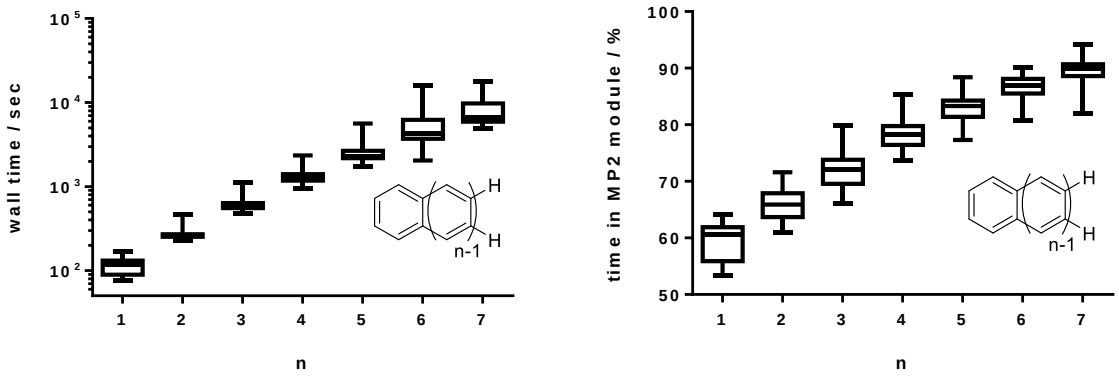

Figure 4.5. Wall time (left) and fraction of total wall time spent in the MP2 module (right) for various molecules of linearly polyacenes by NUMFREQ@Grid using RIJCOSX-ZORA-B2PLYP are shown.

4.6 A Practical Example

E-$Ag_2(^tbu_3tpy)_2OTf(NSO_3$-2,6-dFPh) ($^tbu_3$tpy = 4-,4'-,4"-tri-tert-butyl-2-,2':6'-2"-terpyridine, OTf = triflate, and dFPh = difluorophenyl), whose structure is shown in Figure 4.6, is a proposed metal-nitrene reactive intermediate in silver-catalyzed intermolecular nitrene transfer reactions with a triplet electronic ground state.[71] Such complexes are important for atom-efficient addition of nitrogen functionalities to organic molecules. With SARC-def2-TZVPP on Ag and SARC-def2-SVP on the rest of the elements adding up to 2705 primitive GFs contracted to 1653 BFs and 7094 primitive DFGFs contracted to 5018 ABFs, NUMFREQ@Grid took 181-239-257-286-483 minutes in wall time for wall time for E-$Ag_2(^tbu_3tpy)_2OTf(NSO_3$-2,6-dFPh) with 432-686-728-814-981 MB memory usage per core. In contrast, an analytic Hessian calculation completed in 3730 minutes using 12 cores and 4343 MB per core. Overall, NUMFREQ@Grid is 7.7 times faster in wall time and 4.4 times less memory intense than the analytic

Hessian using 12 cores on an open-shell molecule consisting of 156 atoms, among them two transition metal atoms.

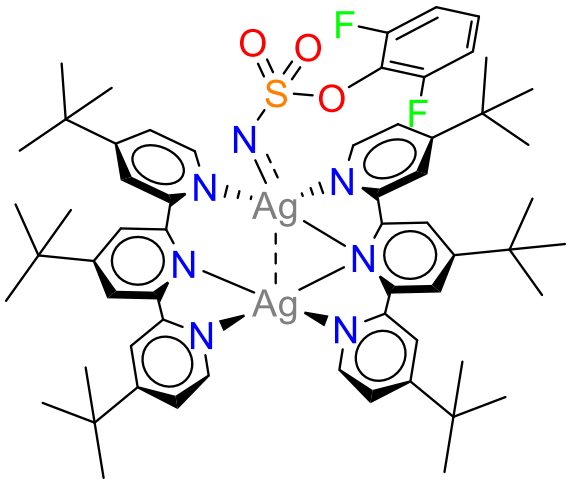

Figure 4.6. Structure of E-$Ag_2(^tbu_3tpy)_2OTf(NSO_3$-2,6-dFPh), a proposed reactive intermediate in silver-catalyzed nitrene transfer, containing 156 atoms with two heavy metals.

4.7 Conclusion and Outlook

Continuous developments in computing hardware, optical fibers, the Internet, and protocols for internetwork communication have enabled us to develop a new computing-grid-enabled semi-numerical method for computing nuclear Hessian matrices: NUMFREQ@Grid. NUMFREQ@Grid can outperform analytic Hessians in terms of wall time for B3LYP (and other similar or lower scaling density functionals) and of treatable system size using less memory for higher level computational methods. To our knowledge, the study reported herein is the first example of the utilization of grid computing to improve the applicability of nuclear Hessian computations to various chemical systems using a broad range of theoretical methods. We envision future developments of computing-grid-enabled quantum chemical methods, especially for methods that are embarrassingly parallel that can readily be adapted to grid computing.

4.8 Acknowledgments

J.F.B. thanks the Center for Selective C−H Functionalization supported by the National Science Foundation (CHE-1700982). The computational facility at Madison is supported in part by National Science Foundation Grant CHE-0840494 and at the UW—Madison Center for High Throughput Computing (CHTC) in the Department of Computer Sciences. The CHTC is supported by UW—Madison, the Advanced Computing Initiative, the Wisconsin Alumni Research Foundation, the Wisconsin Institutes for Discovery, and the National Science Foundation, and is an active member of the Open Science Grid, which is supported by the National Science Foundation award 1148698 and the U.S. Department of Energy's Office of Science.

4.9 References

1. Le Calcul, B. S., Non Empirique des constants de force et des derives du moment dipolaire. *Colloq Int C N R S* **1958,** *82*, 287-301.
2. Gerratt, J.; Mills, I. M., Force Constants and Dipole-Moment Derivatives of Molecules from Perturbed Hartree-Fock Calculations. II. Applications to Limited Basis-Set SCF-MO Wavefunctions. *J. Chem. Phys.* **1968,** *49* (4), 1730-1739.
3. Gerratt, J.; Mills, I. M., Force Constants and Dipole-Moment Derivatives of Molecules from Perturbed Hartree-Fock Calculations. I. *J. Chem. Phys.* **1968,** *49* (4), 1719-1729.
4. Pople, J. A.; Krishnan, R.; Schlegel, H. B.; Binkley, J. S., Derivative studies in hartree-fock and møller-plesset theories. *Int. J. Quantum Chem.* **1979,** *16* (S13), 225-241.
5. Harrison, R. J.; Fitzgerald, G. B.; Laidig, W. D.; Bartlett, R. J., Analytic MBPT(2) second derivatives. *Chem. Phys. Lett.* **1986,** *124* (3), 291-294.
6. Handy, N. C.; Amos, R. D.; Gaw, J. F.; Rice, J. E.; Simandiras, E. D., The Elimination of Singularities in Derivative Calculations. *Chem. Phys. Lett.* **1985,** *120* (2), 151-158.
7. Fox, D. J.; Osamura, Y.; Hoffmann, M. R.; Gaw, J. F.; Fitzgerald, G.; Yamaguchi, Y.; Schaefer, H. F., Analytic energy second derivatives for general correlated wavefunctions, including a solution of the first-order coupled-perturbed configuration-interaction equations. *Chem. Phys. Lett.* **1983,** *102* (1), 17-19.
8. Handy, N. C.; Schaefer, H. F., On the evaluation of analytic energy derivatives for correlated wave functions. *J. Chem. Phys.* **1984,** *81* (11), 5031-5033.
9. Koch, H.; Jensen, H. J. A.; Jorgensen, P.; Helgaker, T.; Scuseria, G. E.; Schaefer, H. F., Coupled cluster energy derivatives. Analytic Hessian for the closed-shell coupled cluster singles and doubles wave function: Theory and applications. *J. Chem. Phys.* **1990,** *92* (8), 4924-4940.
10. Gauss, J.; Stanton, J. F., Analytic CCSD(T) second derivatives. *Chem. Phys. Lett.* **1997,** *276* (1), 70-77.
11. Pulay, P., Second and third derivatives of variational energy expressions: Application to multiconfigurational self-consistent field wave functions. *J. Chem. Phys.* **1983,** *78* (8), 5043-5051.

12. Hohenberg, P.; Kohn, W., Inhomogeneous Electron Gas. *Phys. Rev. B* **1964,** *136* (3B), B864-B871.
13. Kohn, W.; Sham, L. J., Self-Consistent Equations Including Exchange and Correlation Effects. *Phys. Rev.* **1965,** *140* (4A), A1133-A1138.
14. Jones, R. O.; Gunnarsson, O., The Density Functional Formalism, Its Applications and Prospects. *Rev Mod Phys* **1989,** *61* (3), 689-746.
15. Ziegler, T., Approximate Density Functional Theory as a Practical Tool in Molecular Energetics and Dynamics. *Chem. Rev.* **1991,** *91* (5), 651-667.
16. Parr, R. G.; Yang, W., *Density-functional theory of atoms and molecules*. Oxford University Press, New York: 1989.
17. Johnson, B. G.; Gill, P. M. W.; Pople, J. A., The performance of a family of density functional methods. *J. Chem. Phys.* **1993,** *98* (7), 5612-5626.
18. Bast, R.; Ekström, U.; Gao, B.; Helgaker, T.; Ruud, K.; Thorvaldsen, A. J., The ab initio calculation of molecular electric, magnetic and geometric properties. *Phys. Chem. Chem. Phys.* **2011,** *13* (7), 2627-2651.
19. Pulay, P., Analytical derivatives, forces, force constants, molecular geometries, and related response properties in electronic structure theory. *Wiley Interdiscip. Rev. Comput. Mol. Sci.* **2014,** *4* (3), 169-181.
20. Schlegel, H. B., AB Initio Energy Derivatives Calculated Analytically. In *Computational Theoretical Organic Chemistry: Proceedings of the NATO Advanced Study Institute held at Menton, France, June 29-July 13, 1980*, Csizmadia, I. G.; Daudel, R., Eds. Springer Netherlands: Dordrecht, 1981; pp 129-159.
21. Pulay, P., Analytical Derivative Methods in Quantum Chemistry. In *Adv. Chem. Phys.*, John Wiley & Sons, Inc.: 1987; pp 241-286.
22. Yamaguchi, Y.; Schaefer, H. F., Analytic Derivative Methods in Molecular Electronic Structure Theory: A New Dimension to Quantum Chemistry and its Applications to Spectroscopy. In *Handbook of High-resolution Spectroscopy*, John Wiley & Sons, Ltd: 2011.
23. Deglmann, P.; Furche, F.; Ahlrichs, R., An efficient implementation of second analytical derivatives for density functional methods. *Chem. Phys. Lett.* **2002,** *362* (5), 511-518.
24. White, C. A.; Johnson, B. G.; Gill, P. M. W.; Headgordon, M., The Continuous Fast Multipole Method. *Chem. Phys. Lett.* **1994,** *230* (1-2), 8-16.
25. Neese, F.; Wennmohs, F.; Hansen, A.; Becker, U., Efficient, approximate and parallel Hartree-Fock and hybrid DFT calculations. A 'chain-of-spheres' algorithm for the Hartree-Fock exchange. *Chem. Phys.* **2009,** *356* (1-3), 98-109.
26. Baerends, E. J.; Ellis, D. E.; Ros, P., Self-consistent molecular Hartree-Fock-Slater calculations I. The computational procedure. *Chem. Phys.* **1973,** *2* (1), 41-51.
27. Dunlap, B. I.; Connolly, J. W. D.; Sabin, J. R., On some approximations in applications of Xα theory. *J. Chem. Phys.* **1979,** *71* (8), 3396-3402.
28. Manzer, S.; Horn, P. R.; Mardirossian, N.; Head-Gordon, M., Fast, accurate evaluation of exact exchange: The occ-RI-K algorithm. *J. Chem. Phys.* **2015,** *143* (2), 024113.
29. White, C. A.; Head-Gordon, M., A J matrix engine for density functional theory calculations. *J. Chem. Phys.* **1996,** *104* (7), 2620-2629.
30. Friesner, R. A., New Methods for Electronic-Structure Calculations on Large Molecules. *Annu. Rev. Phys. Chem.* **1991,** *42*, 341-367.
31. Bykov, D.; Petrenko, T.; Izsak, R.; Kossmann, S.; Becker, U.; Valeev, E.; Neese, F., Efficient implementation of the analytic second derivatives of Hartree-Fock and hybrid DFT

energies: a detailed analysis of different approximations. *Mol. Phys.* **2015,** *113* (13-14), 1961-1977.
32. Kossmann, S.; Neese, F., Comparison of two efficient approximate Hartee-Fock approaches. *Chem. Phys. Lett.* **2009,** *481* (4-6), 240-243.
33. Rebolini, E.; Izsak, R.; Reine, S. S.; Helgaker, T.; Pedersen, T. B., Comparison of Three Efficient Approximate Exact-Exchange Algorithms: The Chain-of-Spheres Algorithm, Pair-Atomic Resolution-of-the-Identity Method, and Auxiliary Density Matrix Method. *J. Chem. Theory Comput.* **2016,** *12* (8), 3514-3522.
34. Almlof, J.; Faegri, K.; Korsell, K., Principles for a Direct Scf Approach to LCAO-MO ab initio Calculations. *J. Comput. Chem.* **1982,** *3* (3), 385-399.
35. Häser, M.; Ahlrichs, R., Improvements on the direct SCF method. *J. Comput. Chem.* **1989,** *10* (1), 104-111.
36. Furlani, T. R.; King, H. F., Implementation of a Parallel Direct SCF Algorithm on Distributed-Memory Compute. *J. Comput. Chem.* **1995,** *16* (1), 91-104.
37. Harrison, R. J.; Guest, M. F.; Kendall, R. A.; Bernholdt, D. E.; Wong, A. T.; Stave, M.; Anchell, J. L.; Hess, A. C.; Littlefield, R. J.; Fann, G. L.; Nieplocha, J.; Thomas, G. S.; Elwood, D.; Tilson, J. L.; Shepard, R. L.; Wagner, A. F.; Foster, I. T.; Lusk, E.; Stevens, R., Toward high-performance computational chemistry: II. A scalable self-consistent field program. *J. Comput. Chem.* **1996,** *17* (1), 124-132.
38. Foster, I. T.; Tilson, J. L.; Wagner, A. F.; Shepard, R. L.; Harrison, R. J.; Kendall, R. A.; Littlefield, R. J., Toward high-performance computational chemistry .1. Scalable Fock matrix construction algorithms. *J. Comput. Chem.* **1996,** *17* (1), 109-123.
39. Brode, S.; Horn, H.; Ehrig, M.; Moldrup, D.; Rice, J. E.; Ahlrichs, R., Parallel Direct SCF and Gradient Program for Workstation Clusters. *J. Comput. Chem.* **1993,** *14* (10), 1142-1148.
40. Harrison, R. J.; Shepard, R., Ab-Initio Molecular Electronic-Structure on Parallel Computers. *Annu. Rev. Phys. Chem.* **1994,** *45*, 623-658.
41. Baker, J.; Wolinski, K.; Malagoli, M.; Pulay, P., Parallel implementation of Hartree-Fock and density functional theory analytical second derivatives. *Mol. Phys.* **2004,** *102* (23-24), 2475-2484.
42. Korambath, P. P.; Kong, J.; Furlani, T. R.; Head-Gordon, M., Parallelization of analytical Hartree-Fock and density functional theory Hessian calculations. Part I: parallelization of coupled-perturbed Hartree-Fock equations. *Mol. Phys.* **2002,** *100* (11), 1755-1761.
43. Mitin, A. V.; Baker, J.; Wolinski, K.; Pulay, P., Parallel stored-integral and semidirect Hartree-Fock and DFT methods with data compression. *J. Comput. Chem.* **2003,** *24* (2), 154-160.
44. Dudley, T. J.; Olson, R. M.; Schmidt, M. W.; Gordon, M. S., Parallel coupled perturbed CASSCF equations and analytic CASSCF second derivatives. *J. Comput. Chem.* **2006,** *27* (3), 352-362.
45. Janowski, T.; Ford, A. R.; Pulay, P., Parallel calculation of coupled cluster singles and doubles wave functions using array files. *J. Chem. Theory Comput.* **2007,** *3* (4), 1368-1377.
46. Ishimura, K.; Pulay, P.; Nagase, S., New parallel algorithm for MP2 energy gradient calculations. *J. Comput. Chem.* **2007,** *28* (12), 2034-2042.
47. Cawkwell, M. J.; Sanville, E. J.; Mniszewski, S. M.; Niklasson, A. M. N., Computing the Density Matrix in Electronic Structure Theory on Graphics Processing Units. *J. Chem. Theory Comput.* **2012,** *8* (11), 4094-4101.
48. Ufimtsev, I. S.; Martinez, T. J., Quantum chemistry on graphical processing units. 1. Strategies for two-electron integral evaluation. *J. Chem. Theory Comput.* **2008,** *4* (2), 222-231.

49. Yasuda, K., Two-electron integral evaluation on the graphics processor unit. *J. Comput. Chem.* **2008,** *29* (3), 334-342.
50. Yasuda, K., Accelerating density functional calculations with graphics processing unit. *J. Chem. Theory Comput.* **2008,** *4* (8), 1230-1236.
51. Ufimtsev, I. S.; Martinez, T. J., Quantum Chemistry on Graphical Processing Units. 2. Direct Self-Consistent-Field Implementation. *J. Chem. Theory Comput.* **2009,** *5* (4), 1004-1015.
52. Hohenstein, E. G.; Luehr, N.; Ufimtsev, I. S.; Martinez, T. J., An atomic orbital-based formulation of the complete active space self-consistent field method on graphical processing units. *J. Chem. Phys.* **2015,** *142* (22), 224103.
53. Bhaskaran-Nair, K.; Ma, W. J.; Krishnamoorthy, S.; Villa, O.; van Dam, H. J. J.; Apra, E.; Kowalski, K., Noniterative Multireference Coupled Cluster Methods on Heterogeneous CPU-GPU Systems. *J. Chem. Theory Comput.* **2013,** *9* (4), 1949-1957.
54. Apra, E.; Kowalski, K., Implementation of High-Order Multireference Coupled-Cluster Methods on Intel Many Integrated Core Architecture. *J. Chem. Theory Comput.* **2016,** *12* (3), 1129-1138.
55. DePrince, A. E.; Hammond, J. R., Coupled Cluster Theory on Graphics Processing Units I. The Coupled Cluster Doubles Method. *J. Chem. Theory Comput.* **2011,** *7* (5), 1287-1295.
56. Vogt, L.; Olivares-Amaya, R.; Kermes, S.; Shao, Y.; Amador-Bedolla, C.; Aspuru-Guzik, A., Accelerating resolution-of-the-identity second-order Moller-Plesset quantum chemistry calculations with graphical processing units. *J. Phys. Chem. A* **2008,** *112* (10), 2049-2057.
57. Pulay, P., Ab initio calculation of force constants and equilibrium geometries in polyatomic molecules. *Mol. Phys.* **1969,** *17* (2), 197-204.
58. De Roure, D.; Jennings, N. R.; Shadbolt, N. R., The Semantic Grid: Past, present, and future. *P Ieee* **2005,** *93* (3), 669-681.
59. Pordes, R. P., D.; Kramer, B.; Olson, D.; Livny, M.; Roy, A.; Avery, P.; Blackburn, K.; Wenaus, T.; Wurthwein, F.; Foster, I.; Gardner, R.; Wilde, M.; Blatecky, A.; McGee, J.; Quick, R., The open science grid. *J. Phys. Conf. Ser.* **2007,** *78*, 012057.
60. Garzoglio, G.; Alderman, I.; Altunay, M.; Ananthakrishnan, R.; Bester, J.; Chadwick, K.; Ciaschini, V.; Demchenko, Y.; Ferraro, A.; Forti, A.; Groep, D.; Hesselroth, T.; Hover, J.; Koeroo, O.; La Joie, C.; Levshina, T.; Miller, Z.; Packard, J.; Sagehaug, H.; Sergeev, V.; Sfiligoi, I.; Sharma, N.; Siebenlist, F.; Venturi, V.; Weigand, J., Definition and Implementation of a SAML-XACML Profile for Authorization Interoperability Across Grid Middleware in OSG and EGEE. *J Grid Comput.* **2009,** *7* (3), 297-307.
61. Thain, D.; Tannenbaum, T.; Livny, M., Distributed computing in practice: the Condor experience. *Concurr. Comp.- Pract. E.* **2005,** *17* (2-4), 323-356.
62. Couvares, P. K., T.; Roy, A.; Weber, J.; Wenger, K., *Workflow in Condor*. Springer Press: 2007.
63. Liu, K. Y.; Liu, J.; Herbert, J. M., Accuracy of finite-difference harmonic frequencies in density functional theory. *J. Comput. Chem.* **2017,** *38* (19), 1678-1684.
64. Becke, A. D., Density-Functional Exchange-Energy Approximation with Correct Asymptotic-Behavior. *Phys. Rev. A* **1988,** *38* (6), 3098-3100.
65. Lee, C. T.; Yang, W. T.; Parr, R. G., Development of the Colle-Salvetti Correlation-Energy Formula into a Functional of the Electron-Density. *Phys. Rev. B* **1988,** *37* (2), 785-789.
66. Franke, R.; Van Wullen, C., First-order relativistic corrections to MP2 energy from standard gradient codes: Comparison with results from density functional theory. *J. Comput. Chem.* **1998,** *19* (14), 1596-1603.

67. Pantazis, D. A.; Chen, X. Y.; Landis, C. R.; Neese, F., All-electron scalar relativistic basis sets for third-row transition metal atoms. *J. Chem. Theory Comput.* **2008,** *4* (6), 908-919.
68. Weigend, F.; Ahlrichs, R., Balanced basis sets of split valence, triple zeta valence and quadruple zeta valence quality for H to Rn: Design and assessment of accuracy. *Phys. Chem. Chem. Phys.* **2005,** *7* (18), 3297-3305.
69. Eichkorn, K.; Weigend, F.; Treutler, O.; Ahlrichs, R., Auxiliary basis sets for main row atoms and transition metals and their use to approximate Coulomb potentials. *Theor. Chem. Acc.* **1997,** *97* (1-4), 119-124.
70. Weigend, F.; Haser, M.; Patzelt, H.; Ahlrichs, R., RI-MP2: optimized auxiliary basis sets and demonstration of efficiency. *Chem. Phys. Lett.* **1998,** *294* (1-3), 143-152.
71. Dolan, N. S.; Scamp, R. J.; Yang, T.; Berry, J. F.; Schomaker, J. M., Catalyst-Controlled and Tunable, Chemoselective Silver-Catalyzed Intermolecular Nitrene Transfer: Experimental and Computational Studies. *J. Am. Chem. Soc.* **2016,** *138* (44), 14658-14667.
72. Grimme, S., Semiempirical hybrid density functional with perturbative second-order correlation. *J. Chem. Phys.* **2006,** *124* (3), 034108.
73. Neese, F., Software update: the ORCA program system, version 4.0. *Wiley Interdiscip. Rev. Comput. Mol. Sci.* **2017**, e1327.
74. Neese, F., The ORCA program system. *Wiley Interdiscip. Rev.: Comput. Mol. Sci.* **2012,** *2* (1), 73-78.
75. Shimanouchi, T., *Tables of Molecular Vibrational Frequencies Consolidated Volume I*. Gaithersburg MD, 20899, 1972.
76. Lippincott, E. R.; O'Reilly, E. J., Vibrational Spectra and Assignment of Naphthalene and Naphthalene-*d*-8. *J. Chem. Phys.* **1955,** *23* (2), 238-244.
77. Pople, J. A.; Krishnan, R.; Schlegel, H. B.; Binkley, J. S., Derivative Studies in Hartree-Fock and Moller-Plesset Theories. *Int. J. Quantum Chem.* **1979,** *16*, 225-241.
78. Halkier, A.; Helgaker, T.; Jørgensen, P.; Klopper, W.; Koch, H.; Olsen, J.; Wilson, A. K., Basis-set convergence in correlated calculations on Ne, N_2, and H_2O. *Chem. Phys. Lett.* **1998,** *286* (3), 243-252.
79. Cané, E.; Miani, A.; Palmieri, P.; Tarroni, R.; Trombetti, A., The gas-phase infrared spectra of anthracene-h_{10} and anthracene-d_{10}. *J. Chem. Phys.* **1997,** *106* (22), 9004-9012.
80. Goerigk, L.; Grimme, S., Double-hybrid density functionals. *Wiley Interdiscip. Rev.: Comput. Mol. Sci.* **2014,** *4* (6), 576-600.
81. Ziolkowski, M.; Jansik, B.; Kjaergaard, T.; Jorgensen, P., Linear scaling coupled cluster method with correlation energy based error control. *J. Chem. Phys.* **2010,** *133* (1), 014107.

5 *Combining the Cambridge Structural Database with the Open Science Grid: High Throughput Structural Generation for Catalyst Virtual Screening*

Yang, T.; Berry, J. F.*

Department of Chemistry, University of Wisconsin—Madison, Madison, Wisconsin 53706, USA

5.1 Abstract

Quantum chemistdry provides the possibility to predict properties of a system. The accuracy of the prediction depends on the level of theory employed and a time-performance trade-off is required when predictions concerning experimental results are of interested, particularly those in the condensed phase. To reduce the amount of time spent in theoretical investigation, existing experimental databases serves as a solid foundation. In addition, high throughput computing power can be utilized to elevate the performance aspect of quantum chemistry. In this work, we present the idea of bridging the Cambridge Structural Database with the Open Science Grid to effect high throughput generation of initial catalyst-substrate transition state structures based on pre-optimized TS structures of substrates and catalyst structures retrieved from the database.

5.2 Introduction

One of the biggest promises of quantum chemistry is the ability to predict properties of a system with the corresponding operator for each property investigated given an exact wavefunction or density and its density functional.[1] One issue with this promise is that the size of chemical space in reality is vast and the time-performance trade-off requires either the selection of

some portions of the chemical space, based on chemical intuition, or a sacrifice of the computational accuracy. Another angle to look at this issue regarding the time-performance trade-off is that one either has to ask the right questions or has to possess a large amount of computational resources. One method to ensure that hypotheses regarding a chemical reaction are sensical is to compare the hypotheses to known reports of similar, if not identical, chemical observations. This method requires a database of chemical observations and a systematic procedure that allows comparisons between the hypotheses regarding a chemical reaction to information in the database.

Chart 5.1. The number of crystal structures in the Cambridge Structural Database partitioned into structures that contain one (orange) or two (grey) transition metals and the rest (blue)

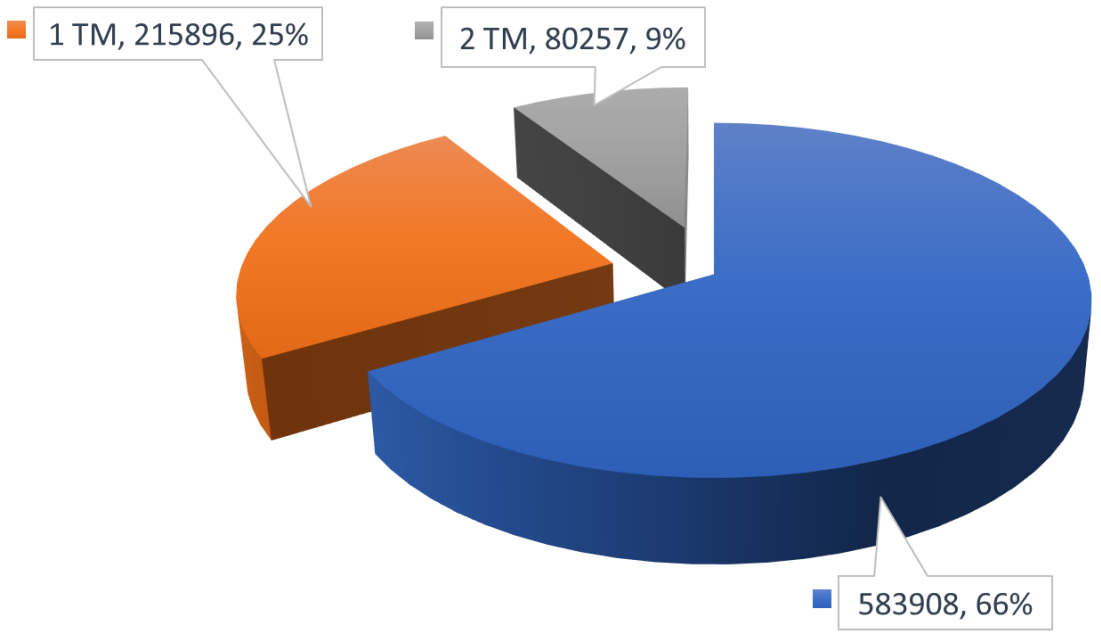

One of the databases that curates mostly high-resolution data and information regarding chemical systems is the Cambridge Structural Database (CSD). [2] The CSD curates more than 0.88 million single crystal structures of molecular compounds, dating back to 1923, as of February 2018. Among them, 216 thousand structures contain one transition metal and 80 thousand structures contain two transition metals (Chart 5.1). Many structures were crystallized from the solution

phase into the solid phase to allow crystal ordering during the slow crystallization process. This crystallization process allows the inclusion of multiple conformations of the transition metal complex (disorder) and solvent molecules in the crystal. In addition, the lack of charge screening by solvent molecules causes counterions bound to each other in the solid phase on occasions. Therefore, the crystal structures in the CSD serves as a good point to ask the "right questions" although precautions are needed to ensure "artifacts" generated from the crystallization process are contained when solution behavior of interest.

The CSD contains a large amount of high-resolution crystal structures, obtained from slow crystallization process to ensure crystal ordering. This experimental necessity intrinsically reduces the likelihood of crystallizing fleeting species during a chemical reaction, such as transition states (TSs), transient reaction intermediates, and thermally or photo-excited states. Therefore, the structure of these reactive species can usually be modeled efficiently by quantum chemistry. Numerous computational studies have been published in the literature focusing on different aspects of a catalytic cycle, such as the rate-determining step and the product-determining step. These studies provide "high-quality" structures of reactive species during a reaction and a portion of these structures can be harvested and used as initial TS structures for high throughput virtual screening (HTVS) of potential catalysts, whose structures are based on those in the CSD.

These "high-quality" structures of reactive species, i.e. TS structures, obtained from truncating catalyst-substrate complexes (Cat-Sub complexes) modeled by quantum chemistry in the literature encounter a problem when they are combined with the potential catalyst structures in the CSD: The truncation eliminates the information regarding the binding mode of these TS structures. This information is important to the accurate modeling of reactions in a catalytic cycle and is usually cross-referenced to indirect investigations of the reactive species, such as

spectroscopies, mass spectrometry, and microscopies. To mitigate this issue, conformation sampling of the generated Cat-Sub complexes using the truncated TS structures from the literature and the structures in the CSD is necessary. One method to generate multiple conformations of Cat-Sub complexes is docking based on a stochastic algorithm (i.e. the Lamarckian genetic algorithm[3]). Docking provides a method to mimic the stochastic collision process before the formation of the TS in the condensed phase; each docked conformation can be thought as a replicate of a collision event derived from a collision orientation.

Figure 5.1. Status map of the Open Science Grid (OSG). The green circles denote OSG sites.

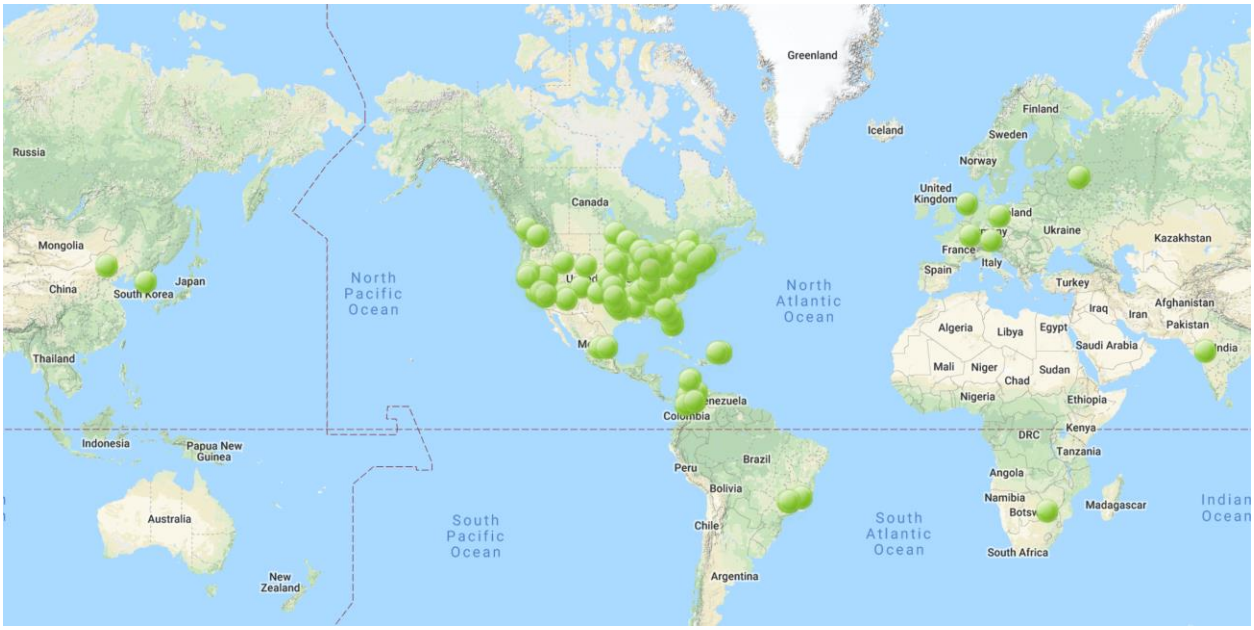

The chemical space is narrowed to experimentally derived structures curated in the CSD and truncated substrate structures from computational studies. However, there are still at least 0.29 million structures for each substrate structure that can be investigated. To facilitate the database-driven high-throughput catalyst-substrate complex generation, we propose to employ grid computing is employed. Grid computing is a distributed system where the collection of computing nodes is geographically dispersed utilizing diverse computer architectures.[4] One of the computing grids available in the United States is the Open Sc ience Grid (OSG).[5-6] Users of a computing grid

can submit their jobs to the agent Condor-G,[7] which bridges the jobs from users to available resources in the grid. One advantage of grid computing compared to high performance computing commonly employed for computational chemistry is its high scalability in terms of the number of jobs. This feature is particular beneficial for catalyst-substrate docking because multiple stochastic processes can be started concurrently with different seeds to allow multiple concurrent sampling of conformations.

To screen the chemical space in the CSD using the vast computing power of the OSG, we present here a preparatory step for the grand scheme of database-focused computational HTVS of molecular catalysts. In this work, we present a method to allow fast generation of a suite of catalyst-substrate complexes ready for TS optimization: 1) Generation of TS structures of the targeted organic transformations without the catalyst, 2) catalyst structure retrieval from the CSD and pre-processing, and 3) generation of the structures of most likely catalyst-substrate transition state complexes using the docking program Autodock.[8] Additionally, due to the scope of the project, on-the-fly job execution, data analysis, and file generation are necessary. Hence, automation enabled by the directed acyclic graph manager (DAGMan) utility[9] of the HTCondor software framework[10] is also outlined.

5.3 Implementation

5.3.1 Structural generation of transition state for the targeted organic transformations

The TS structures of targeted organic transformations can be generated from TS optimization of the organic reactive intermediate. Another source of TS optimized structure of the targeted organic transformations are structural fragments from reported computational studies in the literature. For example, a TS structure of an intramolecular nitrene insertion into the γC–H

bond obtained by removing the silver catalyst from the TS catalyst-substrate complex reported in the literature (Figure 5.2).[11] The advantage of optimizing the organic fragment to the TS first before introducing the catalyst is that ab initio molecular dynamics can easily be affordable for smaller molecular structures or truncated models to sample various TS isomers that may be responsible for the desired transformations.

Figure 5.2. Generation of the transition state optimized structure for intramolecular nitrene transfer by removing the silver catalyst based on a literature reported computational structure.

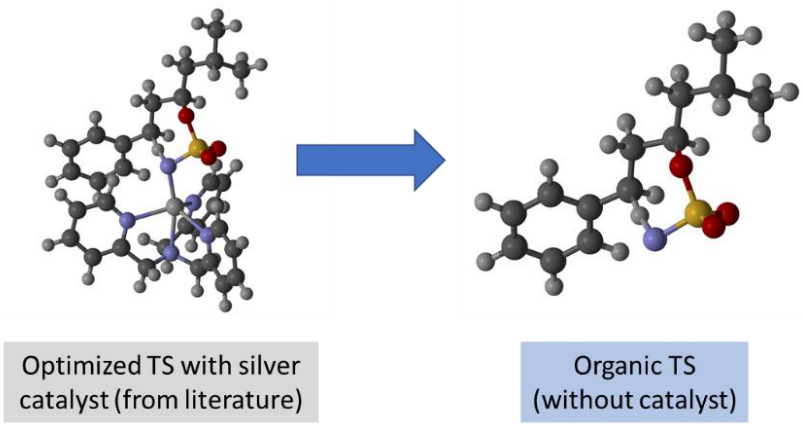

5.3.2 Catalyst structure retrieval and pre-processing.

5.3.2.1 Structure retrieval

The structures of potential catalysts are obtained from the Cambridge Structural Database (CSD).[2] Structures that contain at most two transition metals are targeted in this study due to the fact that the number of spin states needed to be considered grows proportionally to the number of transition metal centers and the number of near degenerate spin states (i.e. magnetically coupled states) increase. To manipulate these structures, the Python application programming interface (API) of the CSD is exploited. [2] This API allows structural retrieval, manipulation, and analysis. Structures deposited in the CSD can be retrieved using their respectively reference code (refcode) in the format of a crystallographic information file (.cif), which contains information pertaining to single crystal X-ray diffraction (SC-XRD) data acquisition, the unit cell of the crystal, and the

molecule itself; Tripos exchange format files (.mol2), which contains atomic, bond, molecular, and connectivity information; and other formats such as CSD coordinate files (.coord) and protein database format (.pdb). Mol2 format is particularly advantageous for structural analysis because it contains molecular information describing the assignment of atoms in each molecule in a file, such as components of disordered structures in a file, which are also found in cifs, but also connectivity such as bond orders.

5.3.2.2 Structure patching

After retrieving the desired structures in mol2 format, molecular structures in each mol2 file have to be processed because each file can contain more than one molecule, counter-ions, solvent molecules, and disordered components, and/or have missing hydrogen atoms. To process mol2 files, the API function atoms, neighbours, bonds, add_hydrogens(), and components are used. The atoms function outputs all atoms in the file; the neighbours function outputs all neighboring atoms of a given atom connected through bonds; the bonds function outputs all bonds pertained to a given atom (outputs of the bonds function contain the outputs of the neighbours function); the add_hydrogens() function adds/removes hydrogen atoms to satisfy the octet of atoms such as C, N, O, P, and S. This function will be discussed in detail below; the components function outputs each molecule residue assigned in a mol2 file. For example, disordered positions are represented as duplicates of a molecule in which the atomic position of the disordered regions differs. Each duplicate is assigned a residue number (i.e. 1 and 2).

The add_hydrogens() function deserves in depth discussion because it adds/removes atoms to mol2 files. The accuracy of this function is crucial to subsequent steps because both missing and extra hydrogen atoms will result in failed structural optimization and/or an incorrect number of electrons. From empirical observation, the function adds or removes hydrogen atoms to C, N,

O, P, and S atoms according to the octet rule. This function relies on the bond order assignments from mol2 files to distinguish among aliphatic, aromatic, alkenyl, and alkynyl carbon atoms; among amino, amido, imido, and nitride nitrogen atoms; among aqua, oxy and oxido oxygen atoms; between phosphino and phosphido phosphorus atoms; and among sulfur atoms with zero, one, and two valencies. This function successfully adds missing hydrogen atoms in phenyl rings. However, for example, for N-heterocyclic carbene (NHC) ligands, an extra hydrogen atom is erroneously added to the 2-position due to the assignments of a single bond between the 1-position and the 2-position, between the 3-position and the 2-position, and between the coordinated transition metal and the 2-position. These assignments render the carbon atom at the 2-position missing one valency, causing the add_hydrogens() function to add one hydrogen atom to the 2-position. Another problematic example occurs in mol2 files with unknown bond types, such as Ag-alkene noncovalent interactions, which are usually assigned “dashed” bonds (equivalent to unknown bonds in mol2 files) in the pictorial representation given in the CSD.

To remedy the issue where add_hydrogens() adds/removes hydrogens undesirably, a python script (bond_mod+add_H+split_comp.py) was written to modify the bonds between transition metal centers and atoms in their first coordination sphere, when these atoms are C, N, O, P, or S, in each mol2 file to ensure these coordinating atoms have the correct valency according to their periodicity in the periodic table. In the NHC example above, the single bond between the carbon at the 2-position and the transition metal will be modified to a double bond to ensure the carbon atom makes four bonds (Scheme 5.1). Another common example seen in crystal structures is the valency of coordinating oxygen atoms in aqua ligands. These oxygen atoms are assigned three bonds due to the single bond that connects to the transition metal. The add_hydrogens() function will systematically remove one of the two hydrogen atoms to maintain the valency of two

of oxygen. To eliminate this undesired removal of a hydrogen atom, our bond_mod+add_H+split_comp.py script removes the single bond between the oxygen atom and the transition metal. One precaution pertaining to bond removal in case of hypervalency is that the transition metal complex and the ligand (the aqua ligand in the example) are treated as two components unless they are connected through another bond. Hence, bonds that are removed by the bond_mod+add_H+split_comp.py script are recorded in a separate text file and added back to after the add_hydrogens() function is executed to maintain the number of components in the mol2 file. One caveat with this first coordination sphere based fix to the add_hydrogens() enclosed in bond_mod+add_H+split_comp.py is that problems with valency beyond the first coordination sphere are ignored.

Scheme 5.1. First coordination sphere fix for hypovalency using the bond_mod+add_H+split_comp.py script

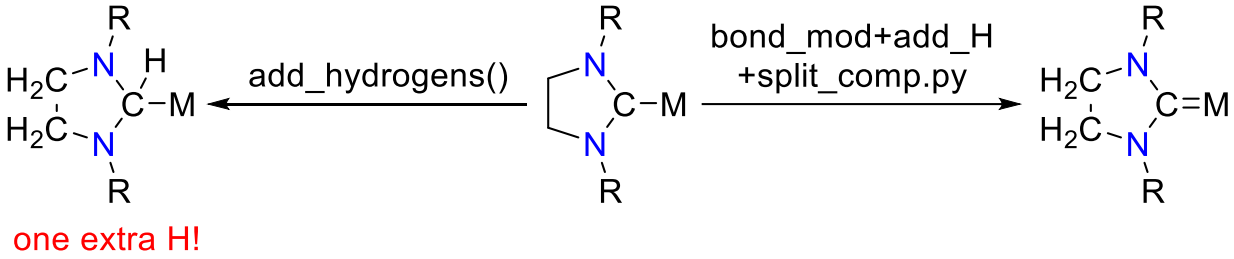

5.3.2.3 Stripping components and ligand removal

After the bond modification of the first coordination sphere, missing hydrogen atoms are added using the add_hydrogens() function followed by the components function to separate each hydrogen-added mol2 file (modified.mol2) into child mol2 files (modified.RES#.mol2; # = 1, 2, 3,…, n; n = number of components) that contain each component of the original modified.mol2 file. Child mol2 files that contain no transition metals or only one atom are discarded. The remaining modified.RES#.mol2 files can be counter-ion pairs containing transition metals, enantiomer pairs in an asymmetric space group, or a second molecule of the complex that is not

related by crystallographic symmetry. To sift through these three possibilities, one of the modified.RES#.mol2 files that has the same constituent atoms is kept for further studies. This coarse filter removes one of the enantiomer pairs and all but one molecules related by symmetry.

Among the bonds in the each modified.RES#.mol2 file, one or more of those that directly connect atoms to the transition metal centers may be formed during the crystallization procedure; the strength of the bonds could be weak enough to dissociate in solution due to solvent charge screening. Therefore, some of the structures in these modified.RES#.mol2 files will not reflect the correct solution structure. In addition, some of the structures in these modified.RES#.mol2 files will be the structure of apre-catalyst that requires ligand dissociation to form a catalytically active molecule; a dynamic equilibrium between the CSD structure in one modified.RES#.mol2 and the active structure could occur in solution. To mitigate these issues, we take advantage of the concept of denticity: the number of coordinating atoms that a ligand has in a coordination complex, i.e. each bipyridine ligand in $[Ru(bpy)_3]^{2+}$ has a denticity of 2. A polydentate ligand is usually less labile than a monodentate ligand due to both entropic (i.e. a bidentate ligand can exist in 3 forms, both coordination atoms bound or either of the coordination atoms bound) and enthalpic effects (two bonds need to be broken in order for the ligand to dissociate). Hence, for the structure in a modified.RES#.mol2 file, we can categorize each ligand as monodentate or polydentate. If a ligand is monodentate, it can be removed from the modified.RES#.mol2 to generate a child file (modified.RES#.FRAG@.mol2, @ = 1, 2, …, n; n = number of monodentate ligands). To find monodentate ligands in a modified.RES#.mol2 file and remove each of them separately to generate modified.RES#.FRAG@.mol2 child files, a shell script (denticity+frags.sh) was written. The script does the following: 1) for each metal center (Atom1), connecting atoms are listed (AtomsLayer1). 2) for each atom in the first layer, connecting atoms are listed except Atom1

(AtomsLayer2). 3) for each atom in the second layer, connecting atoms are listed except those in AtomsLayer1 (AtomsLayer3). Step 3) is repeated until there are no more connecting atoms. If any of the atoms beyond the second layer is Atom1, this ligand is polydentate. Otherwise, this ligand is monodentate and all atoms found through step 1), 2), and 3) are sorted for unique atoms and recorded. This procedure is repeated for each metal center in a modified.RES#.mol2 file. Based on the logical expression for denticity and the atoms recorded, fragments of a modified.RES#.mol2 file is generated and named modified.RES#.FRAG@.mol2 file (Figure 5.3).

Figure 5.3. An example of the component stripping and ligand removal procedure

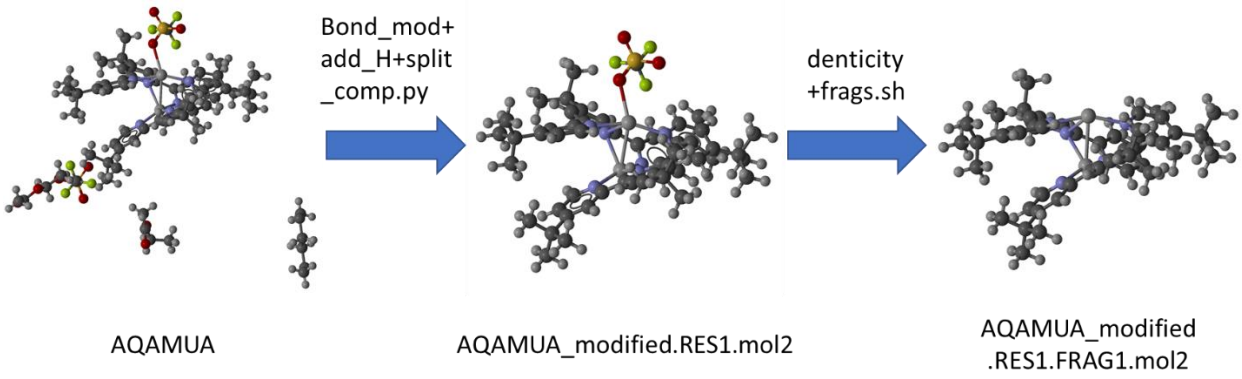

5.3.3 Generation of the catalyst-substrate transition state complex

To introduce the TS optimized structure of the targeted organic transformation (substrate) to modified.RES#.mol2 and modified.RES#.FRAG@.mol2 files of catalysts generated in section 5.3.2, the program Autodock is utilized to dock the target to the catalyst—or the ligand to the receptor, respectively, in the language of Autodock, which is used to describe the procedures in this section. To perform docking, there are two parameter files and two PDBQT files needed: a grid parameter file (gpf), a docking parameter file (dpf), ligand and receptor PDBQT files. These files are generated by the Autodock program based on the PDB format of the ligand and receptor mol2 files, which can be converted into PDB format by open babel.[12]

5.3.4 Automation enabled by DAGMan

Because the scope of this project is on the order of thousands of complexes to be screened, automation is indispensable. The DAGMan utility of HTCondor was employed to enable the automation of the catalyst-substrate transition state initial structure generation for HTVS (Scheme 5.2). 1) Crystal structure are retrieved as mol2 files followed by 2) file pre-processing using the bond_mod+add_H+split_comp.py script to correct for the number of hydrogen atoms and split components. 3) each ligand in each component mol2 file is analyzed for its denticity and removed to generate a child mol2 file if monodentate by the denticity+frags.sh script. 4) The modified.RES#.mol2 files, modified.RES#.FRAG@.mol2 files, and the truncated TS structures from the literature are used to prepare docking files using the Autodock file generation program and 5) are docked with a using Autodock to sample potential Cat-Sub TS structures.

Scheme 5.2. Process flow for automating the catalyst-substrate TS initial structure generation

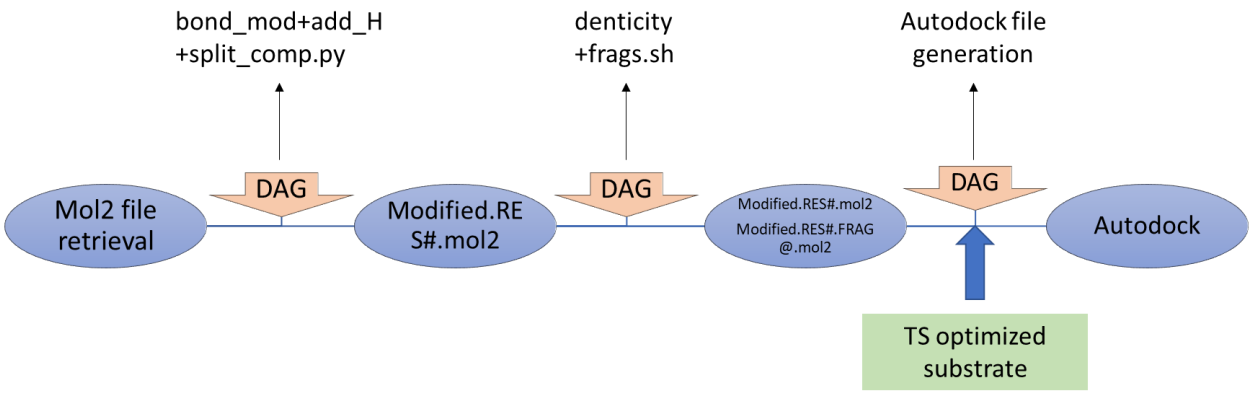

5.4 Preliminary Results

5.4.1 Statistics on the number of files generated at each stage of structure pre-processing

5565 modified.mol2 files containing one or two Ag atoms are chosen as a primer for catalyst-substrate transition state structure generation for HTVS. Structural pre-processing using bond_mod+add_H+split_comp.py generates 6183 modified.RES#.mol2 files followed by denticity+frags.sh, which generates 9409 modified.RES#.FRAG@.mol2 files.

5.4.2 Docking procedure

We show here using the organic portion of an intramolecular nitrene insertion catalyzed by a silver tpa (tpa = tris(2-pyridylmethyl)amine) complex reported by Huang, *et al*.[11] The potential catalyst structure was obtained from the CSD with the refcode EXEZOU. The procedure is outlined in Scheme 5.3. For the TS that abstracts the benzylic C–H bond, a Ag–N bond of 2.227 Å was found. Three other Cat-Sub complexes with Ag–N distances less than 3.0 Å were found (2.7, 2.774, and 2.806 Å). On the other hand, no Cat-Sub complexes with Ag–N bond within 3.0 Å were found for the TS that abstracts the 3º C–H bond.

Scheme 5.3. Docking procedure from the truncated TS structures to the catalyst-substrate complexes

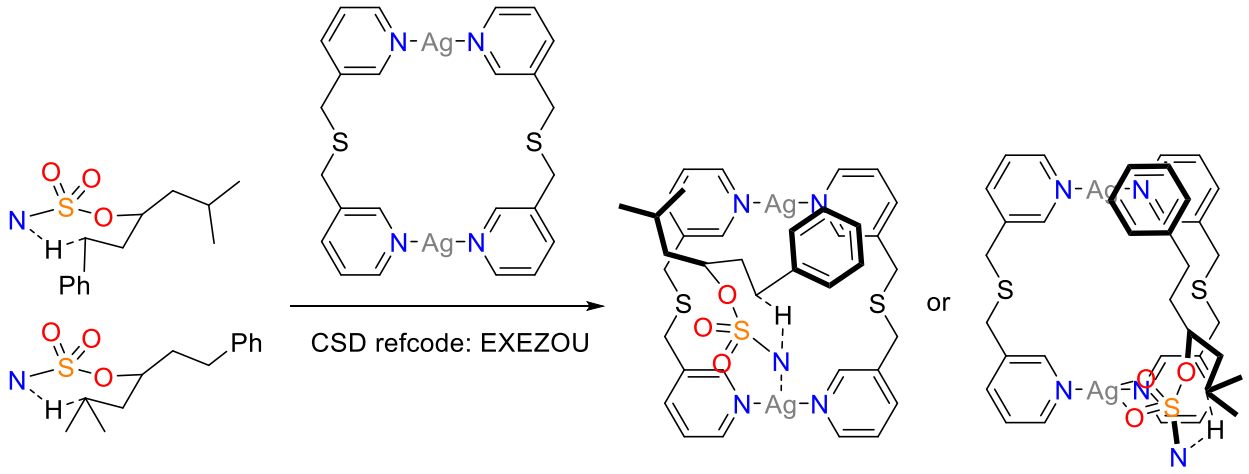

5.4.3 Docking results

1354 out of the 6183 modified.RES#.mol2 files were selected as a test for their manageable molecule size, containing 6 to 154 atoms. Three representative catalyst-substrate structures from one docking run are shown in Figure 5.4. The modified.RES1.mol2 file was generated based on the crystal structure EXEZOW and the substrate structure was taken from a published computational study on silver-catalyzed intramolecular regioselective nitrene transfer[11] and shows a sulfamyl nitrene abstracting one benzylic C–H bond.

Figure 5.4. Three catalyst-substrate structures generated using Autodock.

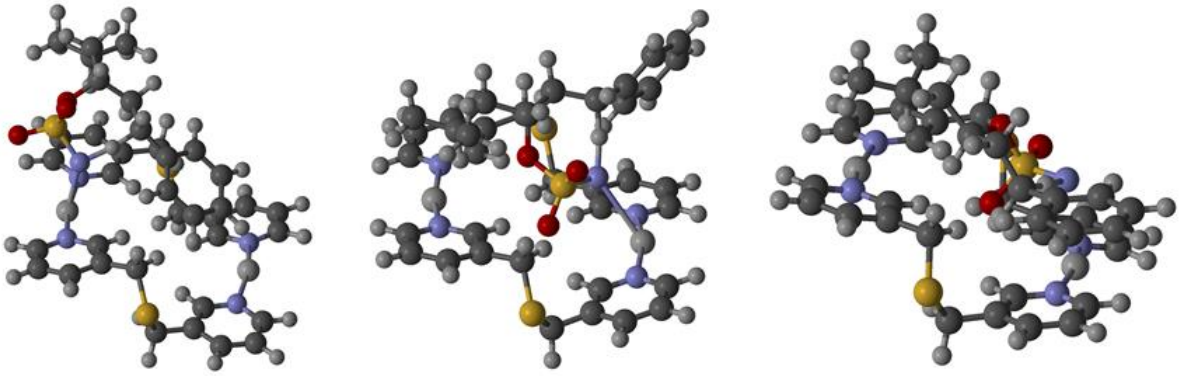

5.5 Conclusion and Outlook

In this chapter, we presented the workflow that allows structural retrieval and patching, component stripping and ligand removal for catalysts followed by catalyst-substrate docking based on transition state optimized intramolecular nitrene insertion fragments from literature to generate the initial transition state geometry for HTVS. Future directions for this project are as following: All the scripts written for this project will be collected into a toolbox and a master script will be written to allow user friendly interactive execution of the code, in the form of either command lines or graphic user interface, which can be achieved by PyQt5. Ultimately, the goal is for any users with a CSD license to easily perform HTVS of their desired organic transformations onto the whole depository of monometallic and bimetallic structures in the CSD.

5.6 Acknowledgments

J.F.B. thanks the Center for Selective C−H Functionalization supported by the National Science Foundation (CHE-1700982). The computational facility at Madison is supported in part by National Science Foundation Grant CHE-0840494 and at the UW—Madison Center for High Throughput Computing (CHTC) in the Department of Computer Sciences. The CHTC is supported

by UW—Madison, the Advanced Computing Initiative, the Wisconsin Alumni Research Foundation, the Wisconsin Institutes for Discovery, and the National Science Foundation, and is an active member of the Open Science Grid, which is supported by the National Science Foundation award 1148698 and the U.S. Department of Energy's Office of Science. We are grateful to Prof. Frank A. Weinhold at the University of Wisconsin—Madison for providing a gratis copy of the NBO 6.0 program.

5.7 References

1. Sperger, T.; Sanhueza, I. A.; Schoenebeck, F., Computation and Experiment: A Powerful Combination to Understand and Predict Reactivities. *Acc. Chem. Res.* **2016,** *49* (6), 1311-1319.
2. Groom, C. R.; Bruno, I. J.; Lightfoot, M. P.; Ward, S. C., The Cambridge Structural Database. *Acta Crystallogr B* **2016,** *72*, 171-179.
3. Morris, G. M.; Goodsell, D. S.; Halliday, R. S.; Huey, R.; Hart, W. E.; Belew, R. K.; Olson, A. J., Automated docking using a Lamarckian genetic algorithm and an empirical binding free energy function. *J. Comput. Chem.* **1998,** *19* (14), 1639-1662.
4. De Roure, D.; Jennings, N. R.; Shadbolt, N. R., The Semantic Grid: Past, present, and future. *P Ieee* **2005,** *93* (3), 669-681.
5. Pordes, R. P., D.; Kramer, B.; Olson, D.; Livny, M.; Roy, A.; Avery, P.; Blackburn, K.; Wenaus, T.; Wurthwein, F.; Foster, I.; Gardner, R.; Wilde, M.; Blatecky, A.; McGee, J.; Quick, R., The open science grid. *J. Phys. Conf. Ser.* **2007,** *78*, 012057.
6. Sfiligoi, I., Bradley, D. C., Holzman, B., Mhashilkar, P., Padhi, S. and Wurthwein, F. In *The Pilot Way to Grid Resources Using glideinWMS*, 2009 WRI World Congress on Computer Science and Information Engineering, 2009; pp 428-432.
7. James Frey, T. T., Ian Foster, Miron Livny, Steve Tuecke. In *Condor-G: A computation management agent for multi-institutional grids.*, Proceedings of the Tenth IEEE Symposium on High Performance Distributed Computing (HPDC), San Francisco, California, San Francisco, California, 2001; pp 7-9.
8. Morris, G. M.; Huey, R.; Lindstrom, W.; Sanner, M. F.; Belew, R. K.; Goodsell, D. S.; Olson, A. J., AutoDock4 and AutoDockTools4: Automated Docking with Selective Receptor Flexibility. *J. Comput. Chem.* **2009,** *30* (16), 2785-2791.
9. Couvares, P. K., T.; Roy, A.; Weber, J.; Wenger, K., *Workflow in Condor*. Springer Press: 2007.
10. Thain, D.; Tannenbaum, T.; Livny, M., Distributed computing in practice: the Condor experience. *Concurr. Comp.- Pract. E.* **2005,** *17* (2-4), 323-356.
11. Huang, M. X.; Yang, T.; Paretsky, J. D.; Berry, J. F.; Schomaker, J. M., Inverting Steric Effects: Using "Attractive" Noncovalent Interactions To Direct Silver-Catalyzed Nitrene Transfer. *J. Am. Chem. Soc.* **2017,** *139* (48), 17376-17386.
12. O'Boyle, N. M.; Banck, M.; James, C. A.; Morley, C.; Vandermeersch, T.; Hutchison, G.

R., Open Babel: An open chemical toolbox. *J Cheminformatics* **2011,** *3*.

Appendix A Other Published Work

A.1 Work published at the Johns Hopkins University

A.1.1 Singlet versus Triplet Reactivity in an Mn(V)−Oxo Species: Testing Theoretical Predictions Against Experimental Evidence

Yang, T.;[†] Quesne, M. G.[‡,§] Neu, H. N.;[†] Reinhard, F. G. C.;[‡] Goldberg, D. P.;[*,†] and de Visser, S. P.[*,‡]

[†]Department of Chemistry, The Johns Hopkins University, Baltimore, Maryland 21218, USA

[‡]Manchester Institute of Biotechnology and School of Chemical Engineering and Analytical Science, The University of Manchester, Manchester M1 7DN, United Kingdom

Abstract: Discerning the factors that control the reactivity of high-valent metal−oxo species is critical to both an understanding of metalloenzyme reactivity and related transition metal catalysts. Computational studies have suggested that an excited higher spin state in a number of metal−oxo species can provide a lower energy barrier for oxidation reactions, leading to the conclusion that this unobserved higher spin state complex should be considered as the active oxidant. However, testing these computational predictions by experiment is difficult and has rarely been accomplished. Herein, we describe a detailed computational study on the role of spin state in the reactivity of a high-valent manganese(V)−oxo complex with para-Z-substituted thioanisoles and utilize experimental evidence to distinguish between the theoretical results. The calculations show an unusual change in mechanism occurs for the dominant singlet spin state that correlates with the electron-donating property of the para-Z substituent, while this change is not observed on the triplet spin state. Minimum energy crossing point calculations predict small spin−orbit coupling constants making the spin state change from low spin to high spin unlikely. The trends in reactivity for the para-Z-substituted thioanisole derivatives provide an experimental measure for the spin

state reactivity in manganese−oxo corrolazine complexes. Hence, the calculations show that the V-shaped Hammett plot is reproduced by the singlet surface but not by the triplet state trend. The substituent effect is explained with valence bond models, which confirm a change from an electrophilic to a nucleophilic mechanism through a change of substituent.

A.1.2 Oxygen-Atom Transfer Reactivity of Axially Ligated Mn(V)−Oxo Complexes: Evidence for Enhanced Electrophilic and Nucleophilic Pathways

Neu, H. M.;[†] Yang, T.;[†] Baglia, R. A.;[†] Yosca, T. H.[§] Green, M. T.;[*,§] Quesne, M. G.;[‡] de Visser, S. P.;[*,‡] and Goldberg, D. P.[*,†]

[†]Department of Chemistry, The Johns Hopkins University, Baltimore, Maryland 21218, USA

[§]Department of Chemistry, Pennsylvania State University, University Park, Pennsylvania 16802, USA

[‡]The Manchester Institute of Biotechnology and School of Chemical Engineering and Analytical Science, The University of Manchester, Manchester M1 7DN, United Kingdom

Abstract: Addition of anionic donors to the manganese(V)−oxo corrolazine complex $Mn^{V}(O)(TBP_8Cz)$ has a dramatic influence on oxygen-atom transfer (OAT) reactivity with thioether substrates. The six coordinate anionic $[Mn^{V}(O)(TBP_8Cz)(X)]-$ complexes ($X = F^{-}$, N_3^{-}, OCN^{-}) exhibit a ~ 5 cm^{-1} downshift of the Mn−O vibrational mode relative to the parent $Mn^{V}(O)(TBP_8Cz)$ complex as seen by resonance Raman spectroscopy. Product analysis shows that the oxidation of thioether substrates gives sulfoxide product, consistent with single OAT. A wide range of OAT reactivity is seen for the different axial ligands, with the following trend determined from a comparison of their second-order rate constants for sulfoxidation: five-coordinate ≈ thiocyanate ≈ nitrate < cyanate < azide < fluoride ≪ cyanide. This trend correlates with DFT calculations on the binding of the axial donors to the parent $Mn^{V}(O)(TBP_8Cz)$ complex.

A Hammett study was performed with p-X-$C_6H_4SCH_3$ derivatives and $Mn^V(O)(TBP_8Cz)(X)]^-$ (X = CN^- or F^-) as the oxidant, and unusual "V-shaped" Hammett plots were obtained. These results are rationalized based upon a change in mechanism that hinges on the ability of the $[Mn^V(O)(TBP_8Cz)(X)]^-$ complexes to function as either an electrophilic or weak nucleophilic oxidant depending upon the nature of the para-X substituents. For comparison, the one electron-oxidized cationic $Mn^V(O)(TBP_8Cz^{\bullet+})$ complex yielded a linear Hammett relationship for all substrates ($\rho = -1.40$), consistent with a straightforward electrophilic mechanism. This study provides new, fundamental insights regarding the influence

of axial donors on high-valent $Mn^V(O)$ porphyrinoid complexes.

A.1.3 Dramatically Accelerated Selective Oxygen-Atom Transfer by a Nonheme Iron(IV)-Oxo Complex: Tuning of the First and Second Coordination Spheres

Widger, L. R.;[†] Davies, C. G.;[‖] Yang, T.;[†] Siegler, M. A.;[†] Troeppner, O.;[§] Jameson, G. N. L.;[*,‖] Ivanović-Burmazović, I.;[§] Goldberg, D. P.[*,†]

[†]Department of Chemistry, The Johns Hopkins University, Baltimore, Maryland 21218, USA

[‖]Department of Chemistry & MacDiarmid Institute for Advanced Materials and Nanotechnology, University of Otago, P.O. Box 56, Dunedin 9054, New Zealand

[§]Department of Chemistry and Pharmacy, University of Erlangen-Nürnberg, 91058 Erlangen, Germany

Abstract: The new ligand N3PyamideSR and its Fe^{II} complex $[Fe^{II}(N_3Py^{amide}SR)](BF_4)_2$ (**1**) are described. Reaction of 1 with PhIO at −40 °C gives metastable $[Fe^{IV}(O)(N_3Py^{amide}SR)]^{2+}$ (**2**), containing a sulfide ligand and a single amide H-bond donor in proximity to the terminal oxo group. Direct evidence for H-bonding is seen in a structural analogue, $[Fe^{II}(Cl)(N_3Py^{amide}SR)](BF_4)_2$ (**3**). Complex **2** exhibits rapid O-atom transfer (OAT)

toward external sulfide substrates, but no intramolecular OAT. However, direct S-oxygenation does occur in the reaction of 1 with mCPBA, yielding sulfoxide-ligated $[Fe^{II}(N_3Py^{amide}S(O)R)](BF_4)_2$ (**4**). Catalytic OAT with **1** was also observed.

A.1.4 High-Valent Manganese−Oxo Valence Tautomers and the Influence of Lewis/Brönsted Acids on C−H Bond Cleavage

Baglia, R. A.;[†] Krest, C. M.;[‡] Yang, T.;[†,§] Leeladee, P.[†,∥] and Goldberg, D. P.[*,†]

[†]Department of Chemistry, The Johns Hopkins University, Baltimore, Maryland 21218, USA

[‡]Stanford Synchrotron Radiation Lightsource, SLAC National Accelerator Laboratory, Menlo Park, California 94025, United States

Abstract: The addition of Lewis or Brönsted acids (LA =$Zn(OTf)_2$, $B(C_6F_5)_3$, HBArF, TFA) to the high-valent manganese−oxo complex $Mn^V(O)(TBP_8Cz)$ results in the stabilization of a valence tautomer $Mn^{IV}(O\text{-}LA)(TBP_8Cz^{\bullet+})$. The Zn^{II} and $B(C_6F_5)_3$ complexes were characterized by manganese K-edge X-ray absorption spectroscopy (XAS). The position of the edge energies and the intensities of the pre-edge (1s to 3d) peaks confirm that the Mn ion is in the +4 oxidation state. Fitting of the extended X-ray absorption fine structure (EXAFS) region reveals 4 N/O ligands at $Mn-N_{ave}$ = 1.89 Å and a fifth N/O ligand at 1.61 Å, corresponding to the terminal oxo ligand. This Mn−O bond length is elongated compared to the $Mn^V(O)$ starting material (Mn−O = 1.55 Å). The reactivity of $Mn^{IV}(O\text{-}LA)(TBP_8Cz^{\bullet+})$ toward C−H substrates was examined, and it was found that H• abstraction from C−H bonds occurs in a 1:1 stoichiometry, giving a Mn^{IV} complex and the dehydrogenated organic product. The rates of C−H cleavage are accelerated for the $Mn^{IV}(O\text{-}LA)(TBP_8Cz^{\bullet+})$ valence tautomer as compared to the $Mn^V(O)$ valence tautomer when LA = Zn^{II}, $B(C_6F_5)_3$, and $HBAr^F$, whereas for LA = TFA, the C−H cleavage rate is slightly slower than when compared to $Mn^V(O)$. A large, nonclassical kinetic isotope effect of k_H/k_D = 25−27 was observed

for LA = $B(C_6F_5)_3$ and $HBAr^F$, indicating that H-atom transfer (HAT) is the rate-limiting step in the C−H cleavage reaction and implicating a potential tunneling mechanism for HAT. The reactivity of Mn^{IV}(O-LA)($TBP_8Cz^{\bullet+}$) toward C−H bonds depends on the strength of the Lewis acid. The HAT reactivity is compared with the analogous corrole complex Mn^{IV}(O−H)($tpfc^{\bullet+}$) recently reported (*J. Am. Chem. Soc.* **2015**, *137*, 14481−14487).

A.1.5 Thioether-ligated iron(II) and iron(III)-hydroperoxo/alkylperoxo complexes with an H-bond donor in the second coordination sphere†

Widger, L. R.;[a] Jiang, Y.;[a] McQuilken, A. C.;[a] Yang, T.;[a] Siegler, M. A.;[a] Matsumura, H.;[b] Moënne-Loccoz, P.;[*b] Kumar, D.;[c,d] de Visser, S. P.’[*c] Goldberg, D. P.[*a]

[a]Department of Chemistry, The Johns Hopkins University, Baltimore, Maryland 21218, USA

[b]Oregon Health & Science University, Institute of Environmental Health, Mail code: HRC3, Portland, OR 97239, USA.

[c]Manchester Institute of Biotechnology and School of Chemical Engineering and Analytical Science, The University of Manchester, Manchester, M1 7DN, UK.

[d]Department of Applied Physics, School of Physical Sciences, Babasaheb, Bhimrao Ambedkar University, Vidya Vihar, Lucknow 226-025, India.

Abstract: The non-heme iron complexes, $[Fe^{II}(N_3PySR)(CH_3CN)](BF_4)_2$ (**1**) and $[Fe^{II}(N_3Py^{amide}SR)](BF_4)_2$ (**2**), afford rare examples of metastable Fe(III)-OOH and Fe(III)-OOtBu complexes containing equatorial thioether ligands and a single H-bond donor in the second coordination sphere. These peroxo complexes were characterized by a range of spectroscopic methods and density functional theory studies. The influence of a thioether ligand and of one H-bond donor on the stability and spectroscopic properties of these complexes was investigated.

A.1.6 Dramatic Influence of an Anionic Donor on the Oxygen-Atom Transfer Reactivity of a MnV–Oxo Complex

Neu, H. M.;[a] Quesne, M. G.;[b] Yang, T.;[a] Prokop-Prigge, K. A.;[a] Lancaster, K. M.;[c] Donohoe, J.;[c] DeBeer, S.;*[c, d] de Visser, S. P.;*[b] Goldberg, D. P.*[a]

[a]H. M. Neu, T. Yang, Dr. K. A. Prokop-Prigge, Prof. D. P. Goldberg Department of Chemistry, The Johns Hopkins University Baltimore, MD (USA)

[b]Dr. M. G. Quesne, Dr. S. P. de Visser Manchester Institute of Biotechnology and School of Chemical Engineering and Analytical Science The University of Manchester, Manchester (UK)

[c]Prof. K. M. Lancaster, J. Donohoe, Prof. S. DeBeer Department of Chemistry and Chemical Biology, Cornell University Ithaca, New York (USA)

[d]Prof. S. DeBeer Max-Planck Institute for Chemical Energy Conversion, Stiftstrasse Mülheim an der Ruhr (Germany)

Abstract: Addition of an anionic donor to an $Mn^{V}(O)$ porphyrinoid complex causes a dramatic increase in 2-electron oxygen-atom-transfer (OAT) chemistry. The 6-coordinate $[Mn^{V}(O)(TBP_8Cz)(CN)]^{-}$ was generated from addition of $Bu_4N^{+}CN^{-}$ to the 5-coordinate $Mn^{V}(O)$ precursor. The cyanide-ligated complex was characterized for the first time by Mn K-edge X-ray absorption spectroscopy (XAS) and gives Mn–O=1.53 Å, Mn–CN=2.21 Å. In combination with computational studies these distances were shown to correlate with a singlet ground state. Reaction of the CN^{-} complex with thioethers results in OAT to give the corresponding sulfoxide and a $2e^{-}$-reduced $Mn^{III}(CN)^{-}$ complex. Kinetic measurements reveal a dramatic rate enhancement for OAT of approximately 24 000-fold versus the same reaction for the parent 5-coordinate complex. An Eyring analysis gives $\Delta H^{\ddagger}$=14 kcal mol^{-1}, $\Delta S^{\ddagger}$= –10 cal $mol^{-1}K^{-1}$. Computational studies fully support the structures, spin states, and relative reactivity of the 5- and 6-coordinate $Mn^{V}(O)$

complexes.

A.2 Additional work published at the University of Wisconsin—Madison

A.2.1 Inverting Steric Effects: Using "Attractive" Noncovalent Interactions To Direct Silver-Catalyzed Nitrene Transfer

Huang, M.;[†] Yang, T.;[†] Paretsky, J. D.; Berry, J. F.;[*] Schomaker, J. M.[*]

Department of Chemistry, University of Wisconsin—Madison, Madison, Wisconsin 53706, USA

[†]M.H. and T.Y. contributed equally.

Abstract: Nitrene transfer (NT) reactions represent powerful and direct methods to convert C−H bonds into amine groups that are prevalent in many commodity chemicals and pharmaceuticals. The importance of the C−N bond has stimulated the development of numerous transition-metal complexes to effect chemo-, regio-, and diastereoselective NT. An ongoing challenge is to understand how subtle interactions between catalyst and substrate influence the site-selectivity of the C−H amination event. In this work, we explore the underlying reasons why Ag(tpa)OTf (tpa = tris(pyridylmethyl)amine) prefers to activate α-conjugated C−H bonds over 3° alkyl C(sp^3)−H bonds and apply these insights to reaction optimization and catalyst design. Experimental results suggest possible roles of noncovalent interactions (NCIs) in directing the NT; computational studies support the involvement of π···π and Ag···π interactions between catalyst and substrate, primarily by lowering the energy of the directed transition state and reaction conformers. A simple Hess's law relationship can be employed to predict selectivities for new substrates containing competing NCIs. The insights presented herein are poised to inspire the design of other catalyst-controlled C−H functionalization reactions.

A.2.2 A Synthetic Oxygen Atom Transfer Photocycle from a Diruthenium Oxyanion Complex

Corcos, A. R.; Pap, J. S.;‡ Yang, T.; Berry, J. F.*

Department of Chemistry, University of Wisconsin—Madison, Madison, Wisconsin 53706, USA

Abstract: Three new diruthenium oxyanion complexes have been prepared, crystallographically characterized, and screened for their potential to photochemically unmask a reactive Ru–Ru=O intermediate. The most promising candidate, $Ru_2(chp)_4ONO_2$ (**4**, chp = 6-chloro-2-hydroxypyridinate), displays a set of signals centered around m/z = 733 amu in its MALDI-TOF mass spectrum, consistent with the formation of the $[Ru_2(chp)_4O]^+$ ($[\mathbf{6}]^+$) ion. These signals shift to 735 amu in **4***, which contains an ^{18}O-labeled nitrate. EPR spectroscopy and headspace GCMS analysis indicate that $NO_2^{\bullet}$ is released upon photolysis of **4**, also consistent with the formation of **6**. Photolysis of **4** in CH_2Cl_2 at room temperature in the presence of excess PPh_3 yields $OPPh_3$ in 173% yield; control experiments implicate **6**, $NO_2^{\bullet}$, and free NO_3^- as the active oxidants. Notably, $Ru_2(chp)_4Cl$ (**3**) is recovered after photolysis. Since **3** is the direct precursor to **4**, the results described herein constitute the first example of a synthetic cycle for oxygen atom transfer that makes use of light to generate a putative metal oxo intermediate.

Abstract: Three new diruthenium oxyanion complexes have been prepared, crystallographically characterized, and screened for their potential to photochemically unmask a reactive Ru–Ru=O intermediate. The most promising candidate, $Ru_2(chp)_4ONO_2$ (**4**, chp = 6-chloro-2-hydroxypyridinate), displays a set of signals centered around m/z = 733 amu in its MALDI-TOF mass spectrum, consistent with the formation of the $[Ru_2(chp)_4O]^+$ ($[\mathbf{6}]^+$) ion. These signals shift to 735 amu in **4***, which contains an ^{18}O-labeled nitrate. EPR spectroscopy and headspace GCMS analysis indicate that $NO_2^{\bullet}$ is released upon photolysis of **4**, also consistent with the formation of **6**. Photolysis of **4** in CH_2Cl_2 at room temperature in the presence of excess PPh_3 yields $OPPh_3$ in

173% yield; control experiments implicate **6**, $NO_2^{\bullet}$, and free NO_3^- as the active oxidants. Notably, $Ru_2(chp)_4Cl$ (**3**) is recovered after photolysis. Since **3** is the direct precursor to **4**, the results described herein constitute the first example of a synthetic cycle for oxygen atom transfer that makes use of light to generate a putative metal oxo intermediate.

Appendix B Utilizing Reaction Mechanism to Tune the Site-selectivity of Silver-Catalyzed, Intramolecular Nitrene Transfer

This appendix is under preparation:

Yang,ǂ Ryan J. Scamp,ǂ Bradley Scheffer, John F. Berry* and Jennifer M. Schomaker*

Department of Chemistry, University of Wisconsin—Madison, 1101 University Avenue, Madison, Wisconsin 53706, USA

ǂThese authors contributed equally to this manuscript.

B.1 Introduction

Strategies that enable the tunable and predictable functionalization of C–H bonds continue to be of interest for their potential to streamline the syntheses of an array of useful molecular scaffolds. In a broad sense, these transformations rely largely on either substrate- or catalyst-control (shown in Figure B. for metal-catalyzed nitrene transfer) to dictate the outcome of the reaction. In the former case, the selectively is governed mainly by the inherent electronic and/or steric features of the various C-H bonds in the organic precursor. In the latter situation, the reactivity and/or selectivity can respond to changes in the features of the catalyst. Manipulations of the metal-ligand framework can be engaged to tune the electronic properties of the metal center, thus enhancing, or even overriding, substrate control. Alternatively, alterations to the ligand can be used to impose higher steric demands on the approaching substrate; this may result in the reaction of a more accessible C-H bond over one that is inherently more activated.

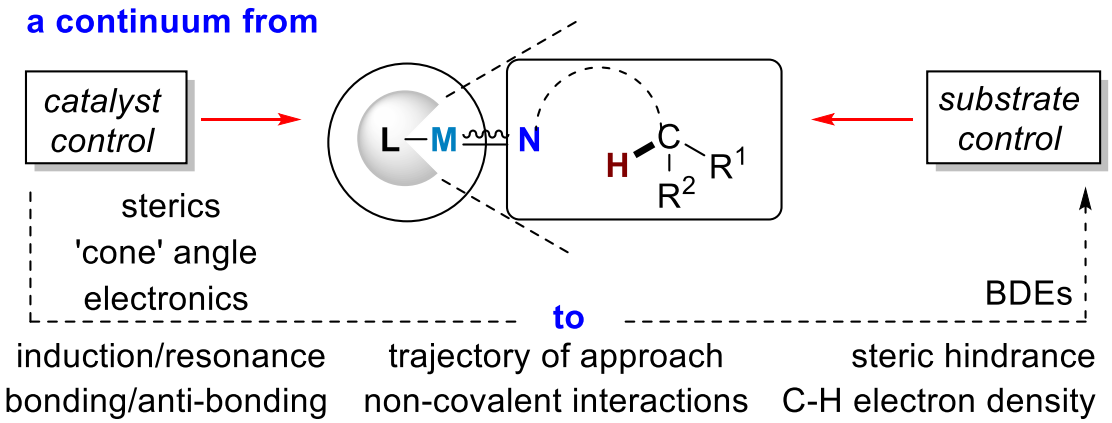

Figure B.1. Substrate vs. catalyst-controlled strategies for site-selective C-H amination via metal-catalyzed nitrene transfer.

Both substrate- and catalyst-controlled strategies have been demonstrated for a variety of C-H functionalizations, including group transfer reactions, as exemplified by transition metal-catalyzed nitrene transfers (NT). It is interesting to note that transformations involving the intermediacy of metal-oxo, metal-nitrene, and metal-carbene species have been reported that do not display selectivities expected from Hammett-type electronic tuning of the substrate. Many of these reactions also display unpredictable responses to Charton-type steric tuning of the substrate. In fact, the site-selectivities of C-H oxidation via group transfer can vary widely with changes to the catalyst, even when the identity of the transition metal is altered within the same or similar ligand framework. As just one example, intramolecular NT reactions of alkenes catalyzed by $Rh_2(esp)_2$ vs. $[Ru_2(esp)_2]^+$ yield very different results, with the former furnishing exclusive aziridination and the latter C-H bond amination to deliver the allylic amine. Parsing out the factors responsible for dictating selectivity can be challenging, but is key to expanding the array of catalysts available for diverse types of C-H functionalizations. Silver catalysts represent an excellent framework within which to study these factors, as the diversity of ligand architectures able to support NT enables steric and electronic parameters to be studied independent of the metal identity.

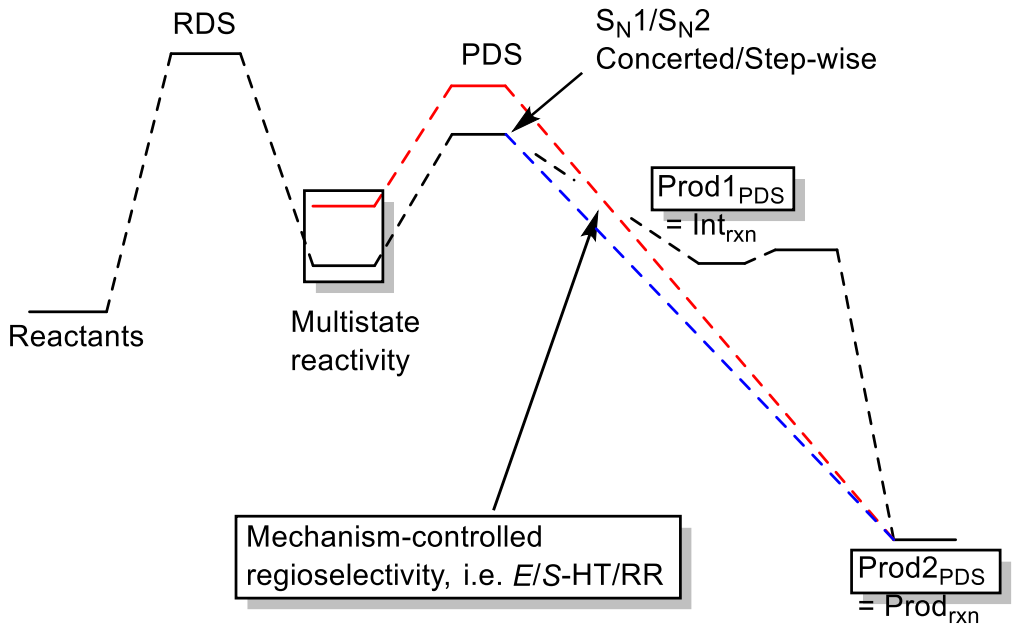

Figure B.2. Potential energy surface representation of various reaction steps in metal-catalyzed nitrene transfer. RDS = rate-determining step. PDS = product-determining step. Prod = product. Int = intermediates. Boxed items are discussed in this work.

In this work, we propose a new paradigm to control the site-selectivity of NT reactions by tuning the reaction mechanism through the ligand identity. In contrast to traditional site-selective group transfer, where activation energy is controlled by altering the energy of the reactant complex, 'mechanism-control' over site-selectivity tunes the energy of the species resulting from the product-determining step in the catalysis. This 'product' ($Prod_{PDS}$) differs from traditional products that are observed spectroscopically or isolated ($Prod_{rxn}$). The energetic relationship between the transition state (TS) and the $Prod_{PDS}$ is best described by the Bell-Evans-Polanyi (BEP) principle, which states that the more exothermic an elementary reaction step, the lower its corresponding activation energy. We hypothesized the BEP principle might be invoked to correlate the site-selectivity of transition-metal (TM) catalyzed intramolecular NT to the enthalpy of formation of the $Prod_{PDS}$ of the first elementary step in the product-determining step (PDS). Here, the $Prod_{PDS}$ are either TM-amide complexes with a tethered organic radical ($Prod1_{PDS}$ in Figure B.), or the TM catalyst and

the aminated substrate ($Prod2_{PDS}$ in Figure B.), where the two extremes are tuned by the mechanism of the PDS; solely proceeds along the dark dashed line or first along the dark dashed line then the red dashed line, respectively, in Figure B.. Using this approach, a qualitative descriptor for the reaction-mechanism controlled site-selectivity was developed to explain puzzling results in observed silver-catalyzed NT, as well as develop a predictive paradigm to tune site-selectivity. However, we also show that multiple factors influence reaction outcome; thus, caution should be used to assign the major driving force behind observed site-selectivities.

B.2 Results and Discussion

Tuning the behavior of a NT reaction, whether through substrate- or catalyst-control, directly affects the energy of the reactant complex on the potential energy surface. Substrate-controlled site-selective NT relies on the interplay of bond dissociation energy (BDE) and the accessibility of the C-H bond, features that can be manipulated by changing the electronics and sterics, respectively, of the substrate in the reactant complex. In the case of catalyst-control, pre-organization of the targeted site through the use of directing groups or attractive non-covalent interactions lowers the transition state energy by raising the energy of the reactant complex or increasing the steric accessibility of the C-H bond. Conversely, repulsive, non-covalent interactions between the catalyst and the substrate can disfavor the approach of particular C-H bonds to the putative metallonitrene, resulting in amination at a less reactive site. Enzymes are classic examples of catalysts that override substrate control to orient a specific C-H bond for reaction. For example, the chiral pocket of the protein active site in CYP411 can be modulated through mutagenesis in a manner that enables selective intramolecular NT into either the α or β C-H bond of a *o*-(*n*-propyl)benzenesulfonyl azide precursor.

Tuning the properties of reaction intermediates by altering the mechanism are known for enantioselective transformations. For example, whether a nucleophilic substitution proceeds via an S_N1 vs. an S_N2 mechanism will influence the stereochemical outcome. The same applies to enantioselective group transfer catalysis, in that concerted vs. step-wise mechanisms directly impact product stereochemistry (PDS proceeds through either the dashed dark or blue line in Figure B.). The lifetime of the reactive intermediate determines the degree of enantiocontrol; long-lived intermediates allow sufficient time for a pro-chiral or chiral site to undergo 'scrambling', while mechanisms that result in short-lived or no intermediates readily transfer chiral information from substrate to product. To some degree of approximation, the mechanism can be viewed as a connection between the stability of the reaction intermediate (or product in the absence of intermediates) and the desired enantiocontrol.

B.2.1 Investigation of regioselective, intramolecular NT using o-(n-propyl)benzenesulfonamide as the substrate.

Previous studies by Zhang and co-workers reported that reaction of the sulfonyl azide version of 1 (Table B.1, entry 1) with a Co(II)(OEP) (OEP = octaethylporphyrin) catalyst resulted in a 2.7:1 ratio of 1a:1b. The preference for benzylic C-H amination could be rationalized by a mechanism involving H-atom transfer, followed by radical rebound, which would be expected to favour reaction at the C-H bond with the lowest bond dissociation energy (BDE for α C-H in 1 ~ 85 kcal/mol; BDE for β C-H bond ~ 95 kcal/mol). The electronic configuration of d^{10} silver complexes indicates that silver metallonitrenes should also engage in step-wise NT reactions and favour reaction at the α C-H bond. However, much to our surprise, we found that dimeric silver catalysts based on tpy (terpyridine) ligands (entries 2 and 3) favored amination at the stronger

homobenzylic C-H bond to give 1b as the major product. Interestingly, while AgOTf supported by a tris(2-pyridylmethyl)amine (tpa) ligand was previously shown to promote benzylic C-H bond amination using sulfamates as the nitrogen source, reaction with 1 unexpectedly lead to amination predominantly at the homobenzylic position to yield 1b (entry 4). Overall conversion and product yields improved in the absence of light (entry 5), perhaps due to the vulnerability of catalytic intermediates to photodecomposition. A Py_5Me_2 (entry 6) ligand that furnishes a dimeric $[(Py_5Me_2Ag)_2](OTf)_2$ complex with AgOTf gave good yields of benzosultams in favour of 1b over 1a in a ratio of 4.5:1.

Table B.1. Influence of catalyst on benzylic vs. homobenzylic C-H amination.

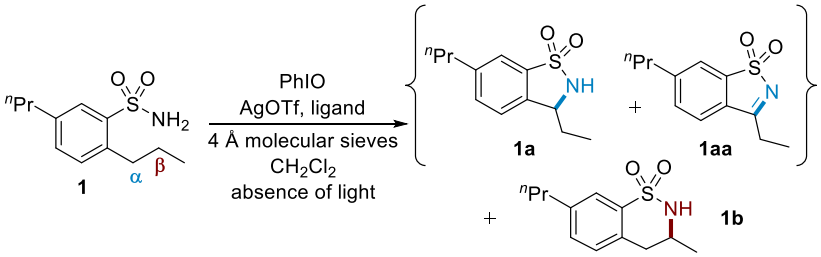

entry	ligand (equiv)	yield (%)[a]	[1a+1aa]:b	1a:1aa
1[b]	Co(OEp)	92[c]	2.7 : 1	>20 : 1
2[d]	Me_3tpy (0.12)	91	1 : 3.3	1.9 : 1
3[d]	$^tBu_3tpy$ (0.12)	85	1 : 4.0	2.0 : 1
4[e]	tpa (0.12)	50 [46]	1 : 3.6	>20 : 1
5[d]	tpa (0.12)	65	1 : 3.3	>20 : 1
6[d]	Py_5Me_2 (0.12)	86	1 : 4.5	1.6 : 1
7	[FePc]Cl /$AgSbF_6$[f]	22 [51]	3.0 : 1	>20 : 1
8	$Rh_2(esp)_2$[g]	84	1 : 1	>20 : 1
9	$Rh_2(TPA)_4$[f]	40 [45]	1 : 1.6	>20 : 1

[a] NMR yields; recovered starting material indicated in parenthesis. [b] See ref. 25, the sulfonyl azide was the substrate. [c] Isolated yield. [d] Conditions: 0.1 equiv AgOTf, *x* equiv ligand, 3.5 equiv PhIO, 4 Å MS, 0.05 M CH_2Cl_2, protected from light with Al foil. [e] 2 mol % catalyst loading. [f] 10 mol %. [g] Exposed to ambient light.

To further explore if the mechanism of the NT might play a role in determining reaction outcome, 1 was benchmarked against a [Fe(Pc)]Cl catalyst (entry 7). The reaction displayed moderate selectivity for amination at the benzylic position to furnish 1a, consistent with the presence of radical intermediates previously proposed for C–H amination.[18,41] Dinuclear Rh catalysts reported to promote concerted nitrene transfer processes behaved differently; $Rh_2(esp)_2$

(entry 8) showed no selectivity, while a modest preference for 1b was observed with $Rh_2(TPA)_4$, albeit in low conversion (entry 9). As we have previously noted several times in our studies of chemo- and site-selective aminations, the behaviour of silver seems to be distinct from other catalysts; the results in Table B.1 again underscored the unconventional behaviour of silver catalysts in NT and lead us to seek an explanation for this unexpected behaviour.

Scope of the computational study in this work. To gain a better understanding of the influence of ligand and metal on site-selective, intramolecular NT of *o*-(*n*-Pr)benzenesulfonamide 1 (Table B.1), we compared the behavior of our silver catalyst, Ag(*t*Bu$_3$tpy)OTf, to that of cobalt(II) octaethylporphyrin (Co(OEP) complex reported by Zhang to yield the opposite site-selectivity. Experimentally, Ag(*t*Bu$_3$tpy)OTf has been shown to exist as a dimer, $[Ag_2(tBu_3tpy)_2OTf]^+$, in both the solid and solution phases and can exist as two enantiomers with either clock-wise or counter-clockwise coordination of the tpy ligands (Figure B., Δ or λ conformer, respectively). This is supported by reports that $[Ag_2(tBu_3tpy)_2OTf]^+$ crystallizes in a chiral space group ($P3_1$), with only the Δ isomer in the unit cell (CSD refcode: AQAMOU), or in an achiral space group ($P2_{1/n}$), with both the Δ and λ isomer in the unit cell (CSD refcode: AQAMUA).

The Δ isomer was used to build the initial geometry of the catalyst. The *t*Bu groups on the ligand backbond of $[Ag_2(tBu_3tpy)_2OTf]^+$ are replaced by H, $[Ag_2(tpy)_2OTf]^+$ (A), to facilitate computation. Adding the sulfonyl nitrene to A to generate the initial structure of the nitrene complex A(N) produces two potential diastereomeric nitrene complexes and their corresponding TSs for each C–H bond that A(N) is capable of abstracting. One pair of these diastereomers is shown in Figure B., denoted as bz/homobz-proR/S-$[\Delta\text{-}Ag_2(tpy)_2OTf(\lambda\text{-}NSO_2Ph\text{-}o\text{-}Pr)]^+$ and bz/homobz-proR/S-$[\Delta\text{-}Ag_2(tpy)_2OTf(\Delta\text{-}NSO_2Ph\text{-}o\text{-}Pr)]^+$. It should be noted that there are 8 isomers/conformations (2 regioisomers × 2 enantiomers × 2 diastereomers) that must be

investigated for the Δ isomer of A(N) to enable the calculation of regioselectivity by statistical mechanics. In addition, two potential spin states, triplet and open shell singlet, are operative (*vida infra*), totalling 16 elementary reaction steps for each substrate that must be considered.

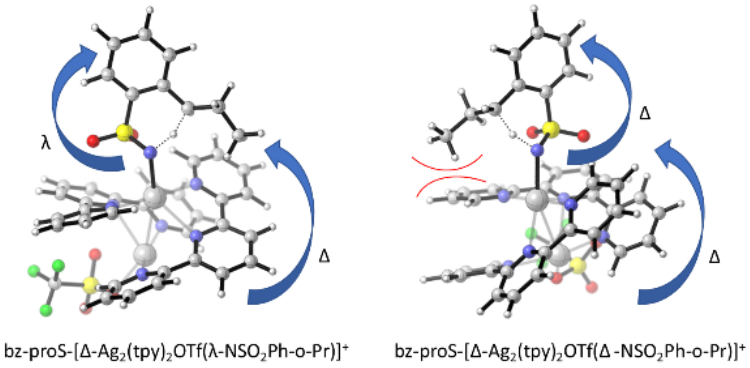

Figure B.3. Diastereomers of the Bz-*pro-S* transition states of nitrene complexes **A(N)**, Δ,λ-isomer (left) and Δ,Δ-isomer (right).

Understanding the differences in regioselective C-H amination between Co(OEP) and Ag(^{t}*Bu*$_3$*tpy)OTf.* To better understand the experimentally observed preference for amination of the homobenzylic C-H bond using silver catalysis, we performed computational studies on **A** and the truncated model of Co(OEC), Co(Por) (**B**). In previous computational work, the truncated model **A** correctly predicted the chemoselectivity of intermolecular NT into C–H bonds or C=C bonds, respectively. The calculated distances of the first coordination sphere and electronic structures of **A(N)** and **B(N)** are in line with previous calculations. In particular, both **A(N)** and **B(N)** exist in charge-transferred electronic configurations—Ag(II)- and Co(III)-nitrene radical anion structures, respectively, as evidenced by their respective mulliken spin populations (Table B.2) and singly occupied unrestricted natural (UNO) orbitals (Figure B.). The ground spin state of **A(N)** is triplet state with one unpaired electron on Ag(II) ferromagnetically coupled to the other unpaired electron on the nitrene anion radical. The ground spin state of **B(N)** is a double state with the unpaired electron localized on the nitrene anion radical and a diamagnetic t_{2g}^6 Co(III) center. Departing from the first coordination sphere the ligand backbones of the nitrene complexes constitute the

major driving force behind the steric-controlled selectivity of these complexes; both **A(N)** and **B(N)** share similar ligand-substrate interactions where the relatively flat surface formed by the ligands allows a majorly electronic-controlled selectivity

Table B.2. Selected Mulliken spin populations for **A(N)**.

Complex	**ρ(M)**	**ρ(N)**
A(N)	triplet	
	0.29 (M = Ag)	1.38
	BS(1,1)	
	0.40 (M = Ag)	-0.59
B(N)	doublet	
	-0.06 (M = Co)	0.94

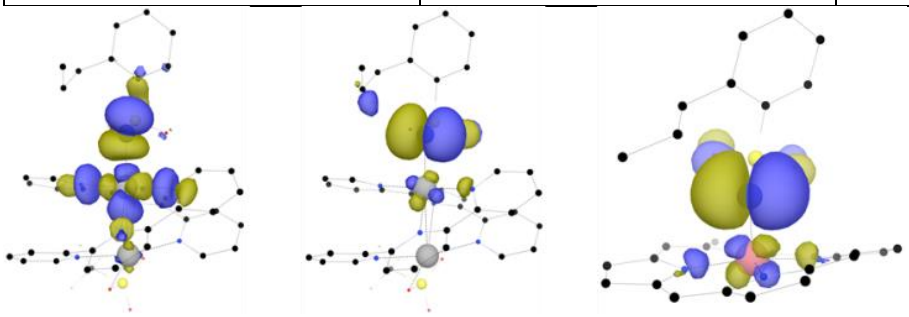

Figure B.4. Singly occupied unrestricted natural spin orbitals of **A(N)** (left and middle) and **B(N)** (right).

The potential energy surface for the NT of a truncated model of **1** (the propyl group *meta* to the sulfonamide in **1** is replaced with a H) catalyzed by **A(N)** is shown in Figure B.. The NT proceeds through an initial hydrogen atom transfer (HAT) TS for both the benzylic (α) and homobenzylic (β) C–H bonds. This step is formally a coupled one-electron/one-proton transfer into the empty β orbital of the nitrene anion radical on the triplet surface. The outcomes of the initial TS are the corresponding silver(II)-amido complexes (Ag(II)-NHR) and a tethered organic radical. Based on the calculated HAT TSs, the regioselectivity is found to be 1:7.8 α:β (1:4.9 when only the lowest energy TS for each site is considered), which is in good agreement with the

experimental value of α:β 1:4.0. After the TSs of the two HAT processes at the α and β C-H bonds, the chemical event diverges, depending on which hydrogen atom is abstracted. In the case of the β hydrogen, the diradical intermediate formed after HAT proceeds through a barrierless radical recombination on the open-shell singlet surface, rendering the complete NT an elementary step (*E*-HT/RR; left in Figure B.). In contrast, a diradical intermediate is found for α insertion on both the triplet and open-shell singlet surface; radical recombination on the open-shell singlet surface furnishes the 5-membered sultam, amounting to a stepwise radical recombination mechanism (*S*-HT/RR; right in Figure B.). As the $Prod_{PDS}$ after the initial HT step are different for these two sites, the corresponding reaction enthalpies are divergent; -76.5 and -7.27 kcal·mol^{-1} for the homobenzylic and benzylic C–H bonds, respectively. This highly exothermic elementary step lowers the activation energy at the ß position according to the BEP principle, rendering the homobenzylic insertion the major $Prod_{rxn}$.

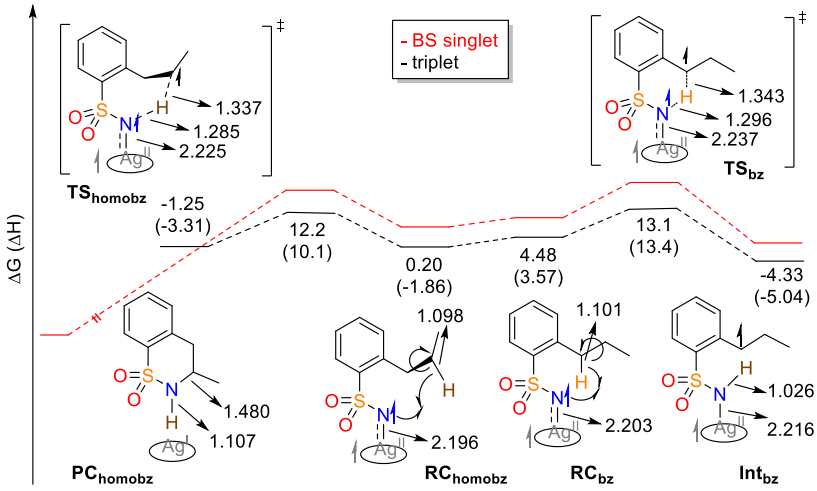

Figure B.5. TSR for NT into the proR-α (left) or proS-β (right) C–H bonds mediated by **A(N)**.

For comparison, we calculated the potential energy surfaces (PESs) for NT reactions of **B(N)** to the α or β C–H bonds (for both proR and proS) on the doublet PES (Figure B.). In contrast to our findings for **A(N)**, only the S-HT/RR mechanism was found for **B(N)**, regardless of whether HT occurs at the α or β position, consistent with the previous experimental observation that

intramolecular NT catalyzed by a Co(Por) complex is controlled by the relative BDE of the C–H bonds, exhibits a high H/D kinetic isotope effect (6.6), and is inhibited by TEMPO.[1] Thus, the different site-selectivity of **A(N)** and **B(N)** for the α and β sites of 1 can be rationalized by their differing mechanisms (vida infra).

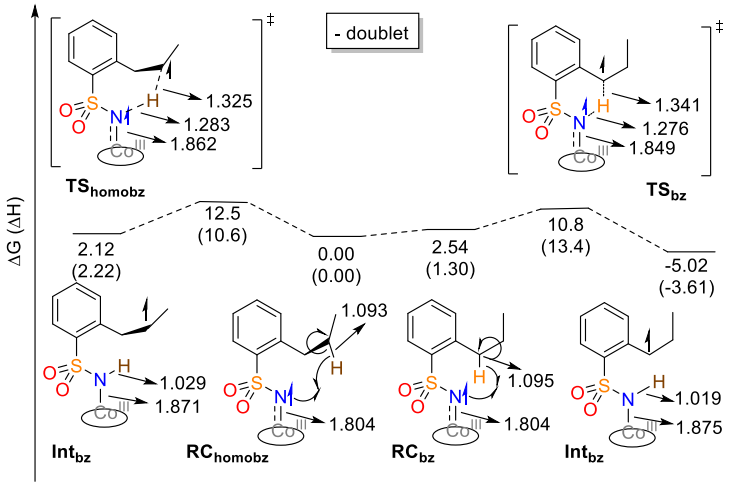

Figure B.6. TSR for NT into the proR-α (left) or proS-β (right) C–H bonds mediated by **B(N)**.

B.2.2 Tunability of reaction-mechanism controlled regioselective intramolecular NT.

Our computational studies on the NT mechanisms and the regioselectivities of **A(N)** and **B(N)** provide an opportunity to understand the differential site-selectivity displayed by these two catalysts. **A(N)** and **B(N)** both initiate NT by an HT TS, which is expected to result in a metal-amido complex with a tethered organic radical. Due to the nature of HT, the site-selectivity is expected to be dominated by the BDE of the abstracted C–H bond. Therefore, it might be expected that substitution of the γ-CH_3 group of **1** with a CO_2Et group in **3** (Scheme B.) would promote higher β selectivity with **A(N)**, as the BDE of the ß C–H bonds in **1** is 98 kcal·mol^{-1} while that in **3** is 92 kcal·mol^{-1}. However, the β selectivity was attenuated, a counterintuitive result based on BDE arguments. In contrast, the BDE argument is supported in studies of catalysts based on **B(N)**, where an intramolecular competition experiment shows that a C-H bond located α to an ester can be favored.

Scheme B.1. Correlation between regioselectivity and reaction mechanism

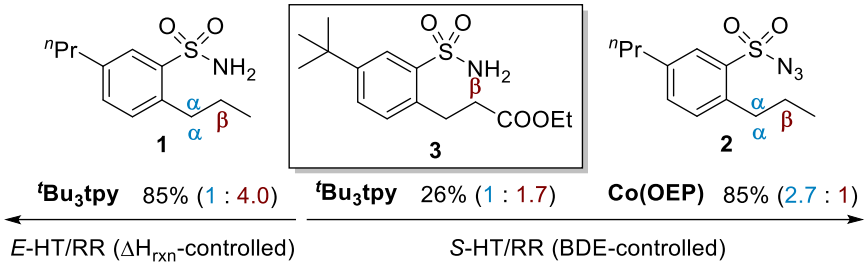

To understand this discrepancy, we performed DFT calculations on **A(N)** using **3**, designated as **A'(N)** (Figure B.). The calculated regioselectivity is 1.7:1 α:β, compared to the experimental selectivity of 1:1.7 α:β, slightly underestimating the preference for the β C–H bonds. The increased TS energy of the β C–H bonds, as compared to α C-H bonds, is accompanied by a change in mechanism from *E*-HT/RR to *S*-HT/RR; Ag(II)-amide with a tether organic radical is observed on both the triplet and open-shell singlet surface. This converging mechanism of NT with **A'(N)** renders the regioselectivity substrate-controlled; the BDE of the 2° benzylic C–H bonds (~85 kcal·mol^{-1}) is lower than that of the 2° C–H bonds with a terminal carboxyl group (~92 kcal·mol^{-1}).

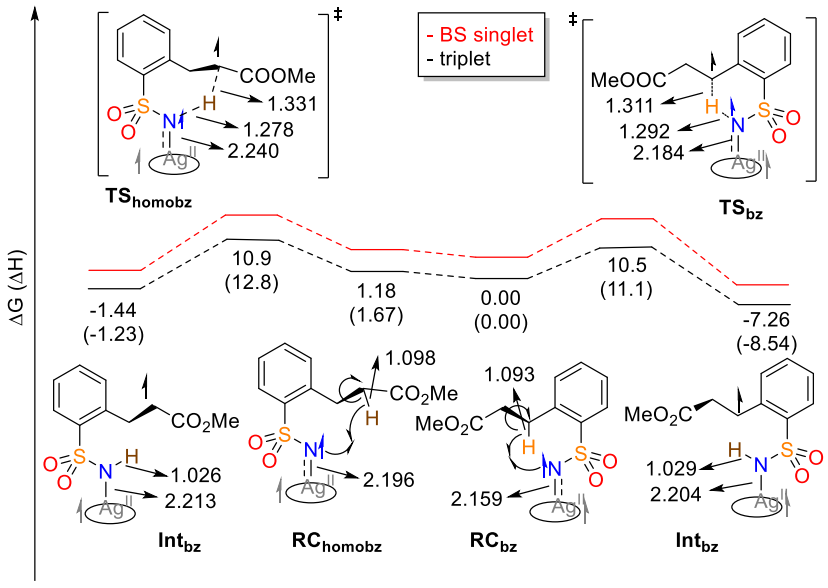

Figure B.7. TSR for NT into the proR-α (left) or proS-β (right) C–H bonds mediated by **A'(N)**.

B.2.3 The origin of reaction-mechanism controlled site-selective intramolecular NT and guide to future developments.

We established using **A(N)**, **A'(N)**, and **B(N)** that reaction mechanism after the PDS is the driving force behind the differential regioselectivity—whether the NT proceeds through an *E*-HT/RR or an *S*-HT/RR mechanism. For HT from a α C–H bond to the metal-nitrene group, the resulting benzylic radical is resonance-stabilized (less than one electron on ρ(C) in Table B.3). This resonance renders the diradical intermediate species thermodynamically accessible (the reaction path on the right in Figure B.-5.11). On the other hand, HT from the β C–H bond to the metal nitrene complexes generates an unstable diradical intermediate species due to the presence of a localized aliphatic radical for **A(N)** and **B(N)** (Table B.3). Hence, β activation is unfavorable both kinetically and thermodynamically when only the *S*-HT/RR mechanism is operative *(*middle in Scheme B.); **B(N)** prefers to insert into the benzylic C–H bonds.

Table B.3. Selected Mulliken spin populations for Int-**A(N)**, Int-**B(N)**, and Int-**A'(N)**.

Complex		**Int-A(N)**	**Int-B(N)**	**Int-A'(N)**
β	**ρ(M)**	-0.37[a,b]	-0.01	-0.38
	ρ(N)	-0.33[a,b]	0.03	-0.33
	ρ(C)	0.99[a]	1.01	0.86
α	**ρ(M)**	-0.30[b]	0.04	-0.36
	ρ(N)	-0.43[b]	-0.02	-0.35
	ρ(C)	0.70[c]	0.76[c]	0.76

[a] Spin population was calculated based on the optimized structure of ^{3}TS(proR-β). [b] The remainder of the β spin is delocalized between the tpy ligands. [c] The remainder of the α spin is delocalized in the aromatic ring.

The analysis is expanded when the radical nature of the intermediate metal-amido complex is taken into consideration. For **B(N)**, the resulting (Por)Co(III)-amido complex contains a relatively stable diamagnetic Co(III) center with a t_2g^6-derived configuration and an innocent

amide ligand. This observation is supported by the calculated spin population (Table B.2), the reported isolation of (Por)Co(III) complexes with various axial ligands,[2-14] and the stability of (Por)Co(III)(X) as evidenced by the reversible CoII/CoIII redox couple and the presence of multiple higher anodic waves.[15-17] This differs from **A(N)**, where the Ag(II)-amido complex resulting from HT is not expected to be stable, since it has considerable Ag(I)-aminyl radical character, as evidenced by the non-integer spin values for Ag and N (Table B.3). Furthermore, crystal structures of Ag(II) complexes supported by polypyridyl ligands are rare (mostly isolated by electrocrystallization of the corresponding Ag(I) complexes),[18-21] while the instability of Ag(II)-polypyridyl complexes is evidenced by the irreversible nature of the $Ag^{+/2+}$ redox couples. We have previously demonstrated that the non-innocence of the bound nitrogen-based axial ligand associates with the redox potential of the metal center.[22] This nitrogen radical can undergo a barrierless RR with the tethered organic radical when: a) the organic radical is unstable and the spin is localized, i.e. aliphatic vs. benzylic radical, b) the metal-centered unpaired electron is easily delocalized to the N atom, and c) steric repulsion between the amidyl group and the organic radical does not hinder the RR. All these criteria allow *E*-HT/RR to become operative for activation of the β C-H bond of **1** by **A(N)**, resulting in a highly exothermic $Prod_{PDS}$ after the initial HT (right side in Scheme B.). The activation energy of the *E*-HT/RR is lowered, compared to that if the reaction proceeded through *S*-HT/RR, by the BEP principle. The reason why **A'(N)** proceeds thrugh *S*-HT/RR in spite of an unstable Ag(II)-amide generated from the HT step is that the generated organic radical at the ß position is resonance stabilized by the germinal carboxyl group (middle in Scheme B.2), rendering the selectivity substrate-controlled.

Scheme B.2. Association between valence tautomers of Ag-amido complex and the stability of the tethered organic radical generated after the HT process and the reaction mechanism

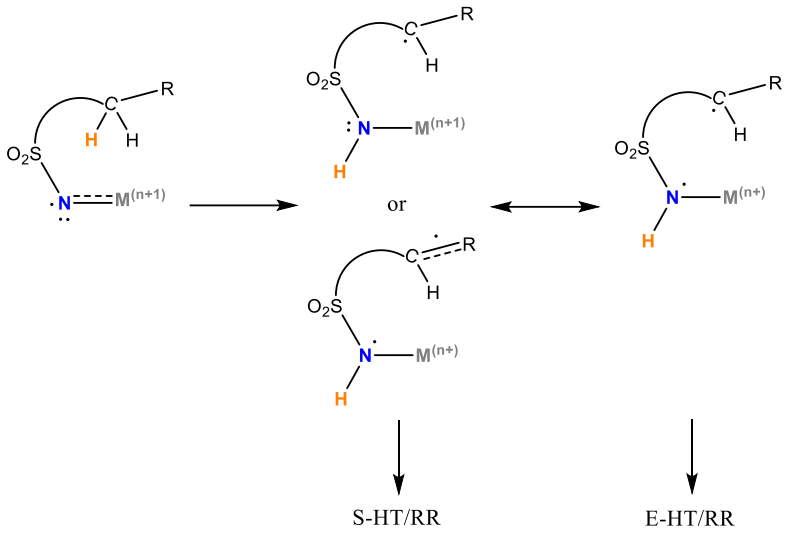

One caveat is to be noted: the multistate reactivity (a singlet Ag(I) catalyst proceeds to form a triplet Ag(II)-nitrene anion radical, which then finishes with the singlet Ag(I) catalyst) of the silver-nitrene is crucial to the mechanism-controlled regioselectivity. The reason for this is that if the whole catalytic cycle occurs on the same spin surface, i.e. $Rh_2(esp)_2$ catalyzed nitrene transfer, the *E*-HT/RR mechanism will collapse into the concerted mechanism (instead of proceeding through the dashed dark line first, the PDS will proceed through the dashed red line in Figure B.). In this case, the step-wise and concerted mechanisms are two distinct families of reactions that cannot be categorized by the BEP principle.

B.2.4 Multiple factors can compete to drive regioselectivity.

In the preceding section, we propose and explain a new paradigm using reaction mechanism to control the site-selectivity. We established using **A'(N)**, **A(N)** with a γ COOEt group, that changes in the electronic induction can attenuate, if not override, the reaction-mechanism-controlled site-selectivity. However, an attractive feature of Ag-catalyzed NT is that we can readily engage other driving forces to alter reaction-mechanism-controlled site-selectivity. For example, steric effects are commonly utilized to tune the selectivity of C-H functionalization. For example, mutations of the artificial cytochrome P450 enzyme CYP 411 can modulate the α:ß

ratio using the azide version of **1**, even though the electronic properties of the reactive Fe(Por)-nitrene intermediates and the mechanism are not affected.

To show how the nature of the ligand on Ag alters the competition between steric- and reaction-mechanism-controlled site-selectivity, we subjected both **A** and the bulky $[Ag_2(Py_2Me_2)_2]^{2+}$ (**C**) to substrates with varying degrees of steric demand. Table B.4 shows that catalyst **A** and **C** behave similarly in terms of regioselectivity for less sterically demanding substrates **1**, **3**, and **4** and presumably operate via the same reaction mechanism. However, with sterically demanding substrates **5-7**, A shows little sensitivity to steric pressure and selectivity is driven by reaction mechanism. In contrast, **C** increasingly prefers amination of the benzylic α C–H bond as the steric bulk at the γ position increases; thus, the selectivity is steric-controlled.

Table B.4. Reaction-mechanism vs. steric-controlled in site-selective C-H amination.

Reaction-mechanism control > Steric control

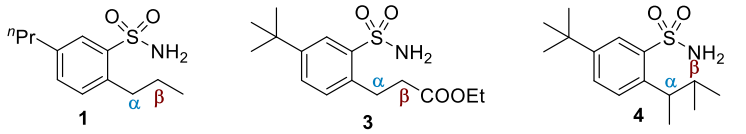

1	3	4
Py_5Me_2[a] 86% (1 : 4.5)	**Py_5Me_2** 40% (1 : 1.0)	**Py_5Me_2** >99% (1.1 : 1)
$^tBu_3tpy$[a] 85% (1 : 4.0)	**$^tBu_3tpy$** 26% (1 : 1.7)	**$^tBu_3tpy$** 75% (1.6 : 1)

Steric control > Reaction-mechanism control

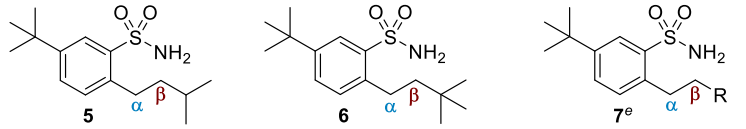

5	6	7[e]
Py_5Me_2 79% (1.6 : 1)	**Py_5Me_2** 89% (6.3 : 1)[b,c]	**Py_5Me_2** 56% (4.6 : 1)[b,d]
$^tBu_3tpy$ 76% (1 : 5.9)	**$^tBu_3tpy$** 85% (1 : 3.8)	**$^tBu_3tpy$** 85% (1 : 5.9)

[a] **Conditions:** 0.1 equiv AgOTf, 0.12 equiv ligand, 3.5 equiv PhIO, 4 Å MS, 0.05 M CH_2Cl_2, protected from light with aluminum foil. [b] NMR yield. [c] 2.4:1 amine/imine at the α position. [c] 6.0:1 amine/imine at the α position. [e] R = adamantyl.

Electronic effects are frequently employed to affect site-selectivity. To highlight the interplay between reaction-mechanism and electronic control of the reaction, NT using catalyst C was carried out on **1**, **8**, and **9**, as it was shown in Table B.4 to behave similarly to catalyst **A** for the less bulky **1**, **3**, and **4**. The substrates in Table B.5 were designed to display an increase in the

Hammett σ_p values (-0.60 for 8, -0.41 for 1, and 0.15 for 9). With the increase in the σ_p values, the preference for amination of the α C-H bond should decrease, as has been seen in intramolecular NT at benzylic positions. Interestingly, both **8** and **9** show preference for reaction at the β C–H bonds, a result that appears counterintuitive using an argument that relies mainly on the substrate electronic effect.

When the electronic effect on the metal-ligand motif is considered through an σ_m effect, **8** and **9** have ~0.3-0.4 σ_m values and give similar preference for amination at the β C-H; in contrast, the selectivity is lower for **1**, which has a negative σ_m value. This suggests that nitrene intermediate **C(N)** is electrophilic, as the literature reports that Ag-catalyzed NT reactions show negative responses to σ_p. However, an electron-deficient **C(N)** would not be expected to favor more electron-deficient homobenzylic C–H bonds, as has been noted for NT reactions that operate through the same mechanism for both C–H positions, such as Rh_2 catalysts that proceed through a concerted mechanism or [Mn(^{t}BuPc)]Cl, Ag(tpa)OTf and Ag(bpy)$_2$OTf that proceed through stepwise mechanism. This discrepancy can be explained by invoking cooperation between the reaction-mechanism and the electronic effects. As we have suggested previously, the *E*-HT/RR mechanism results from an unstable Ag(II)-amide complex, which tautomerizes to an Ag(I)-amidyl-radical to proceeds through a barrierless radicl recombination. The less electron-donating the amide generated from the HT step, the less stable is the Ag(II)-amide complex that is generated. The electron-donating strength of the metal nitrene, and hence the amide, is correlated with the σm values: varying the meta substituent from a *m*-^{n}Pr to a *m*-(N-oxazolidinone) to a *m*-bromo diverts the reaction mechanism towards the extreme of *E*-HT/RR at the β site, hence increasing the regioselectivity for the β site.

Table B.5. Electronic effect on site-selective C-H amination

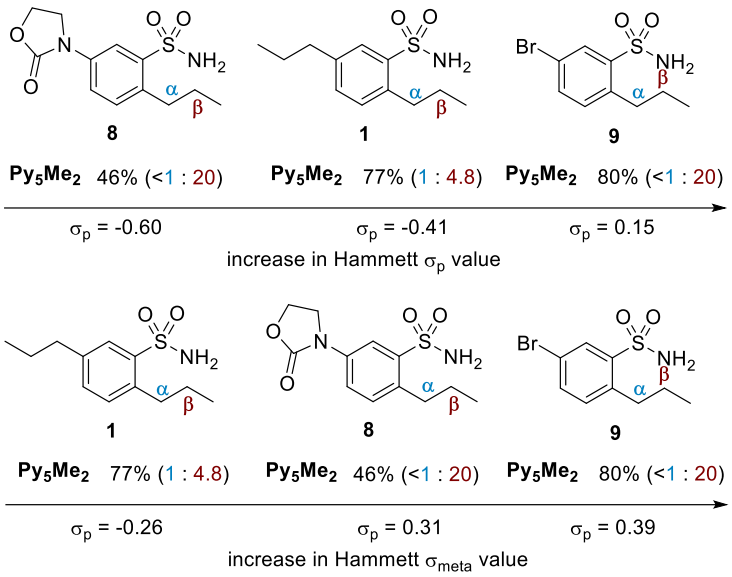

B.3 Conclusion

To our knowledge, the computational studies reported herein demonstrate the first examples of combined experimental and computational evidence for the possibility of two operative NT mechanisms, *E*-HT/RR and *S*-HT/RR, *occurring on the same substrate*, with the only difference being the loci of the activated C–H bonds. The divergent mechanisms result from a) the stability of the organic radicals generated by the initial HT process and b) the electronic structures of the resulting metal-amido complexes. These divergent mechanisms, leading to different reaction outcomes immediately after the initial HT process, are the origin of the differential regioselectivity of catalysts **A** and **B** as a result of the Bell-Evans-Polanyi principle. These conclusions have the potential to be extrapolated to other group transfer reactions to provide a different perspective on the design of catalysts for tunable, site-selective C-H functionalization.

Silver(I) continues to exhibit unusual behaviour among transition metals competent in NT. They display a superior ability to consistently enable amination of homobenzylic methylene C-H bonds with higher yields relative to their typically more active benzylic methylene neighbours.

Explorations of substituent effects revealed that outcomes can depend on either steric or electronic factors, depending on the nature of the ligand and the reaction mechanism. Thus, Ag(I) displays unusual versatility; it is not constrained to steric control, as are dinuclear rhodium complexes, nor is it heavily biased toward sites with low BDE, as noted with cobalt. The adaptable nature of silver described in this manuscript bears exceptional potential for further work in tunable, catalyst control of group transfer reactions, and continues to be the subject of forthcoming studies from our groups.

B.4 Acknowledgments

This work was funded through an NSF-CAREER Award 1254397 and the Wisconsin Alumni Research Foundation to J.M.S. The NMR facilities at UW-Madison are funded by the NSF (CHE-9208463, CHE-9629688) and NIH (RR08389-01). The National Magnetic Resonance Facility at Madison is supported by the NIH (P41GM103399, S10RR08438, S10RR029220) and the NSF (BIR-0214394). Mass spectrometry was acquired on a Q Exactive Plus Orbi Mass Spectrometer funded by the NIH (1S10OD020022-1). J.F.B. thanks the Center for Selective C−H Functionalization supported by the National Science Foundation (CHE01205646). The computational facility at Madison is supported in part by National Science Foundation Grant CHE-0840494 and at the UW-Madison Center For High Throughput Computing (CHTC) in the Department of Computer Sciences. The CHTC is supported by UW-Madison, the Advanced Computing Initiative, the Wisconsin Alumni Research Foundation, the Wisconsin Institutes for Discovery, and the National Science Foundation, and is an active member of the Open Science Grid, which is supported by the National Science Foundation and the U.S. Department of Energy's Office of Science. U.S. Chimera is developed by the Resource for

Biocomputing, Visualization, and Informatics at the University of California, San Francisco (supported by NIGMS P41-GM103311).

B.5 References

1. Lu, H.; Hu, Y.; Jiang, H.; Wojtas, L.; Zhang, X. P., Stereoselective Radical Amination of Electron-Deficient C(sp3)–H Bonds by Co(II)-Based Metalloradical Catalysis: Direct Synthesis of α-Amino Acid Derivatives via α-C–H Amination. *Org. Lett.* **2012,** *14* (19), 5158-5161.
2. Summers, J. S.; Petersen, J. L.; Stolzenberg, A. M., Comparison of the Structures of the 5-Coordinate Cobalt (II) Pyridine, 5-Coordinate Cobalt (III) Methyl, and 6-Coordinate Cobalt (III) Methyl Pyridine Complexes of Octaethylporphyrin. *J. Am. Chem. Soc.* **1994,** *116* (16), 7189-7195.
3. Sakurai, T.; Yamamoto, K.; Naito, H.; Nakamoto, N., The Crystal and Molecular Structure of Chloro-α,β,γ,δ-tetraphenylporphinatocobalt(III). *Bull. Chem. Soc. Jpn.* **1976,** *49* (11), 3042-3046.
4. Penoni, A.; Wanke, R.; Tollari, S.; Gallo, E.; Musella, D.; Ragaini, F.; Demartin, F.; Cenini, S., Cyclopropanation of Olefins with Diazoalkanes, Catalyzed by CoII (porphyrin) Complexes− A Synthetic and Mechanistic Investigation and the Molecular Structure of CoIII (TPP)(CH2CO2Et)(TPP= Dianion of meso-Tetraphenylporphyrin). *Eur. J. Inorg. Chem.* **2003,** *2003* (7), 1452-1460.
5. Masuda, H.; Taga, T.; Sugimoto, H.; Mori, M., Crystal and molecular structure of formylmethyl(tetraphenylporphinato)cobalt(III). *J. Organomet. Chem.* **1984,** *273* (3), 385-392.
6. Liu, C. R.; Qian, Y. Y.; Chan, K. S., Base-promoted aryl-bromine bond cleavage with cobalt(ii) porphyrins via a halogen atom transfer mechanism. *Dalton Trans.* **2014,** *43* (21), 7771-7779.
7. Lin, Z.; Zhang, Z.-M.; Chen, Y.-S.; Lin, W., Highly Efficient Cooperative Catalysis by CoIII(Porphyrin) Pairs in Interpenetrating Metal–Organic Frameworks. *Angew. Chem.* **2016,** *128* (44), 13943-13947.
8. Lee, S. Y.; Fung, H. S.; Feng, S.; Chan, K. S., Visible Light Photocatalysis of Carbon–Carbon σ-Bond Anaerobic Oxidation of Ketones with Water by Cobalt(II) Porphyrins. *Organometallics* **2016,** *35* (15), 2480-2487.
9. Kastner, M. E.; Scheidt, W. R., Stereochemistry of low-spin cobalt porphyrins. 9. preparation and characterization of five-coordinate organocobalt(III) derivatives. *J. Organomet. Chem.* **1978,** *157* (1), 109-123.
10. Fritsch, J. M.; McNeill, K., Aqueous reductive dechlorination of chlorinated ethylenes with tetrakis (4-carboxyphenyl) porphyrin cobalt. *Inorg. Chem.* **2005,** *44* (13), 4852-4861.
11. Cheng, R.-J.; Chen, Y.-H.; Chen, C.-C.; Lee, G.-H.; Peng, S.-M.; Chen, P. P.-Y., Dual-Channel-Mediated Spin Coupling for One-Electron-Oxidized Cobalt (II)-Saddled Porphyrin. *Inorg. Chem.* **2014,** *53* (17), 8848-8850.
12. Cao, Y.; Petersen, J. L.; Stolzenberg, A. M., Metalloradical Chemistry of Cobalt(II) Porphyrins. The Syntheses, Structure, and Reactivity of Triphenyltin(II)- and Trihalomethylcobalt(III) Octaethylporphyrin. *Inorg. Chem.* **1998,** *37* (20), 5173-5179.
13. Cao, Y.; Petersen, J. L.; Stolzenberg, A. M., Do organocobalt porphyrins have agostic alkyl groups? An investigation of the structure of ethyl cobalt (III) octaethylporphyrin and the nuclear

magnetic resonance spectra of 13 C-labeled alkyl cobalt (III) porphyrin complexes. *Inorg. Chim. Acta* **1997,** *263* (1), 139-148.
14. Angurell, I.; Martínez-Ruiz, I.; Rossell, O.; Seco, M.; Gómez-Sal, P.; Martín, A.; Font-Bardia, M.; Solans, X., About the different reactivity of dinuclear palladium and platinum compounds with trispyrrolylphosphine: Synthesis and X-ray crystallographic results of new palladium complexes containing P–pyrrolyl bonds. *J. Organomet. Chem.* **2007,** *692* (18), 3882-3891.
15. Chang, C. J.; Deng, Y.; Shi, C.; Chang, C. K.; Anson, F. C.; Nocera, D. G., Electrocatalytic four-electron reduction of oxygen to water by a highly flexible cofacial cobalt bisporphyrin. *Chem. Commun.* **2000,** (15), 1355-1356.
16. Walker, F. A.; Beroiz, D.; Kadish, K. M., Electronic effects in transition metal porphyrins. 2. The sensitivity of redox and ligand addition reactions in para-substituted tetraphenylporphyrin complexes of cobalt(II). *J. Am. Chem. Soc.* **1976,** *98* (12), 3484-3489.
17. Setsune, J.-i.; Takeda, H.; Ito, S.; Saito, Y.; Ishimaru, Y.; Fukuhara, K.; Saito, Y.; Kitao, T.; Adachi, T., Synthesis of Vinylene-Co,N-Linked Multi(porphyrin)s by the Addition of Free-Base Porphyrins to a C2H2 Complex of Cobalt(III) Porphyrin and Their Oxidative Rearrangement to Vinylene-N,N‘-Linked Multi(porphyrin)s. *Inorg. Chem.* **1998,** *37* (9), 2235-2246.
18. Kandaiah, S.; Peters, E. M.; Jansen, M., Electrocrystallization of Tetra-and Hexa-coordinated Silver (II) Compounds Based on 4, 4′-Dimethyl-2, 2′-Bipyridine Ligand–Single Crystal Structures and Magnetic Studies. *Z. Anorg. Allg. Chem.* **2008,** *634* (14), 2483-2486.
19. Kandaiah, S.; Huebner, R.; Jansen, M., Electrocrystallisation and single crystal structure determination of Bis (2, 2′-bipyridyl) silver (II) perchlorate [Ag (bipy) 2](ClO 4) 2. *Polyhedron* **2012,** *48* (1), 68-71.
20. Bastida, R.; Fenton, D. E.; López-Deber, M.; Macías, A.; Valencia, L.; Vicente, M., Synthesis of perchlorate metal complexes with a new tetrapyridyl pendant armed macrocyclic ligand. *Inorg. Chim. Acta* **2003,** *355*, 292-301.
21. Atwood, J. L. S., M. L.; Zatko, D. A., *Cryst. Struct. Commun.* **1973,** *2*, 279.
22. Varela-Alvarez, A.; Yang, T. H.; Jennings, H.; Kornecki, K. P.; Macmillan, S. N.; Lancaster, K. M.; Mack, J. B. C.; Du Bois, J.; Berry, J. F.; Musaev, D. G., Rh_2(II,III) Catalysts with Chelating Carboxylate and Carboxamidate Supports: Electronic Structure and Nitrene Transfer Reactivity. *J. Am. Chem. Soc.* **2016,** *138*, 2327-2341.